Cover design by Hylmar Lindeboom.

The work described in this thesis was carried out in the Photonics & Semiconductor Nanophysics (PSN) group, Faculty of Applied Physics, at Eindhoven University of Technology, in a close collaboration with the Photonics for Energy group at the Dutch Institute for Fundamental Energy Research (DIFFER, from July 2015), which was until June 2015 named Surface Photonics and part of FOM-institute AMOLF, and which was located at Philips Research Laboratories. The work was funded by STW (Dutch Technology Foundation).

A catalogue record is available from the Eindhoven University of Technology Library
ISBN: 978-90-386-4116-4

NANOWIRE PHOTONICS FOR PHOTOVOLTAICS

PROEFSCHRIFT

ter verkrijging van de graad van doctor aan de Technische Universiteit Eindhoven, op gezag van de rector magnificus prof.dr.ir. F.P.T. Baaijens, voor een commissie aangewezen door het College voor Promoties, in het openbaar te verdedigen op maandag 17 oktober 2016 om 16:00 uur

door

Arie Dirk van Dam

geboren te Zederik

Dit proefschrift is goedgekeurd door de promotoren en de samenstelling van de promotiecommissie is als volgt:

Voorzitter:	Prof.dr. H.J.H. Clercx
Promotoren:	Prof.dr. J. Gómez Rivas
	Prof.dr. E.P.A.M. Bakkers
Copromotor:	Dr. J.E.M. Haverkort
Leden:	Dr. J.A. Sánchez-Gil (Instituto de Estructura de la Materia – CSIC)
	Prof.dr. A. Polman (Universiteit van Amsterdam)
	Prof.dr. H.J.M Swagten
	Prof.dr. R.E.I. Schropp

Het onderzoek dat in dit proefschrift wordt beschreven is uitgevoerd in overeenstemming met de TU/e Gedragscode Wetenschapsbeoefening.

CONTENTS

1 INTRODUCTION 1
- 1.1 Sustainable energy 1
- 1.2 Photovoltaics 3
  - 1.2.1 Working principle of single junction solar cell 5
  - 1.2.2 Solar spectrum 5
  - 1.2.3 Materials 6
  - 1.2.4 Absorption and emission 6
- 1.3 Semiconductor nanowires 8
  - 1.3.1 Fabrication methods 9
  - 1.3.2 Optoelectronic applications 11
- 1.4 Nanowire solar cells 12
  - 1.4.1 Nanowire photonics 14
  - 1.4.2 Absorption of light in nanowires 14
  - 1.4.3 Emission from nanowires 15
- 1.5 Advantages of nanowires for solar cells 16
- 1.6 Outline of the thesis 17

2 THEORETICAL BACKGROUND 19
- 2.1 Solar cell physics 19
  - 2.1.1 Detailed balance of photons/electrons 19
  - 2.1.2 Losses in photovoltaic energy conversion 21
  - 2.1.3 External luminescence efficiency 23
  - 2.1.4 Photon reabsorption 25
- 2.2 Single nanowire photonics 27
  - 2.2.1 Mie theory 27
  - 2.2.2 Calculation of waveguide mode dispersion 27
  - 2.2.3 1D current emission model based on waveguide modes 31

3 EXPERIMENTAL METHODS 35
- 3.1 Fourier microscopy 35
  - 3.1.1 Polarization analysis 36
- 3.2 Time-reversed Fourier microscopy 37
- 3.3 Calibrated photoluminescence intensity measurements 38
  - 3.3.1 Collection efficiency of photoluminescence 40
  - 3.3.2 Power-dependent photoluminescence measurements 40

4 ENHANCED VOLTAGE IN NANOWIRE SOLAR CELLS 43

4.1 Introduction 43
4.2 Direct material comparison 45
4.3 Voltage measurements 46
4.4 Effects on V_{OC} through nanostucturing 47
4.4.1 Material volume reduction 47
4.4.2 Enhanced emission outcoupling 47
4.4.3 Other effects 50
4.5 Solar cell devices 50
4.6 Conclusion 54
5 ENHANCED AND OMNIDIRECTIONAL ABSORPTION IN NANOWIRE SOLAR CELLS USING MIE SCATTERING ITO NANOPARTICLES 55
5.1 Introduction 55
5.2 Time-reversed Fourier Microscopy on nanowire solar cells 56
5.3 Simulations and Mie scattering 59
5.4 Conclusion 63
6 DIRECTIONAL AND POLARIZED EMISSION FROM NANOWIRE ARRAYS 65
6.1 Introduction 65
6.2 Measurement description 67
6.3 Results and discussion 67
6.3.1 Directional and polarized emission 67
6.3.2 Polarization anisotropy 72
6.3.3 Influence of surrounding array 75
6.4 Conclusion 77
7 STRONG DIAMETER-DEPENDENCE OF NANOWIRE EMISSION COUPLED TO WAVEGUIDE MODES 79
7.1 Introduction 79
7.2 Sample and measurement 80
7.3 Waveguide mode dispersion and polarization 82
7.4 HE_{11} mode interference 84
7.5 Conclusion 85
8 HIGH REFRACTIVE INDEX OF WURTZITE GAP MEASURED FROM NANOWIRE FABRY-PÉROT RESONANCES 87
8.1 Introduction wurtzite GaP nanowires 87
8.2 Sample description 88
8.3 Effective mode index 88
8.4 Bulk index of wurtzite GaP 89
8.5 Conclusion 92

BIBLIOGRAPHY 95
LIST OF SYMBOLS AND ABBREVIATIONS 111
SCIENTIFIC SUMMARY 113
WETENSCHAPPELIJKE SAMENVATTING 115
SAMENVATTING VOOR IEDEREEN 117
LIST OF PUBLICATIONS 119
ACKNOWLEDGEMENTS 121
CURRICULUM VITAE 125

1 INTRODUCTION

In this chapter we introduce the topic of nanowire solar cells, starting off by sustainable energy. We explain the need and progress of solar energy and describe the development of photovoltaics. Semiconductor nanowires are introduced as elongated crystals which show characteristic interaction with visible light. This property makes them interesting for optoelectronic devices such as solar cells. At the end of the chapter, we describe the outline of this thesis.

1.1 SUSTAINABLE ENERGY

The average wealth and life standards of the earth's citizens has been increasing continuously for many decades. Together with technological development a rapidly increasing demand for energy has arised, mainly in the form of fuels and electricity. Since the industrial revolution fossil energy sources – coal, natural gas and oil – have been dominating the general energy supply. Already in the 19th century scientists such as Joseph Fourier [1] and Svente Arrhenius [2] developed knowledge about the existence of the greenhouse effect. This effect describes how greenhouse gases – especially carbon dioxide (CO_2), water vapor (H_2O) and methane (CH_4) – in the atmosphere transmit visible solar radiation, but reflect the infrared heat radiation from the earth. Along with other processes, this causes an increase of the average temperature on earth. It was Alexander Graham Bell who wrote in 1917 that "the unchecked burning of fossil fuels would have a sort of greenhouse effect" [3]. In the 20th century the scientific knowledge about the relation between fossil fuel burning and the greenhouse effect developed. In 1972 John Sawyer published a review entitled "Man-made carbon dioxide and the greenhouse effect" [4], in which he accurately predicted the human-induced temperature increase on earth until 2000. In the last decades of the 20th century, more and more evidence was presented for human-induced or anthropogenic climate change. Presently, there is consensus among the scientific community about the existence of human-induced climate change [5, 6]. Stopping anthropogenic climate change is identified by the United Nations as one of the major challenges of the twenty-first century. The concentration of CO_2 is often used as an indicator for the temperature on earth; its annual minimum has surpassed 400 ppm in 2015, which is the highest annual minimum ever measured.

The rise in temperature of the last two centuries will probably continue due to several loop processes and memory effects in the earth's climate system. However, to slow down the temperature increase we need to reduce the emission of greenhouse gases as much as possible.

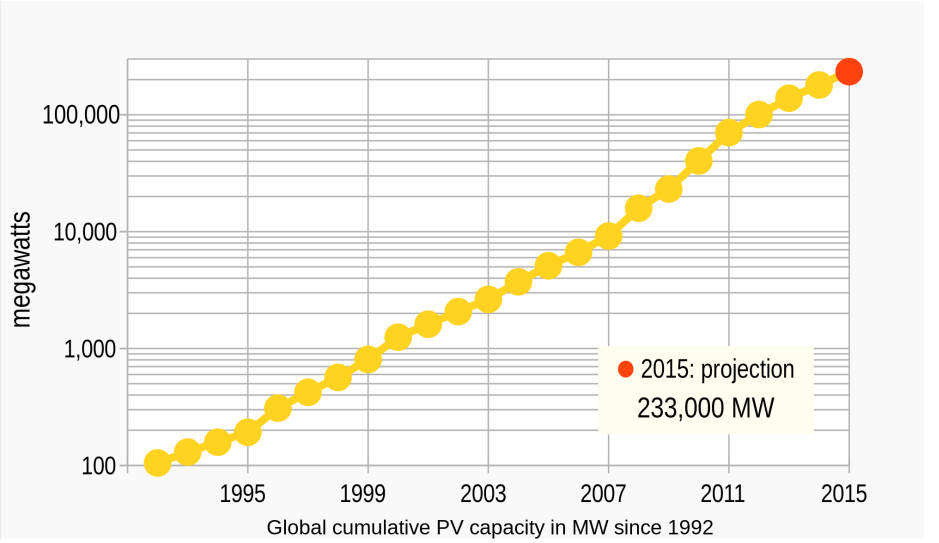

Figure 1.1: The amount of globally installed photovoltaic capacity has doubled every two years since 1990. Figure reproduced from ref. [8].

There are two basic ways to do so: the first, and most important, is the reduction of energy consumption. This is related to a change in the general human behavior and efficiency enhancements in basically all energy-consuming devices. Since it is not likely that people will reduce their energy usage back to levels of the eighteenth century, we additionally need a second solution: decoupling greenhouse gas emission from energy usage, by stopping to burn fossil fuels. Therefore, we need alternative sources for fuels and electricity, which limit the greenhouse gas emission to an absolute minimum.

A wide range of these alternative or sustainable energy sources has been investigated. The most promising alternative fuels are biofuels, biomass, and hydrogen. The most mature non-fossil source of electricity is nuclear fission. This energy source represents a large reduction of greenhouse gas emission with respect to fossil energy and provides a reliable and efficient energy production. However, nuclear fission involves a risk regarding the radioactivity of the reactor and the waste, which makes it an impopular option. Even cleaner are energy sources that make use of the natural landscape and local circumstances, such as water power, tidal energy, wind energy and solar energy. In practice, it is expected that a combination of these sources will be necessary to eventually provide the entire global energy supply [7], to ensure any-time availability and reliability.

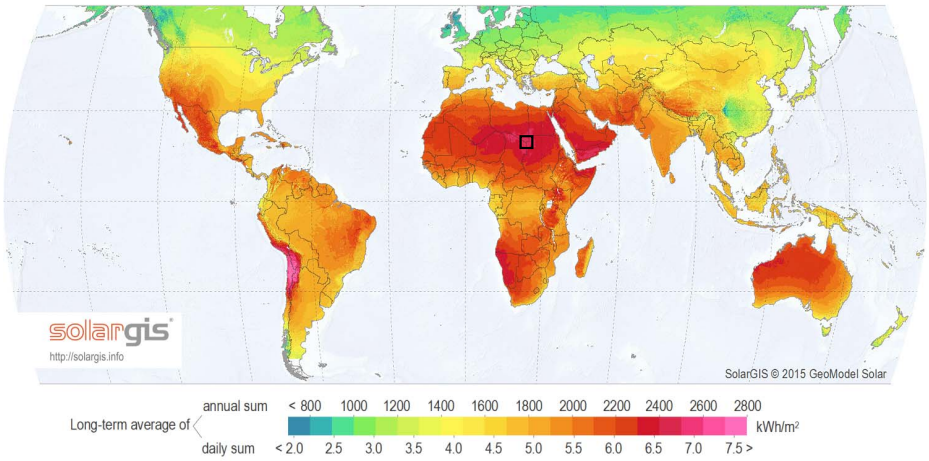

Figure 1.2: Global horizontal irradiance. The black square shows that covering a fraction of the Sahara desert with state-of-the-art solar panels would be sufficient to supply enough power for the world. The color scale indicates the irradiance per unit area in kWh/m^2. Reproduced under Creative Commons license from ref. [9].

1.2 PHOTOVOLTAICS

The emphasis of this thesis is on solar energy, but more specific on photovoltaic devices or solar cells (we will use these terms as synonyms, although there are other types of solar cells available, which we will not address). These devices convert sunlight directly into electricity. The share of photovoltaics (PV) in the global electricity market has increased to 1 % in 2015, accounting for a global installed capacity of 233 GWp, which has doubled every two years since the early 1990's [8] (Figure 1.1). The potential of solar energy is that it can power the world. The amount of energy that the sun delivers onto the earth's surface in a single hour is enough to provide the energy demand of the entire globe in a full year. It can be calculated that an equivalent area of 470 km x 470 km covered with 25% efficient solar panels produces enough energy to cover the global energy demand (Figure 1.2). Of course, efficient storage and transport of solar energy is required, but these are fundamentally feasible technological challenges.

The development of solar cells has started with the discovery of the photovoltaic effect, as discovered by Edmund Becquerel in 1839 [10]. This effect describes the process of a photon which excites an electron, generating an electrical current. This notion led to the invention of the first selenium solar cell by Charles Fritts in 1883 [11]. This cell had a power conversion efficiency of no more than 1%, which means that from the incident solar irradiation onto the cell only 1% was converted into electrical energy. Via the invention of the pn-junction in silicon by Russell Ohl in 1940 [12], solar cell development speeded up. The first solar cells were fabricated at Bell Labs for space applications. These cells had efficiencies of about 6% [13]. Afterwards,

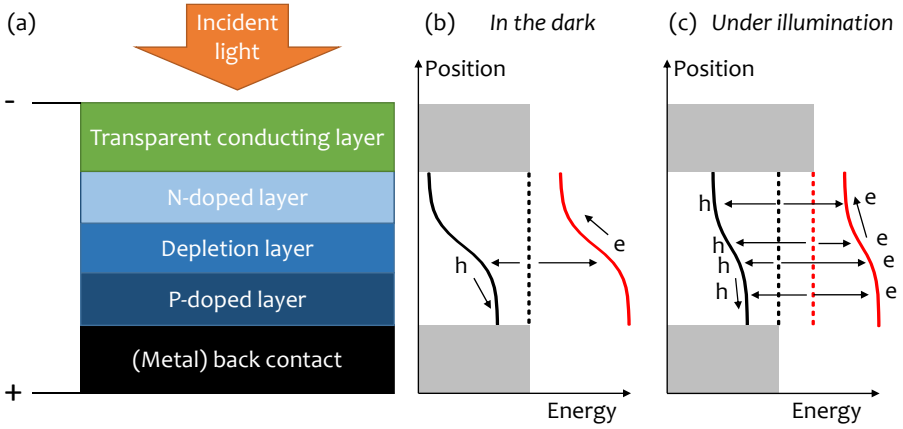

Figure 1.3: (a) A schematic representation of a simple semiconductor pn-junction solar cell. At the right side the band diagram is depicted, both in the dark (b) and under illumination (c). The dashed lines indicate the (quasi-)Fermi energy level(s) and the solid curves are the valence (black) and conduction (red) bands of the semiconductor.

efficiencies have rapidly increased up to the record for a single junction solar cell of 28.8% [14]. Higher efficiencies have been reached by combining different materials, to absorb different parts of the solar spectrum. This concept of multi-junction solar cells has led to a maximum efficiency of 46.0% under concentrated sunlight, in 2014 [14].

Nowadays, the PV market consists of different branches: first-generation cells, which have dominated the global market since the beginning: they consist of crystalline silicon solar cells, with efficiencies of typically 15-20%. The second generation is considered to be much cheaper cells, such as amorphous silicon or organic solar cells, with efficiencies that barely surpass 10%. In recent years, massive subsidies in China and consequent overproduction of solar cells has caused a decrease in the prices of silicon. This has undermined the main advantage of the second generation cells, and it is expected that cells with efficiencies below 20% will not overcome the status of a niche market. The third generation solar cells include different technologies that promises very high efficiency solar cells [15]. They include quantum dot solar cells, multi-junction solar cells, hot-carrier cells and other emerging strategies. This field has been pushed forward by improved fabrication methods, industrial development and developing scientific knowledge. However, only multi-junction cells have proven to be a cost-effective concept which is commercially available. In this thesis, we will only consider solar cells consisting of a single junction.

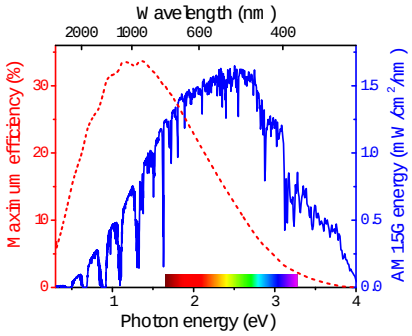

Figure 1.4: AM1.5 global spectrum (blue, solid) and maximum energy conversion efficiency (red, dashed), as a function of the material's band gap energy (after ref. [17]). The range of human-visible light is depicted by the colorbar.

1.2.1 *Working principle of single junction solar cell*

A pn-junction solar cell is schematically depicted in Figure 1.3. In simple terms, light (or, alternatively, a photon) from the sun falling onto a solar cell can either be reflected, transmitted or absorbed. In the first two cases, the photon is lost for the generation of photocurrent. If the photon is absorbed in the active region, an electron is released from its position in the semiconductor, carrying the energy through the cell. Similarly, vacancies in the electron clouds also carry energy, acting as the opposite of electrons, and are named holes. The electron and hole are separated by the internal electric field and can be collected at the cell's contacts, resulting in a net photocurrent, which can be stored or fed into the grid.

1.2.2 *Solar spectrum*

The sun emits a spectrum which can be approximated by a black-body emission at a temperature of 5800 K. However, there is a significant absorption by the gases in the earth's atmosphere, causing sharp spectral features. The spectrum that reaches the earth's surface is called the air mass 1.5 global (AM1.5G) spectrum. Obviously this spectrum varies depending on the location, time and day of the year. In this thesis we take the standard reference spectrum of the American Society for Testing and Materials (ASTM) [16]. This spectrum is depicted by the blue curve in Figure 1.4.

Table 1.1: Properties of solar cell materials compared. Information retrieved from ref. [18], unless otherwise specified.

	Si	InP	GaAs
Band gap[1] (eV)	1.12	1.344	1.424
Absorption coefficient at 2.5 eV (cm^{-1})	$1.5 * 10^4$	$1.5 * 10^5$	$7 * 10^4$
Mobility holes / electrons ($cm^2V^{-1}s^{-1}$)	450/1400	200/5400	400/8500
Surface recombination velocity (cm/s)	$10^2 - 7 * 10^4$	$10^3 - 10^6$	$5 * 10^4 - 5 * 10^6$
Abundance in earth's crust (ppm) [19]	270000	0.25 (In), 1050 (P)	19 (Ga), 1.8 (As)
Record solar cell efficiency (%) [14]	25.7	22.1	28.8

[1] at room temperature, for zincblende material

1.2.3 *Materials*

The solar spectrum sets the optimum band gap for a single junction solar cell. The band gap should be low enough that a large number of solar photons have sufficient energy to excite electrons, but high enough such that a large voltage is built up, which enables the energy extraction from the cells and prevents the energy to be emitted as heat. In fact, the limiting efficiency is given as a function of the band gap energy, as shown in Figure 1.4.

From here we can see that the efficiencies above 33% can be reached only with materials which have a band gap between 1.11 and 1.45 eV. The materials that stand out in this range are silicon (Si), indium phosphide (InP) and gallium arsenide (GaAs), on which we will emphasize our analysis. These materials each have their own interesting properties, which we have summarized in Table 1.1.

In our lab we only fabricate solar cells made of InP, which will therefore be the material of emphasis in this thesis.

1.2.4 *Absorption and emission*

It is evident that the first requirement for a good solar cell is a high absorption. However, having a simple planar solar cell induces reflection losses that can be up to 25-30%. With advanced strategies, it is possible to absorb 95-99% of the incident light with energy beyond the band gap [20–22]. To achieve this 'trapping of the light', one can use anti-reflection coatings [23–25], improving surface roughness by micro- or nanopatterning [26–28], metal or dielectric nanoparticles at front or back side [29–34], or nanostructuring the absorber layer itself, by using micro- and nanowires [35–38], nanopillars [39], nanocones [40, 41], nanodomes [42], and many other nanostructures [43, 44]. The small structures support optical resonances which enhance ab-

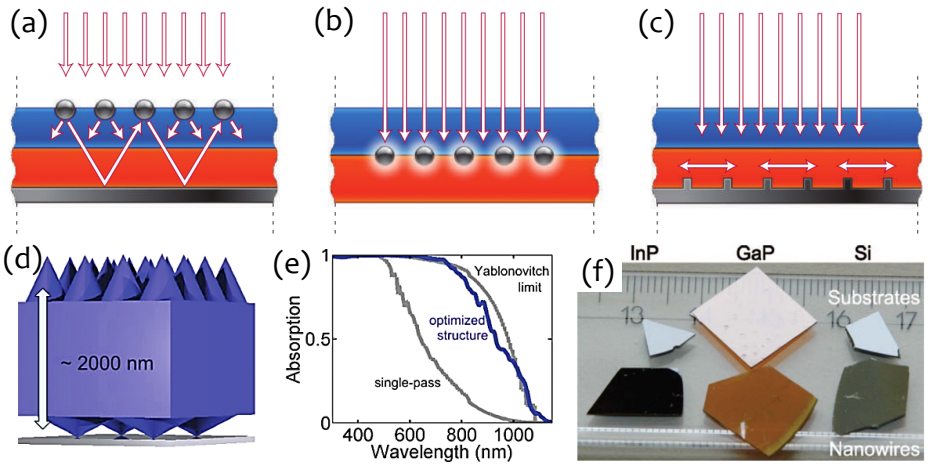

Figure 1.5: Nanostructures for absorption enhancement in photovoltaics. (a-c) metal nanoparticles at the front, middle or back side of the cell can scatter the light (a), locally enhance the electric field (b) or promote coupling of the light to photonic modes in the lateral direction in the cell (Figures taken from ref. [33]). (d,e) An optimized combination of conical nanostructures at the front and back side of a thin silicon cell enhance absorption to values close to the Yablonovitch limit (Figures taken from ref. [28]). (f) Photograph of bare substrates made of three different materials (top), together with equal substrates with nanowires grown on them (bottom), showing the strong anti-reflective properties of the nanowires (Figure taken from ref. [45]).

sorption and scattering of light. If properly designed, they can allow for a much higher local absorption than would be expected from their size. A couple of examples of nanostructures for improved absorption can be found in Figure 1.5.

Since a couple of years, the solar cell community has realized that just a high absorption and (obviously) a high optical quality of the material are not enough to guarantee a very high efficiency. The other aspect that needs a careful design is the luminescent emission of the solar cell, which ensures a high open circuit potential V_{OC}. Martin Green has shown that the cell efficiency can be correlated with the external radiative efficiency η_{ext} [46]. This quantity is defined as the ratio between the number of radative recombination events that lead to photons emitted out of the device R_{ext} and the total number of recombination events R_{tot}, which can be separated into a radiative and a nonradiative rate, i.e. $\eta_{ext} = \frac{R_{ext}}{R_{tot}} = \frac{R_{ext}}{R_{rad}+R_{nrad}}$. In ref. [47], Miller *et al.* motivated why this η_{ext} is of crucial importance.

The reasoning behind this stems from the basic equation for V_{OC}: $V_{OC} \approx \frac{k_B T}{q} \ln \frac{J_{SC}}{J_0}$, where k_B is Boltzmann's constant, T the cell temperature and q the electron charge. J_0 is proportional to the total recombination: $J_0 = q(R_{rad} + R_{nrad})$. Therefore, maximizing voltage means minimizing J_0, thus minimizing recombination. However, at open circuit conditions (V_{OC}) every device

needs to emit light in order to be in thermodynamic equilibrium with its environment. There is no way to avoid this. Therefore, in order to optimize η_{ext}, we need to make sure that the only recombination is the necessary and unavoidable radiative recombination. Any nonradiative recombination reduces V_{OC}. Therefore, besides being a good absorber, a solar cell needs to be designed to be an efficient light-emitting device at V_{OC}. This idea may be very counterintuitive: a solar cell needs to emit (rather than trap) the internally generated light as soon as possible. In Section 2.1 we will explain and mathematically derive this phenomenon in detail.

A significant loss factor in the solar cell V_{OC} is the increased entropy of the photons. [48–52]. Direct incident light from the sun has a very narrow spread in angle, while re-emitted light from the cell is typically sent into all directions. Adding a mirror to the back side of the cell reduces the emission range to the upper hemisphere, but a loss of hundreds of millivolts in the V_{OC} remains [53]. Therefore, angular restriction of the emission from a solar cell has been identified as a potential V_{OC} improvement [54, 55], but it can only work for cells with a very high internal radiative efficiency (η_{int} >0.9) [50]. This loss factor can be understood by the fact that photons re-emitted outside the incident light cone are lost and increase the total photon entropy, which reduces the maximum energy that can be extracted. Voltage enhancement by angular restriction has been demonstrated using a dielectric multilayer stack [56] and a parabolic reflector [57] recently, but the effect was limited to a few millivolts. Naturally, also concentrated solar cells take advantage in the V_{OC} from redirecting the emission into a narrow angular cone. Equivalently, you can say that in concentrated cells the incident and outgoing angular distribution of the light are matched, which minimizes the voltage loss due to photon entropy. To the best of our knowledge, there have not been more efforts to modify the angular emission pattern of solar cells, without using external optics. Semiconductor nanowires modify the angular pattern of the emission [58, 59], which could be an additional advantage for their use in solar cells, next to their anti-reflective properties. We will now discuss these structures in more detail.

1.3 SEMICONDUCTOR NANOWIRES

Semiconductor nanowires are nanosized crystals which have a characteristically large aspect ratio. Two arrays of nanowires are shown in Figure 1.6. Two of their three dimensions are typically on the order of tens or hundreds of nanometers, while their third dimension can range between microns and tens of microns. The relevance of nanowires for optical applications such as solar cells emerges from their diameter, which is on the order of the wavelength of visible light. This causes a strong resonant interaction between nanowires and light, giving rise to many interesting optical effects.

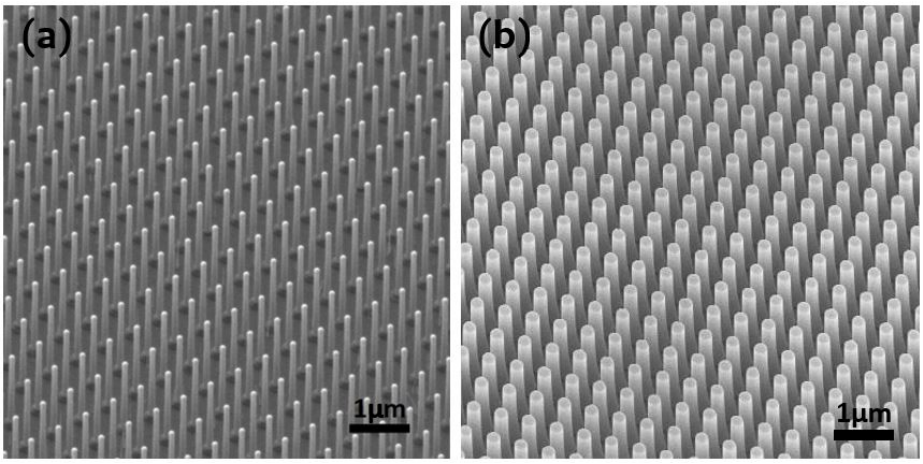

Figure 1.6: Semiconductor nanowire arrays, made of InP, fabricated by (a) VLS-growth and (b) dry etching.

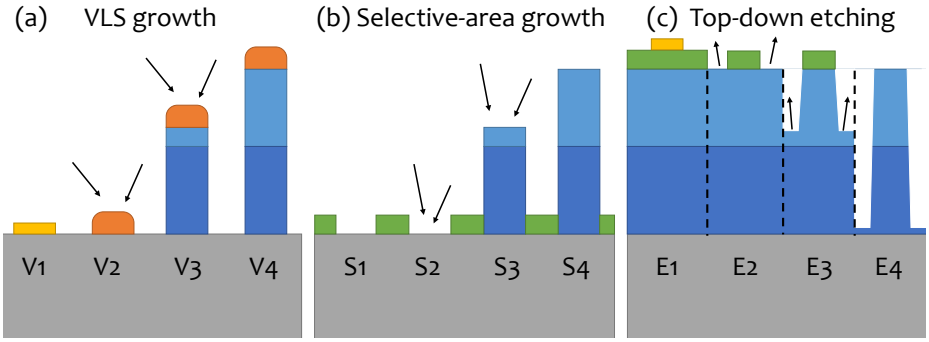

Figure 1.7: Nanowire fabrication methods. The fabrication steps are described in the text.

1.3.1 *Fabrication methods*

Our InP and GaP nanowires are grown in a Metal-Organic Vapor Phase Epitaxy (MOVPE) reactor. Three of the most important methods to fabricate nanowires are described below. All three of them were used to fabricate some of the nanowires that were used in the experiments of this thesis. The methods are schematically shown in Figure 1.7.

1.3.1.1 *Vapor-liquid-solid (VLS) growth*

This method (as depicted in Figure 1.7a) was introduced by Wagner and Ellis in 1964, [60] to grow so-called 'nanowhiskers'. The key point of this technique is the use of a liquid metal particle, which allows for lower growth temperatures. The method attracted a lot of attention in the end

of the 1990's, when improved VLS-growth rapidly expanded the research field of nanowires. Most common is the use of gold catalysts (which is what was done in the VLS-grown nanowires of this thesis), although some groups have reported the use of other catalyst materials. The VLS-method consists of the following steps:

v1 Gold catalyst particles are deposited on a substrate. Their positions and size can be controlled by means of colloids from a solution, nanoimprint lithography or electron-beam lithography.

v2 As the substrate is heated inside a growth reactor the particle melts. When precursor gases are inserted in the reactor, the group III material (In/Ga) is adsorbed in the catalyst droplet, forming an alloy.

v3 After supersaturation of the group III material inside the droplet, a crystal is formed at the droplet-substrate interface. As such, the droplet is lifted and a nanowire starts growing. The composition of the precursor gases can be modified to introduce dopant atoms or completely change the nanowire composition.

v4 The size of the droplets ensures a homogeneous diameter. Sidewall growth can be avoided by in situ HCl etching during the growth [61]. After the growth, the catalyst particle can be removed if required [62].

1.3.1.2 *Selective-area (SA) growth*

The method of selective-area epitaxy for fabricating nanowires was first demonstrated by Motohisa *et al.* from Hokkaido University [63, 64] and was later finetuned by Gao *et al.* from Australian National University [65]. The method uses no catalyst particle, but a dielectric mask (such as silicon nitride) (Figure 1.7b). Because of the absence of a catalyst, the growth takes place at much larger temperature than VLS-growth. This minimizes also the incorporation of carbon atoms which are defects. The method includes the following steps:

s1 A dielectric mask is grown on the substrate, in which nanosized holes are defined. Their positions and size can be controlled by means of colloids from a solution, nanoimprint lithography or electron-beam lithography.

s2 As the substrate is heated inside a growth reactor the growth is started, only inside the holes. The growth rate is limited by the diffusion of the atoms over the surface.

s3 Similar as in VLS-growth, the composition of the precursor gases can be modified to introduce dopant atoms or change the nanowire composition.

s4 The size of the hole determines the nanowire diameter. However, the growth mechanism is a complicated interplay between radial and axial growth, which is not yet completely understood.

1.3.1.3 *Dry plasma etching*

Etching is an indirect way of creating high quality nanowires, but has the advantage that it allows for directly comparing the nanowires with planar material (because they are made in the same growth run. In this case, silicon nitride disks are used as a mask for inductively coupled plasma (ICP) etching, to end up with a periodic array of tapered nanowires which have larger diameter at the bottom than at the top (Figure 1.7c). The nanowires are obtained as follows:

E1 Planar layers (e.g. doped layers) are grown on top of a wafer. These layers have a higher material quality than the wafer itself. A silicon nitride layer is grown by PECVD on top of the planar layer. Afterwards, nanoimprint lithography is used to define an array of chromium disks on top of the silicon nitride.

E2 Via reactive-ion etching the chromium array is transferred into the silicon nitride, creating disks with a similar size. Subsequently, the chromium is removed by oxygen plasma etching.

E3 When exposing the layers to the plasma in the reactor, the material is etched away from the areas which are not covered by the silicon nitride. The etching happens only in the vertical direction, giving rise to the elongated nanowire shape.

E4 When the etching is stopped, nanowires are obtained with a well-controlled length and a dopant profile resembling the profile of the initial planar layers.

The growth methods have the advantage that strain is relaxed in the lateral direction. This makes it possible to grow materials with different lattice constants on top of each other with less strain-induced defects. This phenomenon was theoretically investigated by Glas [66]. Many groups have investigated combining different materials in the same nanowire (or the growth of nanowires on top of substrates of a different material). An example of this was the growth of single nanowires combining silicon, GaP and GaAs, as demonstrated by Hocevar *et al.* [67] and shown in Figure 1.8.

1.3.2 *Optoelectronic applications*

The potential of semiconductor nanowires for optoelectronic applications started at the early 1990's at Hitachi Research in Japan with the so-called quantum wires (diameters of around 100 nm, so not really exhibiting quantum effects). The wires were made of GaAs and exhibited a pn-junction with a quality comparable to its planar counterpart and emission polarized parallel to the wire [68, 69]. Afterwards, the control over the growth improved, enabling ZnO nanowire lasers [70, 71]. InP nanowires were identified as powerful building blocks for optoelectronic devices [72], which show a strongly polarized emission and absorption [73]. Also structures for other applications were investigated, such as heterostructures [74, 75] and emitting quantum dots [76, 77] embedded inside nanowires. In 2005 the first nanowire solar cell followed [78].

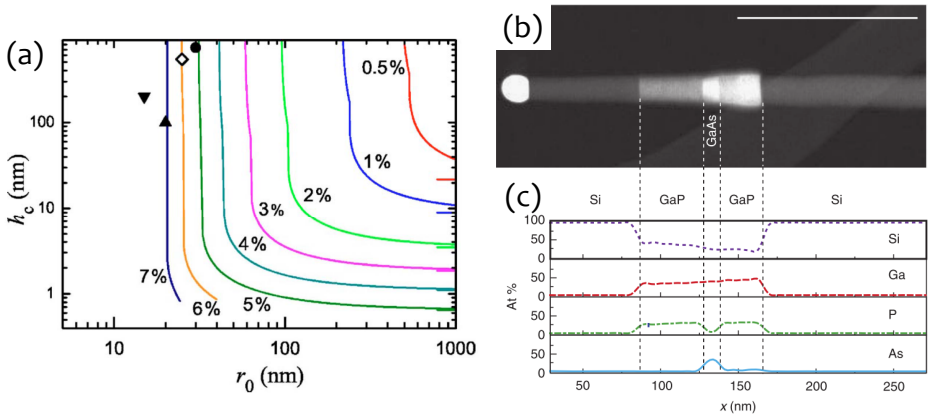

Figure 1.8: Strain relaxation enables combination of different materials. (a) Calculated variation of the critical thickness h_c of a segment growing on top of a nanowire as a function of the wire radius r_0, for varying lattice mismatch (given in percent near each curve). Figure adopted from ref. [66]. (b) High angle annular dark field (HAADF) image of a nanowire consisting of different materials (scale bar is 200 nm). (c) is an EDX scan along the growth axis from the nanowire in (b). Figures (b) en (c) were adopted from ref. [67]

1.4 NANOWIRE SOLAR CELLS

For a macroscale power source a large array of nanowires is preferred over a single nanowire behavior. Vertical nanowires show better light absorption than horizontal nanowires due to the coupling of the incident light to waveguide modes supported by the elongated nanowire geometry [41, 79, 80]. However, a single nanowire has a maximum absorption cross section of a few square microns [81]. Therefore, arrays of vertical nanowires are the basis of any macro-sized nanowire solar cell. The typical geometry, as depicted in Figure 1.9, was shown for the first time in 1992 [68], in the context of an light-emitting diode (LED) device. This concept was embraced as an advantageous solar cell design in 2002 [82]. The first grown nanowire array solar cell device was demonstrated in 2007 [83] (made of silicon) and had a power conversion efficiency of only 0.1%. After large developments in material purity, dopant tuning, size and shape optimization, and device processing, the record power conversion efficiency of nanowire solar cells is now, only 9 years later, set at 17.8%. The development of efficiencies of several nanowire solar cell research groups is depicted in Figure 1.10. The progress has brought nanowire solar cells from a niche scientific idea towards a mature device with properties comparable to their planar counterparts.

It is important to clearly define when a nanotextured solar cell is considered a nanowire solar cell. In this work, we use the following definition: if the substrate has no active role in the cell (other than a mechanical carrier and hole conductor), the cell is considered to be a

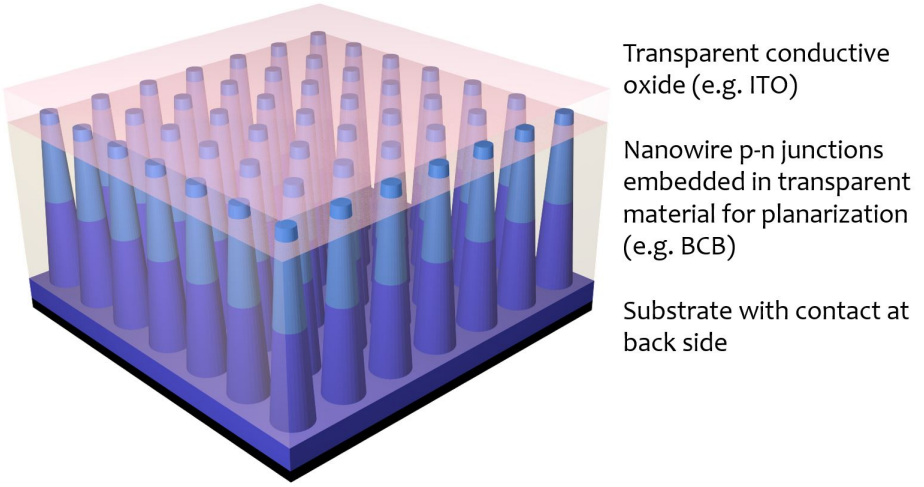

Figure 1.9: Typical axial junction nanowire solar cell geometry. In this case the nanowires have a tapered (conical) shape.

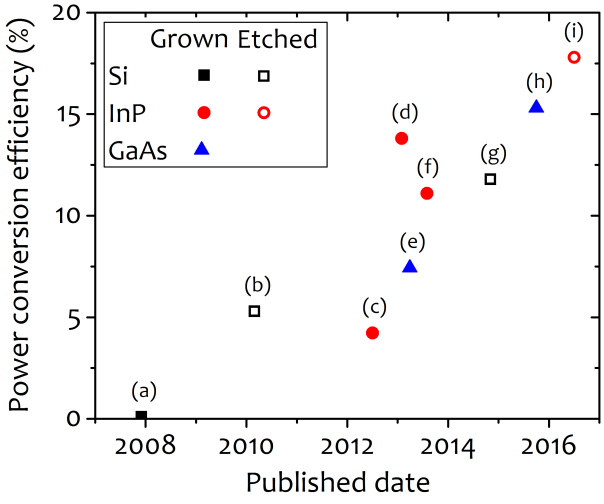

Figure 1.10: Development of published nanowire solar cell efficiencies. The data points are taken from the following references: (a) [83], (b) [37], (c) [84], (d) [85], (e)[86], (f) [87], (g) [88], (h) [89], (i) [90].

nanowire solar cell. Or, alternatively, it is considered a nanowire solar cell if and only if the nanowires form the active part themselves, both in light absorption and in charge separation. So, the vast majority of the light needs to be absorbed in the nanowires which include the junction. In such way, we can distinguish active-nanowire solar cells from planar cells with an antireflective nanostructured top layer.

1.4.1 *Nanowire photonics*

Initially, the strong polarization of the absorption and emission of light from nanowires was explained in the quasi-static approximation, assuming that the electric field inside the nanowire was constant [73]. This, however, turned out to be only true for nanowires that are much thinner than the wavelength [91]. Researchers realized that the interaction between light and nanowires needs a different description. The experimental demonstration of nanowire lasers indicated that the nanowires form an efficient cavity [70, 71]. Maslov *et al.* explained this in terms of waveguide modes supported by the nanowire geometry [92]. From the waveguide mode dispersion they predicted far-field angular emission patterns of the specific mode being excited [93, 94]. The polarization anisotropy was also explained in terms of the diameter-dependent waveguide modes [95] and dielectric contrast between nanowires and environment [91, 96]. These theories were confirmed by polarization-dependent photoluminescence measurements [97, 98]. Van Weert *et al.* explained the polarized emission in terms of Mie theory of infinite cylinders [99, 100]. Due to the particular role of nanowires in concentrating far-field incident light into small volumes they were referred to as 'antennas' for light [101–103]. Recently, it was shown that the different descriptions, both waveguide modes and Mie theory, are equivalent when the wave vector of the light is perpendicular to the long axis of the nanowire [104, 105]. In contrast, when the wave vector is close to parallel to the nanowire, the guided mode description of the interaction between light and nanowire prevails [80]. Therefore, to analyze the absorption and emission of the light, proper understanding and modelling of the nanowire waveguide modes is of seminal importance.

1.4.2 *Absorption of light in nanowires*

When the wave vector of the incident light is (nearly) parallel to the long axis of the nanowire, the absorption of the nanowires is governed by the HE_{11} mode [41, 80]. Nicklas Anttu and coworkers carefully modelled the absorption in InP nanowires by means of a scattering matrix method [79, 106, 107]. They (and others) showed that for InP the nanowire array dimensions that optimize the absorption are a diameter of 170-180 nm and a array period of about 360-400 nm [79, 108]. This would result in more than 90% absorption of solar photons with energy beyond the band gap of InP. In the model a nanowire length of 2 μm was used. The absorption

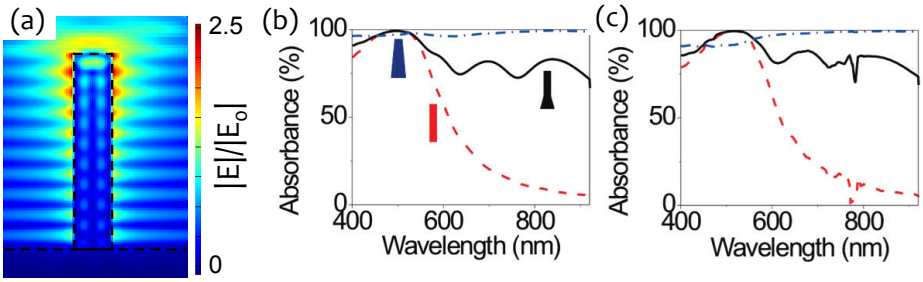

Figure 1.11: Absorption in nanowires. (a) FDTD simulation of a 2.5-micron long cylindrical nanowire with a 200 nm diameter placed on top of a substrate. The nanowire is excited with a plane wave from the top at a wavelength of 532 nm. (b,c) FDTD simulations of the absorbance in cylindrical (red, dashed), base-tapered (black, solid) and tapered (blue, dash-dotted) nanowires, both under normal incidence (b) and at 30 degrees oblique incidence (c). (b,c) were adopted from [21].

achieved in the nanowire array is far larger than the absorption of a planar layer with the same thickness or volume as the nanowire array [108]. The reason for this enhanced absorption is the concentration of the incident field inside the nanowire (Figure 1.11a). In fact, this concentration is caused by the high refractive index of the nanowire, which gives rise to strongly confined waveguide modes.

Diedenhofen *et al.* demonstrated that tapered and base-tapered nanowires show a greatly enhanced absorption with respect to cylindrical nanowires [21]. When the nanowire shape is different from the cylindrical geometry, there is no analytical approach and Finite-Difference Time-Domain (FDTD) or Finite Element Method (FEM) simulations are required to model its absorption (Figure 1.11). The enhanced absorption at the long wavelengths, close to the band gap of the material, was explained with the help of these simulations. This light has a long absorption length, and is more efficiently absorbed in the thicker parts at the bottom of the (base-)tapered nanowires. At the same time, the reflection at the top facet of the nanowire is low because its diameter is small there [21, 109]. Arrays of tapered nanowires are thus very efficient light absorbers, but pure crystal growth of such structures is not easy. Tapering is typically established by radial growth, but this has a high impurity density and therefore most growth studies were optimized for pure untapered nanowires [61, 110].

1.4.3 *Emission from nanowires*

It has been known since a long time that the emission of a nanostructured layer is typically much more intense than a planar layer [111]. The reason is the high refractive index mismatch between the emitting layer and the air on top, which causes a narrow escape cone for the photons inside the planar layer, and thus a high total internal reflection. Nanostructures can

overcome this problem by either randomly scattering the light, thus increasing the probability of escaping from the emitting layer [111], or by coupling to vertical guided modes within the nanostructure, which mediate vertical light propagation and, if properly designed, an efficient escape [112]. This property of nanostructures has evidently been of interest for LEDs, but is, as we have mentioned, also very relevant for photovoltaics. Nowadays, nanostructures such as photonic crystals [113, 114], nanowires [115], nanorods [112] or nanocones [116] are very promising to achieve high emission (or extraction) efficiencies in LEDs [117].

Single photon sources, as used for photonic integration for quantum communication, form yet another type of devices for which the escape probability of internally generated photons is important [118]. The use of semiconductor quantum dots are one of the most common ways of generating single photons. They are traditionally grown randomly in a bulk layer, but growing them in a controlled way inside a nanowire or nanorod offers many advantages in design flexibility and extraction efficiency [119–121]. Tapered nanowires combined with a gold mirror at the back side have boosted the extraction efficiency of quantum dots up to 72% [119]. The nanowire geometry causes coupling of the quantum dot emission to the fundamental guided mode [102] and the tapering allows for an adiabatic expansion of the mode, thus transferring the photons to air with near-zero reflectivity [122].

Tapered nanowires also ensure a Gaussian angular emission pattern in the far-field [123]. This emission pattern might be important for solar cells as well, as the angular spread of the emission influences the entropy losses of the photons. The angular emission pattern of nanowires is determined by the coupling of the emission to the waveguide modes and has been investigated in detail [58, 59, 103, 124, 125]. This emission will be addressed extensively in Chapter 6 and Chapter 7. It is suspected that nanostructures such as nanowires can not only increase the emission intensity, but also narrow the angular emission cone; both effects will enhance the solar cell voltage.

1.5 ADVANTAGES OF NANOWIRES FOR SOLAR CELLS

Nanostructures, or more specific, nanowires, offer a number of properties which make them interesting for applications in solar cells. We will address these properties in more detail in this thesis, but we summarize a number of advantages below.

ABSORPTION. If properly designed, nanowires absorb light very efficiently due to the antenna effect.

EMISSION. Nanowires do not suffer much from total internal reflection, which allows for a high emission probability.

SMALL ACTIVE VOLUME. A smaller active volume reduces the number of defects and impurities in comparison with planar counterparts.

DESIGN FLEXIBILITY. Growth of nanowires allows for a wider design flexibility, as the strain can relax in the lateral direction. This makes combination of materials with a large mismatch in the crystal lattice possible.

MATERIAL REDUCTION. Reducing the amount of material allows for a higher growth rate than planar layers, thus reducing costs. On top of that, nanowires can be released from their supporting substrate e.g. by embedding them in flexible polymer layers. In this way the expensive substrates can be re-used.

1.6 OUTLINE OF THE THESIS

This thesis deals with the photonic properties of semiconductor nanowires, aimed at utilization in photovoltaic cells. In this chapter the motivation, background and scientific field have been introduced.

In Chapter 2 we describe the theoretical efficiency and voltage limitations of solar cells and we give a brief description of single nanowire photonics, in terms of Mie resonances and waveguide modes.

In Chapter 3 we introduce the experimental methods that were used to obtain most results in this thesis. These are Fourier microscopy and time-reversed Fourier microscopy. We highlight also the calibration of the setup for quantitative photoluminescence measurements.

The next five chapters describe the experimental results. in Chapter 4 we prove that nanostructuring significantly enhances a solar cell's voltage, by reducing the active volume and thus the number of defects, and by enhancing the escape probability of the internally generated emission. We show the fundamental advantages of nanostructures over planar cells. The same solar cells are used in Chapter 5, where we describe the high photocurrent in the cells, which is due to forward scattering of the self-aligned textured ITO front contact.

After these two chapters we move to single nanowire photoluminescence measurements. In Chapter 6 we show that waveguide modes determine the direction and polarization of the nanowire emission. We show that by coupling the nanowire emission to three different modes we obtain different emission patterns and different polarizations. Chapter 7 elaborates on this concept and shows that the nanowire diameter is very important for this phenomenon, and that a change of a few nanometer in the diameter can induce a pronounced change in the emission directionality. The directionality and polarization of the nanowire emission is important for e.g. LEDs, but also for photovoltaics, as it affects the photon entropy.

Finally, Chapter 8 discusses a method to derive the refractive index from a material which is only available in the nanowire geometry. We use Fabry-Pérot modes in a photoluminescence spectrum to find that wurtzite gallium phosphide has a very high refractive index, which opens a pathway for interesting applications.

2

THEORETICAL BACKGROUND

In this chapter we will describe the theoretical formalisms that are used further on in the thesis. They are divided in two parts. In the first part, solar cell physics is introduced from a detailed balance model. We describe the theoretical limits and discuss the losses that determine the maximum solar cell power generation. In the second part, the propagation of light in nanowires and the emission from nanowires is modeled based on Mie resonances and waveguide modes.

2.1 SOLAR CELL PHYSICS

In the following section we describe the essential solar cell parameters. Similar descriptions are published elsewhere, e.g. in refs. [52, 53, 126–129].

2.1.1 *Detailed balance of photons/electrons*

The figure of merit for the power production of a solar cell is its power conversion efficiency η, defined as the ratio of its generated power density at the operating point P_{OP} and the incident power density coming from the sun P_{in}. P_{OP} is given by the product of the voltage at the operating point V_{OP} and the current density at the operating point J_{OP}. A current density versus voltage curve is shown in Figure 2.1. In this curve, the area enclosed by the dashed line and the axes is the extracted power density. We have also indicated the open-circuit voltage V_{OC}, which is the voltage at zero current, and the short-circuit current density, which is the current at zero voltage. They form a rectangle with area $V_{OC}J_{SC}$ (enclosed between dashed lines and axes). The ratio between P_{OP} and $V_{OC}J_{SC}$ is known as the *fill factor* (FF) of a solar cell. We can express η in terms of the introduced parameters:

$$\eta = \frac{V_{OP}J_{OP}}{P_{in}} = \frac{V_{OC}J_{SC}FF}{P_{in}}. \tag{2.1}$$

The limits for the solar cell parameters V_{OC}, J_{SC}, FF and η can be found by studying the flows of energy within the cell: the generation of charge carriers, the radiation from the cell into the surroundings, and the photocurrent extracted by the cell. The first researchers to use this 'detailed energy balance' method were William Shockley and Hans Queisser, who published a seminal article in 1961 [17]. They calculated the ideal solar cell efficiency and argued that, for

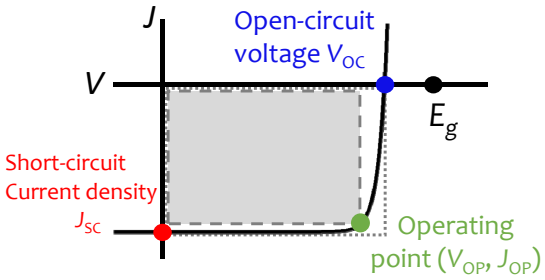

Figure 2.1: Typical current density-voltage characteristic of a solar cell. Indicated are the solar cell parameters V_{OC} and J_{SC} and the dashed, shaded gray rectangle $V_{OP}J_{OP}$ and dotted gray rectangle $V_{OC}J_{SC}$. The ratio of $V_{OP}J_{OP}$ and $V_{OC}J_{SC}$ defines the fill factor FF.

an ideal solar cell, all recombination needs to be radiative. In the ideal case it is assumed that the sun is a black body radiating at a fixed temperature and that the absorption in the cell is a step function, with unity absorption beyond the band gap and zero absorption below the band gap. As such, the limits are only a function of the cell temperature T and the material band gap E_g. The detailed balance equation can be written as

$$J = qR_{\text{gen}} - qR_{\text{rad}}. \tag{2.2}$$

Here, J is the extracted photocurrent density, q the electron charge, and $R_{\text{rad}} = R_{\text{ext}}$ is the (external) radiative emission flux (rate per unit area). The generation flux R_{gen} is, when every incident photon generates a free electron, equal to $\phi(E_g)$, i.e. the incident flux of AM1.5G photons above the band gap. The radiative emission flux is related to the potential difference of the electron and hole Fermi levels of the cell $\mu = qV$, by $R_{\text{rad}} = R_0(\exp(qV/k_BT) - 1)$, where R_0 is the radiative recombination flux in thermal equilibrium for a given band gap and temperature, defined following Planck's equation for blackbody radiation [51]:

$$R_0(E_g, T) = \frac{2\pi}{c^2h^3}\int_{E_g}^{\infty}\frac{E^2dE}{\exp(E/k_BT) - 1}. \tag{2.3}$$

Here, c is the speed of light, h Planck's constant, and k_B is Boltzmann's constant.

Using the considerations above, the detailed balance for an ideal cell equation becomes

$$J(V) = q\Big[\phi(E_g) - R_0(E_g, T)(\exp(qV/k_BT) - 1)\Big]. \tag{2.4}$$

J_{SC} is calculated for $V = 0$, giving $J_{sc} = q\phi(E_g)$.

For finding $V = V_{\text{OC,ideal}}$, Equation 2.4 is set to zero. We then get the well-known textbook equation

$$V_{\text{OC,ideal}} = \frac{k_BT}{q}\ln\left(\frac{J_{SC}}{qR_0}\right) = \frac{k_BT}{q}\ln\left(\frac{J_{SC}}{J_0}\right). \tag{2.5}$$

We see that in the ideal case, the only radiation is the black body radiation R_0, which depends on the temperature of the cell and its band gap energy. The fill factor FF can be approximated from the V_{OC} to [130]

$$\mathrm{FF} = \frac{qV_{OC}/k_BT - \ln(qV_{OC}/k_BT + 0.72)}{qV_{OC}/k_BT + 1}. \tag{2.6}$$

As derived using the formalisms above, the maximum values for the solar cell parameters are plotted as a function of the material's band gap energy in Figure 2.2.

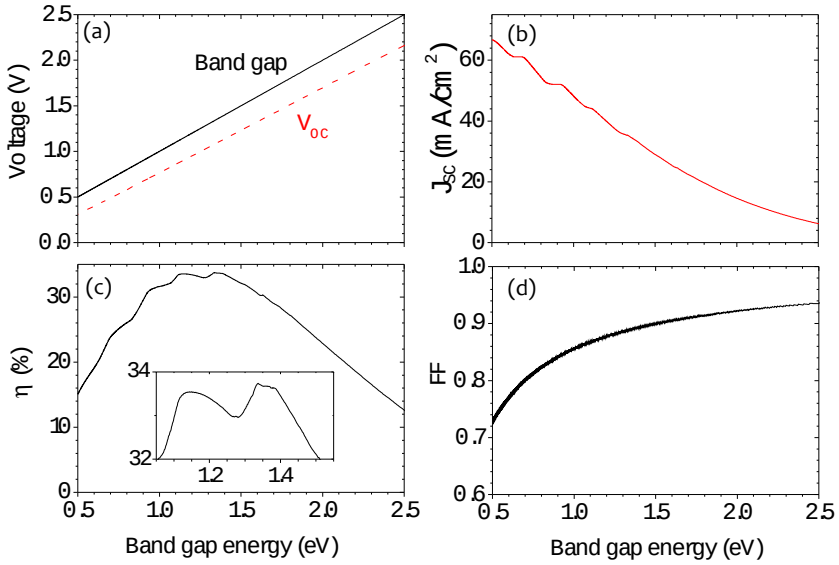

Figure 2.2: Maximum values for the solar cell parameters, calculated as a function of the semiconductor band gap: (a) open-circuit voltage, (b) short-circuit current, (c) efficiency, and (d) fill factor. The inset in (c) is a zoom in around the maximum efficiency.

2.1.2 *Losses in photovoltaic energy conversion*

Figure 2.2 shows the maximum conversion efficiency of a single junction solar cell, which is strongly dependent on the band gap energy. The maximum efficiency that can be reached is equal to 33.7%. This is the limiting efficiency at a band gap of 1.34 V. There are several mechanisms that limit the efficiency, which has been addressed in detail in the literature. Educative overviews can be found e.g. in refs. [52, 53, 128]. We have calculated the losses based on these references and plotted them in Figure 2.3. Following the labels in this figure, the losses are listed below.

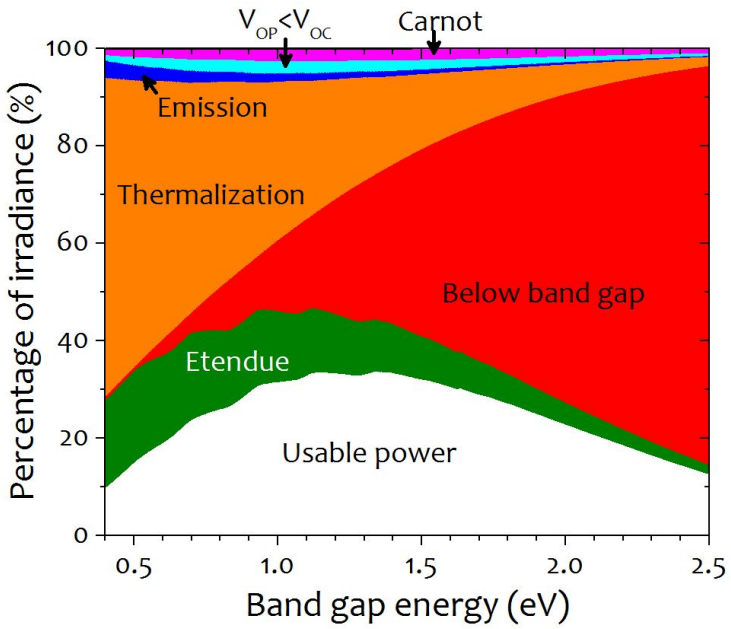

Figure 2.3: Percentage of the incident irradiance that is extracted as usable power (white), or lost (colored), as a function of the cell band gap. A single junction cell operating in the radiative limit is assumed, which has a perfect absorption beyond the band gap and zero absorption below the band gap.

CARNOT. As a solar cell is a thermodynamic engine, the maximum efficiency that can be achieved is limited by the Carnot efficiency. This loss is characterized by the temperature difference between the sun and the cell and is a fundamental loss which cannot be avoided.

$V_{OP} < V_{OC}$. The operating voltage is always lower than the V_{OC} due to the diode characteristics of the cell, which reduces also the usable power. This is an unavoidable loss.

BELOW BAND GAP. Photons that have an energy lower than the band gap pass through the cell without being absorbed. This loss can be minimized by using a very small band gap semiconductor.

THERMALIZATION. The maximum power that can be extracted from a photon that has an energy higher than the band gap is the band gap energy. The excess energy is lost to heat. Included in this loss is the thermal energy of the charge carriers, which is an important loss especially for small band gap cells. Fabricating cells with multiple junctions that have different band gaps can greatly reduce the thermalization losses and below-

band-gap losses, since the different junctions can account for different parts of the solar spectrum.

EMISSION. The photocurrent is reduced because of emitted photons. This is the case at the operating voltage, where the cell emits some light. This reduces the maximum extracted power slightly.

ETENDUE EXPANSION. The etendue is a measure for the angular distribution of photons. A large part of the loss is the entropy increase due to the difference in angular distribution of the incident photons and emitted photons. This loss is sometimes also called Boltzmann loss [53]. Using concentrated sunlight or employing angle restriction of the emission reduces this loss.

OTHER LOSSES. The losses above concern a solar cell operating in the radiative limit and having a perfect absorption beyond the band gap. When the absorption is lower than unity, the maximum extracted power will be reduced since the photocurrent decreases. Similarly, when non-radiative losses are present, the current and voltage are reduced which also results in a lower extracted power. All cells are affected by these two losses, that are caused by non-idealities. The external luminescence efficiency characterizes the non-radiative losses.

2.1.3 *External luminescence efficiency*

The ideal V_{OC}, as derived in Section 2.1.1, is reduced when not every recombination event results in the emission of a photon to the far field. This is characterized by the external luminescence efficiency η_{ext}, which is defined in terms of the external and non-radiative recombination rates, as [47]

$$\eta_{ext} = \frac{R_{ext}}{R_{ext} + R_{nrad}}. \tag{2.7}$$

It is related to V_{OC} by:

$$V_{OC} = \frac{k_B T}{q} \ln \frac{J_{SC}}{q R_{tot}} = \frac{k_B T}{q} \ln \frac{J_{SC}/q}{R_{ext} + R_{nrad}} = \frac{k_B T}{q} \ln \frac{J_{SC}}{q R_{ext}} \frac{R_{ext}}{R_{ext} + R_{nrad}} \tag{2.8}$$

$$= \frac{k_B T}{q} \ln \frac{J_{SC}}{q R_{ext}} + \frac{k_B T}{q} \ln(\eta_{ext}). \tag{2.9}$$

Here, R_{tot} is the total recombination rate per unit cell area.

η_{ext} can be written in terms of the internal luminescence efficiency η_{int} and the angle-, position- and energy-averaged photon reabsorption and escape probabilities $\overline{P_{abs}}$ and $\overline{P_{esc}}$. Here, $\overline{P_{abs}}$ is the probability for an internally emitted photon to be reabsorbed, and $\overline{P_{esc}}$ is the probability for a photon to escape from the device. In any practical device, there may also be a probability for a photon to be parasitically absorbed, e.g. in contacts [52]. This is characterized

by the angle-, position- and energy-averaged parasitic absorption probability $\overline{P_{\text{par}}}$. As these are all the possibilities for a photon in a cell, $\overline{P_{\text{abs}}} + \overline{P_{\text{esc}}} + \overline{P_{\text{par}}} = 1$.

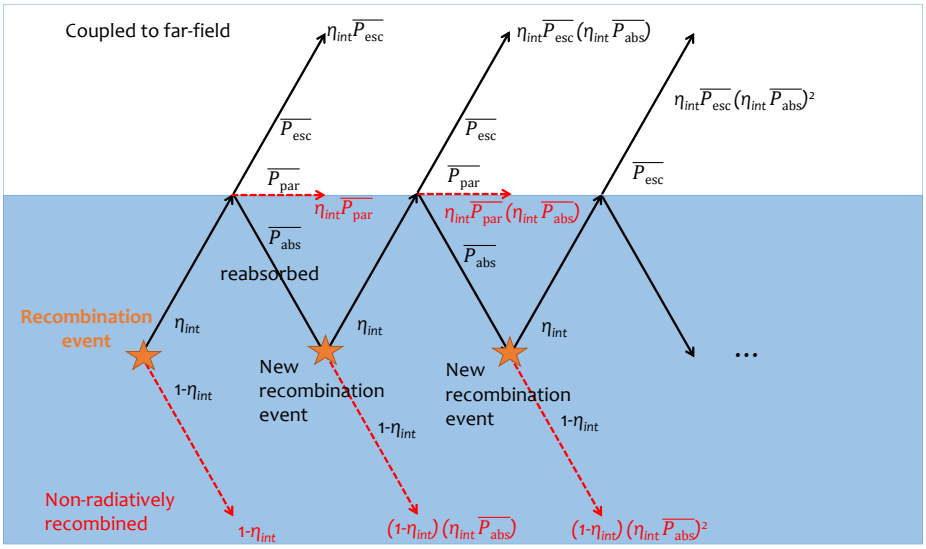

Figure 2.4: Total external luminescence efficiency, including multiple reabsorption-recombination events. The dashed red arrows and red expressions indicate photons that are lost.

The precise expression for η_{ext} can be intuitively derived as follows (schematically shown in Figure 2.4). When carriers recombine, this can be either radiatively or nonradiatively. In the first case, the photon may couple to the far-field with average photon escape probability $\overline{P_{\text{esc}}}$. Otherwise, it will be internally scattered or reflected, and eventually reabsorbed in the active region. The last possibility is that the photon is parasitically absorbed in different regions in the cell, which results in photon loss. After reabsorption in the active region, a new electron-hole pair is created, which again recombines, following the same luminescence and outcoupling efficiencies. This process can happen multiple times.

When summing all routes that lead to external luminescence, we get

$$R_{\text{ext}} = R_{\text{tot}}\eta_{\text{int}}\overline{P_{\text{esc}}}\sum_{n=0}^{\infty}(\eta_{\text{int}}\overline{P_{\text{abs}}})^n, \tag{2.10}$$

where R_{tot} is the total recombination rate. Similarly, the nonradiative recombination rate is

$$R_{\text{nrad}} = R_{\text{tot}}(1-\eta_{\text{int}})\sum_{n=0}^{\infty}(\eta_{\text{int}}\overline{P_{\text{abs}}})^n. \tag{2.11}$$

The loss rate due to parasitic absorption is

$$R_{\text{par}} = R_{\text{tot}}\eta_{\text{int}}\overline{P_{\text{par}}}\sum_{n=0}^{\infty}(\eta_{\text{int}}\overline{P_{\text{abs}}})^n. \tag{2.12}$$

Since parasitic absorption practically implies nonradiative recombination, we can write the total nonradiative recombination rate as

$$R_{\text{nrad,total}} = R_{\text{nrad}} + R_{\text{par}} = R_{\text{tot}}(1 - \eta_{\text{int}} + \eta_{\text{int}}\overline{P_{\text{par}}}) \sum_{n=0}^{\infty} (\eta_{\text{int}}\overline{P_{\text{abs}}})^n. \tag{2.13}$$

Following again the definition of the external luminescence efficiency from Equation 2.7, we end up with

$$\eta_{\text{ext}} = \frac{R_{\text{ext}}}{R_{\text{ext}} + R_{\text{nrad,total}}} = \frac{\eta_{\text{int}}\overline{P_{\text{esc}}}}{1 - \eta_{\text{int}} + \eta_{\text{int}}\overline{P_{\text{esc}}} + \eta_{\text{int}}\overline{P_{\text{par}}}}. \tag{2.14}$$

We can take the limiting cases for η_{int} in this expression, in the absence of parasitic absorption:

$$\lim_{\eta_{\text{int}} \to 1} \eta_{\text{ext}} = 1, \tag{2.15}$$

$$\lim_{\eta_{\text{int}} \to 0} \eta_{\text{ext}} = \eta_{\text{int}}\overline{P_{\text{esc}}}. \tag{2.16}$$

For a perfectly radiative material the escape probability is not relevant, i.e. each phooton will eventually escape the cell. For a poorly radiative material the escape probability is of equal importance as the internal luminescence efficiency. The latter approximation is valid when $\eta_{\text{int}} \lesssim 0.1$.

2.1.4 *Photon reabsorption*

An increase $\Delta\overline{P_{\text{esc}}}$ of the photon escape probability might imply a reduction in photon reabsorption $|\Delta\overline{P_{\text{abs}}}| \leq \Delta\overline{P_{\text{esc}}}$. In the ultimate case, without any parasitic losses, $|\Delta\overline{P_{\text{abs}}}| = \Delta\overline{P_{\text{esc}}}$. However, in this case still η_{ext} (thus V_{OC}) increases for $\eta_{\text{int}} < 1$. This can be understood by realizing the following: if every reabsorption-recombination event has a nonzero probability of photon loss (i.e. $\eta_{\text{int}} < 1$), an escaping photon is always preferred over a reabsorbed photon, in order to achieve maximum η_{ext} (thus V_{OC}). In other words: when we make it easier for photons to escape, the number of reabsorption-recombination events is reduced. In each of these events, there is a certain probability to recombine nonradiatively, which is detrimental for the V_{OC}. Therefore, enhancing the escape probability of the photons reduces the number of nonradiative recombination events, thus increasing η_{ext} and V_{OC} (as follows from Equation 2.14).

In the state-of-the-art planar GaAs cells (e.g. ref. [131]), it is claimed that the V_{OC} enhancement is mainly caused by enhanced photon recycling (or photon reabsorption). This causes an increase in the external luminescence efficiency, therefore in the V_{OC}. This is not in contradiction with the above: enhanced photon reabsorption (characterized by $\overline{P_{\text{abs}}}$) means either a reduced $\overline{P_{\text{esc}}}$ or a reduced $\overline{P_{\text{par}}}$. It was checked that $\overline{P_{\text{esc}}}$ did not decrease [132]. Therefore, the enhanced photon reabsorption (or photon recycling) is in this case equivalent to a reduction of the parasitic losses, and our conclusion that increasing $\overline{P_{\text{esc}}}$ is important holds.

In Chapter 4 we will discuss the implications of nanostructures (e.g. nanowires) on the solar cell voltage. The generated photocurrent of nanowire solar cells, depending on the cell geometry, will be discussed in Chapter 5.

2.2 SINGLE NANOWIRE PHOTONICS

To describe the interaction of light with semiconductor nanowires – as they are used in our solar cells – we address here a couple of theoretical frameworks that we will use in this thesis, namely Mie theory and waveguide modes.

2.2.1 *Mie theory*

The electromagnetic field in or around an arbitrary object can be calculated by solving Maxwell's equations and applying the boundary conditions. Solving these equations analytically can be complicated or even impossible. For particles much smaller than the wavelength, a Rayleigh approximation can be used, while geometrical optics is possible for particles much larger than the wavelength. The nanowires in this thesis however have dimensions on the order of the wavelength. Fortunately, a nanowire is a highly symmetric structure. If a nanowire is sufficiently long, it can be approximated as an infinitely long cylinder. The scattering problem of a plane wave incident on structures with a high symmetry, such as spheres or cylinders, was solved by Gustav Mie [133].

Mie theory allows us to calculate scattering and absorption efficiencies for a nanowire in a non-absorbing medium, assuming a plane wave of incident light. The analytical equations have been described in detail elsewhere [99]. Mie theory for nanowires assumes an infinite length. This is valid when the angle between the incident light and the long axis of the nanowire is close to 90° and the length of the nanowire is several times ($\gtrsim$5) the wavelength. Only then, the end facets of the nanowire play a limited role. Grzela *et al.* have used time-reversed microscopy (described in Section 3.2) to investigate the relation between Mie theory and waveguide theory. They concluded that Mie theory fails when the incident light is almost parallel to the nanowire. In this case waveguide modes describe the interaction of light with nanowires [80]. The angle-dependent absorption of an array of vertically oriented nanowires is shown in Figure 2.5, along with a calculation based on Mie theory and numerical simulations. More details on this experiment can be found in the caption of Figure 2.5, and in ref. [80]. The deviation from Mie theory occurs when $\theta_i < 30°$. In this case, numerical simulations are needed to accurately calculate the angle-dependent scattering and absorption due to the coupling of the incident light toe waveguide modes.

2.2.2 *Calculation of waveguide mode dispersion*

The propagation of light in a medium is described by the dispersion of the optical modes of the medium. In bulk material, a continuum of modes is available, but when the characteristic sizes of the structure are on the order of the wavelength, there is a limited number of eigenmodes.

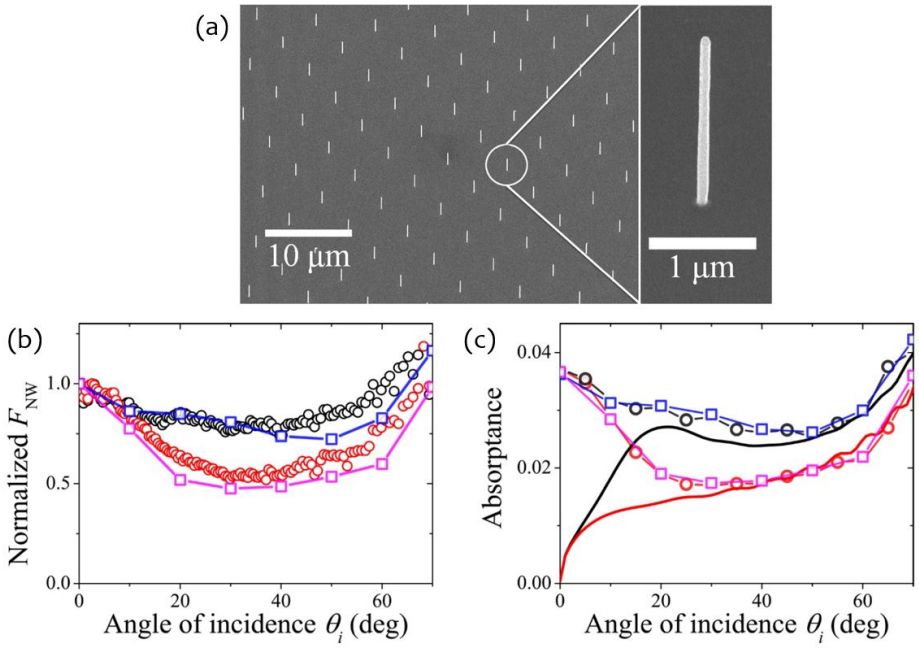

Figure 2.5: Mie theory and waveguide modes on nanowires. (a) Scanning electron microscope image taken at an inclination of 30° of an InP nanowire array grown on top of an InP substrate. The array of nanowires has a pitch of 5 μm. Individual nanowires in this array have a length of 3.1 μm and radius between 45 and 55 nm. (b) Measured normalized directional absorption F_{NW} of nanowires excited with p- and s-polarized light (black and red open circles, respectively) as a function of the angle of incidence. The blue and magenta open squares represent the simulated absorptance of the array of 100 nm-thick nanowires normalized to the value at $\theta_i = 0°$. (c) The blue and magenta squares represent the same absorption as in (b), but plotted in the absolute values of absorptance. The black and red open circles are the simulated angle-dependent absorptance of an array of 90 nm-thick nanowires with a circular cross section for p- and s-polarized illumination, respectively. The solid lines in (c) show the absorptance of the effective medium consisting of 90 nm thick nanowires calculated using transfer matrix formalism. The black line corresponds to the p-polarized absorptance, while the red solid line plots the s-polarized absorptance. Figure reproduced from ref. [80].

Assuming an infinitely long cylinder with radius r, we can calculate the electric and magnetic field components at positions a, both for $a < r$ and $a > r$. At the cylinder boundary, $a = r$, the tangential field components need to be continuous. This requirement defines a homogeneous system of linear equations. The determinant of this system of equations needs to be zero in order to have a solution other than the trivial solution that defines the eigenfrequencies of the modes. The roots of the expansion of the determinant are the eigenfrequencies of the system. For a free-space wavelength λ, $\omega/c = 2\pi/\lambda$, this expansion is as follows [134]:

$$\left(\frac{\mu_c}{k_c r}\frac{J_m'(k_c r)}{J_m(k_c r)} - \frac{\mu_e}{k_e r}\frac{H_m'(k_e r)}{H_m(k_e r)}\right)\left(\frac{\varepsilon_c}{k_c r}\frac{J_m'(k_c r)}{J_m(k_c r)} - \frac{\varepsilon_e}{k_e r}\frac{H_m'(k_e r)}{H_m(k_e r)}\right) = m^2\frac{(k_z r)^2}{(\omega r/c)^2}\left(\frac{1}{(k_e r)^2} - \frac{1}{(k_c r)^2}\right)^2 \tag{2.17}$$

where m is the mode order. J_m and H_m are the standard Bessel and Hankel functions of the first kind, while $k_c = \sqrt{\varepsilon_c(\omega/c)^2 - k_z^2}$ and $k_e = \sqrt{\varepsilon_e(\omega/c)^2 - k_z^2}$ are the transverse components of the mode wave vectors in the cylinder and in the surrounding medium, respectively. Here, k_z is the complex z-component of the wave vector (propagation constant) of any mode that is a solution of the equation above. The dielectric permittivity in cylinder and surrounding medium are denoted as ε_c and ε_e, with $\varepsilon_e = 1$ for vacuum or air. Finally, the magnetic permeabilities in cylinder and environment are μ_c and μ_e, which are both considered equal to 1 since the materials used in this thesis are nonmagnetic. Modes with $k_z < \omega/c$ propagate in the light cone of vacuum and are therefore leaky, while modes with $k_z > \omega/c$ are outside the light cone of vacuum (but inside the light cone defined by the cylinder material) and are guided. Figure 2.6 shows the dispersion relation for the eigenmodes in InP nanowires in vacuum. Only for the leaky modes the wave vector has a nonzero imaginary component, so $k_z = k_z' + ik_z''$. These modes propagate along the nanowire for a limited distance. The typical length scale of propagation is the decay length L_d, which is the distance over which the intensity reduces to a factor $1/e$ of the initial intensity, given by

$$L_d = \frac{1}{2k_z''}. \tag{2.18}$$

The right panel of Figure 2.6 displays the decay lengths of the leaky modes as a function of $k_z'' r$. From this figure we learn that for an InP nanowire with a radius of 50 nm ($k_0 r$=0.38), the imaginary component of the TM_{01} mode $k_z'' r$ equals 0.072, which results in a decay length of L_d/r=7, or L_d=0.35 μm.

The eigenmode field intensity profiles can be calculated using the equations from textbooks, e.g. ref. [135]. As an example, we calculate normalized field profiles of infinite cylinders with radus r=137.5 nm, for the different components in θ-, r-, and z-direction (displayed in Figure 2.7). The first row displays profiles of transverse modes (TE/TM), and the second row hybrid electric modes (HE). In-plane electric field lines for different low-order modes are shown in Figure 2.8.

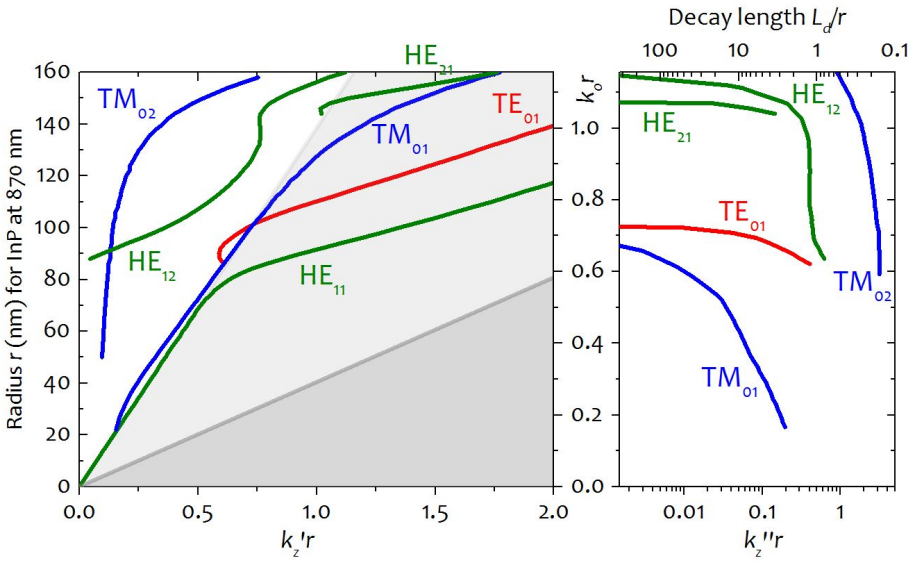

Figure 2.6: Dispersion of the guided and leaky modes in InP nanowires (n=3.43). The left vertical axis indicates the equivalent radius, for an emission wavelength of 870 nm. The dark gray line is the light line in InP, below which no modes can exist (dark gray zone). The light gray line is the light line in air, below which the guided modes exist (light gray zone). The leaky modes are in the light cone of air (white zone). The right panel shows the normalized decay length of the modes.

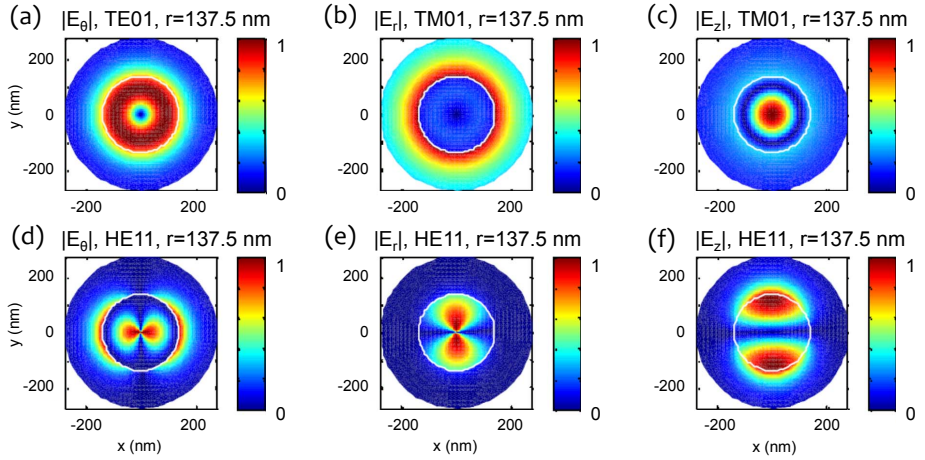

Figure 2.7: Electric field profiles of waveguide modes. The profiles are calculated for infinite cylinders with r=137.5 nm (so diameter d=275 nm), for components in the θ- (a,d), r- (b,e), and z-direction (c,f). The top row (a-c) shows the field components for the TE_{01} and TM_{01} modes, the bottom row (d-f) shows the field components for the HE_{11} mode. Components that are not shown have a zero magnitude.

2.2.3 *1D current emission model based on waveguide modes*

Based on the dispersion relation we can model the directional emission of a nanowire. To this end, a one-dimensional current model developed by Paniagua-Domínguez *et al.* was used [136]. In this model the nanowire emission is determined by a line current $\vec{I}(z)$ produced by a point dipole at position z_0 exciting a leaky or guided mode. For parallel and perpendicular polarization, these displacement currents can be written as $\vec{I} = I(z, z_0)\hat{z}$ (TM_{01} and TE_{01} mode excitation) and $\vec{I} = I(z, z_0)\hat{y}$ (HE_{11} mode excitation), with:

$$I(z, z_0) = I_0 \frac{e^{ik_z z_0} \pm R e^{ik_z L} e^{-ik_z z_0}}{1 - R^2 e^{2ik_z L}} \left(R e^{ik_z L} e^{ik_z z} - e^{-ik_z z} \right), \quad \text{for } -L/2 \leq z < z_0; \quad (2.19a)$$

$$I(z, z_0) = I_0 \frac{R e^{ik_z L} e^{ik_z z_0} \pm e^{-ik_z z_0}}{1 - R^2 e^{2ik_z L}} \left(e^{ik_z z} - R e^{ik_z L} e^{-ik_z z} \right), \quad \text{for } z_0 < z \leq L/2, \quad (2.19b)$$

where the $\pm$ sign depends on the dipole character (electric or magnetic) and the specific mode being excited; k_z corresponds to the mode wave number, and R is the mode reflection coefficient at the nanowire end facets. Note that the equations are here applied to first-order modes,

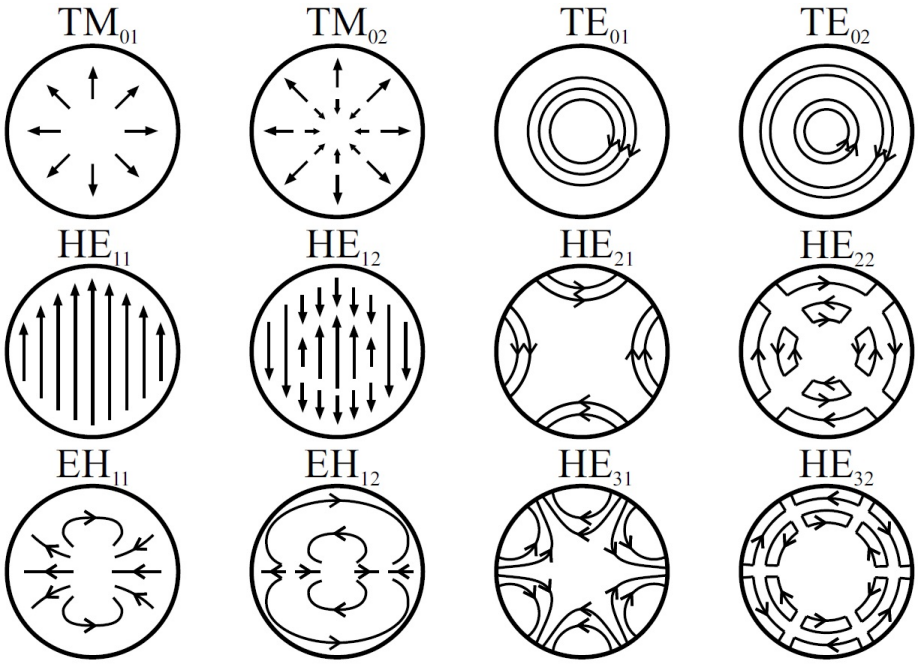

Figure 2.8: In-plane electric field lines of the first guided modes inside a cylinder. The cross-section of the cylinder is shown by the solid circles. Copied from ref. [104].

but they also work for higher order modes. As shown in ref. [136], the resulting electric far field components are:

$$E_\theta = \frac{ik_0\eta_0}{4\pi}\sin\theta\int_{-L/2}^{L/2} I(z,z_0)e^{-ik_0 z\cos\theta}dz, \tag{2.20a}$$

$$E_\phi = 0, \tag{2.20b}$$

for the TM_{01} mode, and:

$$E_\theta = \frac{ik\eta_0}{4\pi}\cos\theta\sin\phi\int_{-L/2}^{L/2} I(z,z_0)e^{-ik_0 z\cos\theta}dz, \tag{2.21a}$$

$$E_\phi = \frac{ik\eta_0}{4\pi}\cos\phi\int_{-L/2}^{L/2} I(z,z_0)e^{-ik_0 z\cos\theta}dz, \tag{2.21b}$$

for the HE_{11} mode. Here η_0 stands for the vacuum impedance. In the case of the TE_{01} mode, we made use of the symmetry between $\vec{E}, \vec{H}$ in Maxwell's equations, so that the far field is exactly that of the TM_{01} mode, but with opposite polarization (equivalent to consider that Eqs. 2.21 for the TM_{01} mode yield the magnetic far field components instead). From the field components, the angular distribution of the emission is given by the time-averaged Poynting

vector $\langle \vec{S} \rangle = \frac{\varepsilon_e c}{2} |\vec{E}|^2$, where c is the speed of light in vacuum and ε_e the vacuum permittivity. From this we calculate the far field emission intensity as a function of the dipole position in the nanowire. As an example, we have calculated the normalized angular emission for InP nanowires with three different radii in Figure 2.9. The calculations used 30 dipoles distributed evenly over the nanowire length. We observe a strong dependence of the emission pattern on the radius, as further discussed in Chapter 7.

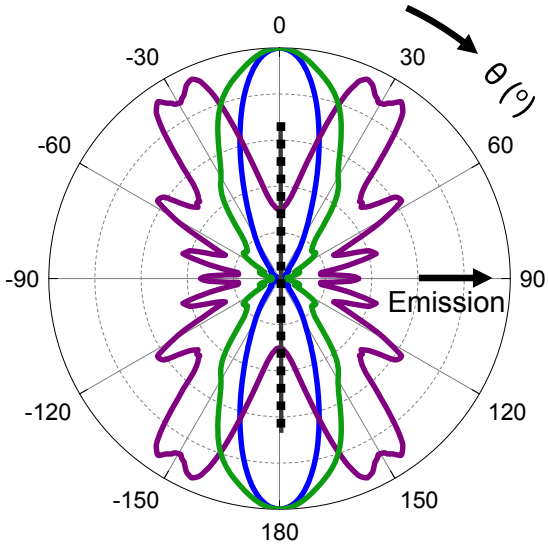

Figure 2.9: Angular patterns of the emission of one-dimensional currents in InP nanowires. The gray line with black dots in the center symbolizes the orientation of the nanowire with the homogeneous distribution of dipoles along the length. The nanowires have radii of 77.5 nm (blue), 84.5 nm (green) and 104 nm (purple). In the first two cases only the HE_{11} mode was taken into account, for the largest radius it is the average between the HE_{11} and TE_{01} modes. The data is normalized to the maximum and averaged over the two polarizations.

3

EXPERIMENTAL METHODS

This chapter describes the experimental methods that were used to obtain the results described in this thesis. They consist of Fourier microscopy and Time-reversed Fourier Microscopy. The methods are introduced and polarization effects are discussed. Finally, the intensity calibration of the photoluminescence (PL) collection is addressed.

3.1 FOURIER MICROSCOPY

Fourier microscopy allows to measure directional emission. The technique is also called 'back focal plane imaging', which is selfexplanatory: the back focal plane of a microscope objective is imaged using a CCD camera. In this way, a circular image is obtained, directly showing the wave vectors of the scattered or emitted light. Each point in the back focal plane corresponds to wave vector of the emission. For instance, emission in the normal direction, perpendicular to the substrate, ends up in the center of the back focal plane, whereas emission at large angles with respect to the nanowire's axis, entering the objective at the very edge of the numerical aperture (NA), can be observed at the edge of the back focal plane. The objective's NA (in our setup NA=0.95) determines the maximum collection angle of the emission at $\theta_{max} = \sin^{-1}(0.95) = 72°$. In such way, all the directional information of the emission captured within the solid angle of the objective is preserved in a so-called Fourier image. Typically, a narrow band pass filter is used in front of the CCD camera to image the emission at a fixed wavelength. The setup is depicted in Figure 3.1.

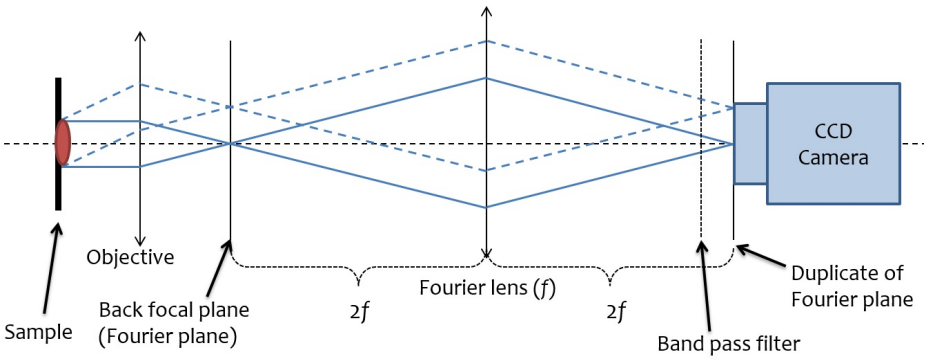

Figure 3.1: Fourier microscope set-up. Solid and dashed lines indicate light rays.

3.1.1 *Polarization analysis*

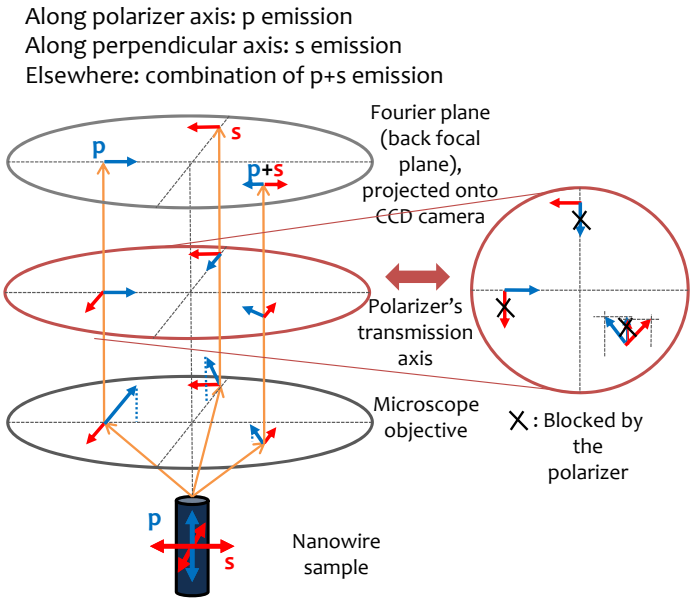

Figure 3.2: Polarization analysis of the emission in the back focal plane of the objective. P-polarization is defined parallel to the long axis of the nanowire and the wave vector k, s-polaration as perpendicular to these. P-polarized emission is collected along the diameter of the back focal plane parallel to the transmission axis of the polarizer, while s-polarized emission is collected along the orthogonal diameter. Therefore, acquiring a single polarized Fourier image gives both p- and s-polarized emission.

Apart from the direction, the polarization is an important property of light. In the case of vertical nanowires, we distinguish between p-polarized light (polarization vector in the plane of the wave vector k and the nanowire axis) and s-polarized light (perpendicular to the plane of k and the nanowire axis). To probe the different polarizations of the emission, a polarizer is placed in the collection path. The acquired emission along the transmission axis of the polarizer is purely p-polarized, whereas the emission along the axis perpendicular to the polarizer's axis is purely s-polarized. The polarization of the emission off these axes is a combination of p- and s-polarization. The unpolarized emission pattern is derived by adding the emission patterns acquired by the two orthogonal orientations of the polarizer, taking into account the polarization-dependent response of the set-up. The set-up is schematically depicted in Fig-

ure 3.1, while the propagation of s- and p-polarized light is shown in Figure 3.2. Definitions of parallel, perpendicular, s, and p are depicted in Figure 3.3.

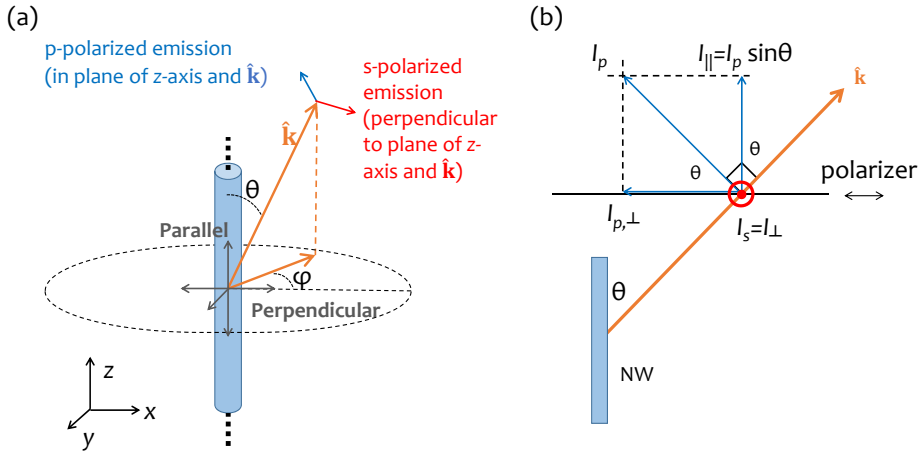

Figure 3.3: (a) Definitions of s, p, parallel, perpendicular and coordinate system. (b) Graphical explanation in the nanowire-axis-k plane of the relations between $I_{\|}$, $I_{\perp}$ and I_p, I_s.

3.2 TIME-REVERSED FOURIER MICROSCOPY

Time-reversed Fourier microscopy (TRFM) has been used to measure the angle-dependent absorption of metal nanoparticle arrays [137] and semiconductor nanowires [80]. It is based on the reciprocal equivalence of Fourier microscopy: instead of imaging the back focal plane, we focus a laser to a quasi-point source in the back focal plane. As each position in the back focal plane corresponds to a certain k-vector under the objective, we can excite a nanostructure with a plane wave under an objective. When changing the position of the laser, the incident k changes. In order to realize TRFM measurements, we mounted a laser including focusing lens on a computer-controlled two-dimensional rotation stage, which allows us to scan over all k-vectors that are available within the numerical aperture of the objective. A schematic of the TRFM setup is shown in Figure 3.4. The excitation beam on the sample under the microscope objective in this setup is a plane wave limited to the field of view of the objective, i.e. $\sim$ 100 μm in diameter, which enables us to do angle-dependent measurements on small samples. The signal that can be detected can be photoluminescence (PL) or reflection. Also, the setup is equipped with remote-controlled microprobes [138], which allows us to measure angle-dependent photocurrent. The setup, including its principles and alignment, has been described in detail by Grzegorz Grzela in his PhD thesis [104].

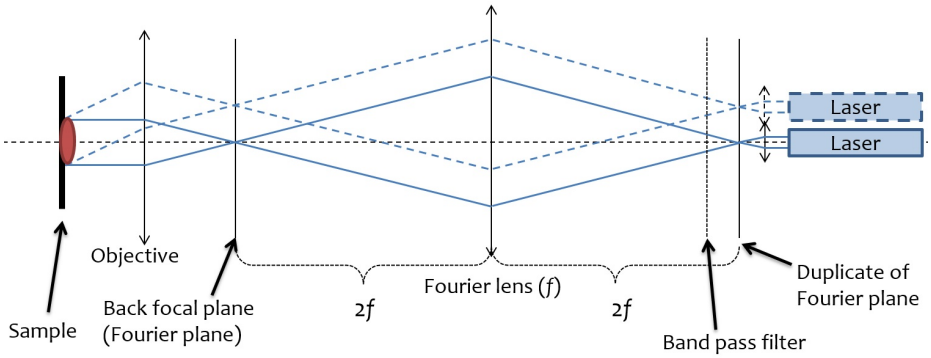

Figure 3.4: Time-reversed Fourier microscope set-up. Solid and dashed lines indicate light rays, for two different laser positions.

The result of the optical configuration of the TRFM setup is that the incident intensity drops when the angle of incidence increases, which is caused be increased reflections at the lenses and components that block a part of the expaned beam. Therefore, the intensity needs to be carefully calibrated. For the PL measurements we use a planar layer for calibration, as has been described elsewhere [104]. For calibrating the current-voltage measurement of our small solar cell, we need to take into account that the photocurrent collection takes place over the entire excitation spot area, while the PL collection is limited to a small part of the spot defined by the excitation beam. Therefore, we need to perform the calibration measurement using a planar, large area silicon solar cell, which we measure in the TRFM setup as a function of the angle (two-dimensional scan). We also perform an angle-dependent reference measurement on a rotation stage, using the same solar cell. This setup and its results are shown in Figure 3.5. The real photocurrent of a small solar cell, which can be a nanowire solar cell (NWSC), $I_{\text{real}}^{\text{NWSC}}$, can be extracted from the measured photocurrent using a correction function $C(\theta,\phi)$:

$$I_{\text{real}}^{\text{NWSC}}(\theta,\phi) = I_{\text{TRFM}}^{\text{NWSC}}(\theta,\phi)C(\theta,\phi) = I_{\text{TRFM}}^{\text{NWSC}}(\theta,\phi)\frac{I_{\text{rot.stage}}^{\text{Si ref}}(\theta,\phi)}{I_{\text{TRFM}}^{\text{Si ref}}(\theta,\phi)}. \tag{3.1}$$

3.3 CALIBRATED PHOTOLUMINESCENCE INTENSITY MEASUREMENTS

The absolute photoluminescence intensity of a semiconductor sample is proportional to the splitting of the highest populated valence band level and the lowest populated conduction band level, i.e. the splitting of the quasi-Fermi-levels μ [51, 139]. Therefore, performing calibrated PL measurements allows for determining this splitting, which is equivalent to the maximum value of a solar cell's V_{OC}, by $\mu = qV_{\text{OC}}$. Such measurements have been performed in, among others, refs. [140, 141]. There are several reasons which make the combination of this

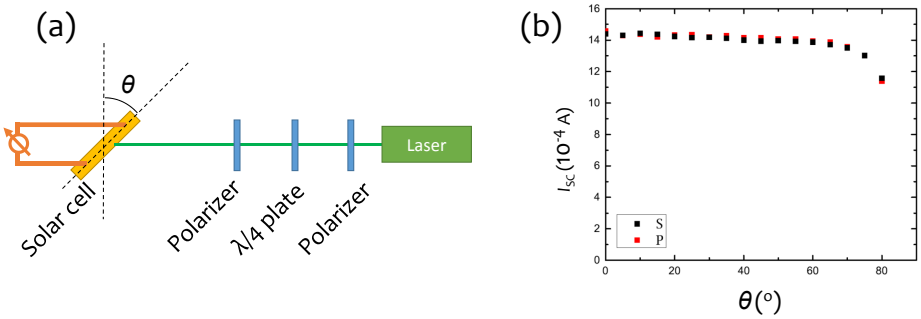

Figure 3.5: Angle-dependent reference measurement of silicon solar cell in a rotation stage. (a) Schematic representation of the setup. (b) Photocurrent I as a function of the incident angle θ, as measured in the rotation stage depicted in (a).

method and a TRFM appealing. The first one is the possiblity to use plane wave illumination on micro-sized samples and select the emission from a micro-sized area. The second reason is the use of a high-NA microscope objective, which captures the emission up to a large angle. A third reason is the easy access to angle-dependent emission measurements, which is needed to estimate how much of the emission is captured within the objective. Therefore, we have calibrated the TRFM setup. The measurements are done using excitation at normal incidence. A complete schematic overview of the setup is shown in Figure 3.6.

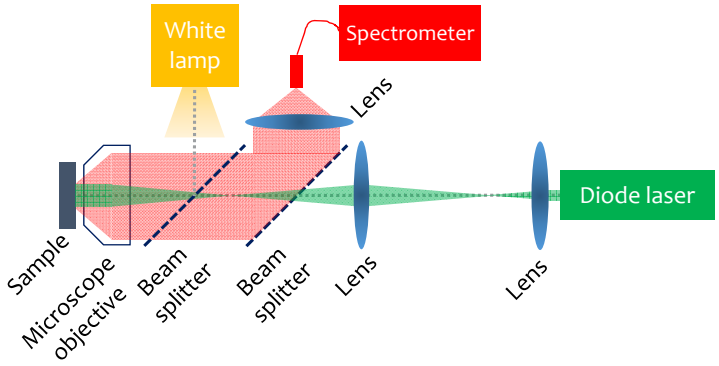

Figure 3.6: Schematic overview of the configuration of the TRFM as used for the calibrated PL measurements

3.3.1 *Collection efficiency of photoluminescence*

First, we need to measure the number of incident photons at the position of our sample, by using a silicon photodiode. Then, we measure the collection efficiency at the wavelength of the PL, λ_{em}. To do so, we turn off the laser and use a white lamp which is equipped with a narrow (10 nm full-width at half maximum) band pass filter. The intensity of the lamp is kept constant and its power $P_{lamp}(\lambda_{em})$ is measured at the sample position, using the silicon photodiode. This power corresponds to a photon rate equal to $\gamma_{source} = P_{lamp}/E_{photon}$, where $E_{photon} = hc/\lambda_{em}$ is the photon energy. Then, the photodiode is replaced by a silver mirror (reflection $R_{mirror}(\lambda_{em})$). This configuration represents a light source of known intensity in the sample position. We measure the PL spectrum using a fiber-coupled spectrometer. The integrated spectrum represents the detected rate of photons $\gamma_{detected}$ per second. From these measurements we can extract the PL collection efficiency of the setup, at the emission wavelength λ_{em}, expressed as

$$\eta_{setup}(\lambda_{em}) = \frac{\gamma_{detected}(\lambda_{em})}{\gamma_{source}(\lambda_{em})R_{mirror}(\lambda_{em})} = \frac{\gamma_{detected}(\lambda_{em})}{P_{lamp}(\lambda_{em})R_{mirror}(\lambda_{em})\lambda_{em}/(hc)}. \tag{3.2}$$

A fraction of the emission is lost since it cannot be captured by the objective. Considering the objective in our setup, which has a numerical aperture of 0.95 and can therefore detect up to a maximum angle of $\sin^{-1} 0.95 = 72°$, the fraction that is captured is

$$\frac{2\pi \int_0^{\sin^{-1}0.95} \cos\theta \sin\theta \mathrm{d}\theta}{2\pi \int_0^{\pi/2} \cos\theta \sin\theta \mathrm{d}\theta} \approx 0.90, \tag{3.3}$$

assuming a Lambertian emission. We should note that the assumption of Lambertian emission is not always true for a nanostructured sample (see e.g. Chapter 6).

3.3.2 *Power-dependent photoluminescence measurements*

To relate the incident total intensity to a power density, we image the cross-section of the beam using an imaging CCD camera. The incident wave is measured at the sample plane to have a radius of $55 \pm 5\ \mu$m. The spectrometer collects the light coming from a circular area on the sample with a radius of $26 \pm 2\ \mu$m, which is collinear with the excitation beam. We measure that 43% of the PL occurs within the field of view of the spectrometer.

The actual emitted intensity of the PL per unit area can be expressed at follows:

$$I_{PL,real}\ [\mathrm{cts/s/cm^2}] = \frac{I_{PL,meas}}{A_{PL}\eta_{setup}}, \tag{3.4}$$

where $I_{\text{PL,meas}}$ is the measured PL integrated in the spectrometer, A_{PL} is the area of the PL collection, in this case 43% of the excitation spot area A_{exc}. The corresponding excitation intensity I_{in} per unit area is expressed as

$$I_{\text{in}}\ [\text{cts/s/cm}^2] = \frac{P_{\text{in}} hc}{A_{\text{exc}} \lambda_{\text{exc}}}, \tag{3.5}$$

where P_{in} is the incident power, measured at the sample position. hc/λ_{exc} is the energy of a photon from the excitation laser. To apply these measurements to solar cells, it is convenient to determine the V_{OC} at an incident intensity of 1 sun. Therefore, I_{in} can be related to the number of suns, which is defined by the number of photons beyond the band gap energy E_g of the material per unit area, $\phi(E_g)$:

$$I_{\text{in}}\ [\text{suns}] = \frac{I_{\text{in}}\ [\text{cts/s/cm}^2]}{\phi(E_g)}. \tag{3.6}$$

The number of photons beyond the band gap energy $\phi(E_g)$ is shown in Figure 3.7. From the calibrated PL measurements we can determine the quasi-Fermi energy level splitting, as is described in Chapter 4.

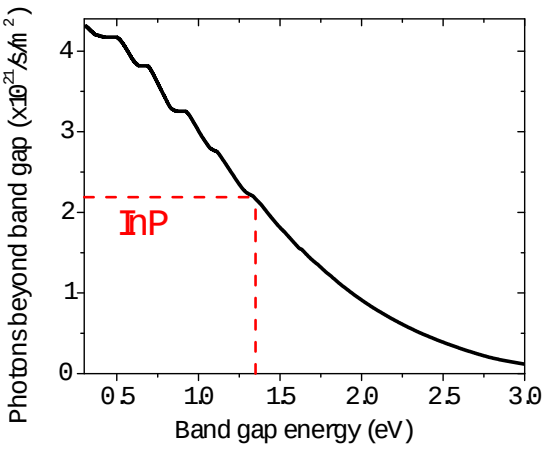

Figure 3.7: Flux of photons in the AM1.5G solar spectrum beyond the band gap, as a function of the band gap energy. The dashed line indicates the material InP, for which 2.19×10^{21} photons from the solar spectrum are beyond the band gap energy, each second per square meter.

4

ENHANCED VOLTAGE IN NANOWIRE SOLAR CELLS

We demonstrate experimentally that nanostructured solar cells can fundamentally outperform their planar counterparts not only in photocurrent, but also in open circuit voltage. By etching tapered nanowires from planar InP, a direct comparison can be made between planar and nanophotonic geometries without affecting material quality. We show that the external radiative efficiency at 1 sun is increased by a factor 14 compared to the planar geometry, leading to a 70 mV enhancement in open circuit voltage. The higher photovoltage arises from both the lower active material volume, which lowers bulk recombination, and the enhanced outcoupling of photons, which promotes radiative recombination. Based on these insights, we have fabricated an InP nanowire solar cell with a power conversion efficiency of 17.8% (calculated based on the exposed area), a large increase over the previous record nanowire device. These effects are generic and promise to further enhance efficiencies of already high-performance solar cells.

4.1 INTRODUCTION

To maximize the conversion efficiency of sunlight into electricity, a photovoltaic device needs to simultaneously achieve optimal photocurrent and voltage. Nanophotonic engineering has been employed to enhance the photocurrent of solar cells by reducing reflection and increasing solar light absorption via light trapping, and values close to maximum absorption have already been achieved [26, 27, 37, 40, 44, 142, 143]. Therefore, in order to bring the photovoltaic conversion efficiency closer to the theoretical limit as determined by Shockley and Queisser [17], the open circuit voltage (V_{OC}) needs to be further improved [55, 81, 144, 145]. The V_{OC} is generally expressed as a function of photocurrent density J_{SC} and dark current density J_0 as $V_{OC} \approx \frac{k_B T}{q} \ln \frac{J_{SC}}{J_0}$, in which k_B, T and q are the Boltzmann constant, solar cell temperature, and electron charge, respectively [51]. The dark (saturation) current density is proportional to the recombination rate, and can be separated into a radiative part and a non-radiative part. Maximizing the voltage requires minimizing recombination, but even a perfect solar cell must undergo radiative recombination to remain in thermal equilibrium with its surroundings. On the other hand, non-radiative recombination caused by bulk defect and surface recombination, constitutes a loss that can be eliminated. Therefore, improving the V_{OC} requires increasing the ratio of external radiative to total recombination rates, which is equivalent to increasing the external radiative efficiency (η_{ext}). The η_{ext} depends mainly on two parameters: the internal radiative efficiency (η_{int}), which gives the fraction of internal recombination events that

is radiative, and the escape probability ($\overline{P_{esc}}$), which gives the fraction of emitted photons that escape the cell. Bulk non-radiative recombination in a solar cell is proportional to the amount of active material, which means that η_{int} can be improved by reducing the amount of material if surface recombination plays a minor role. Additionally, efficient outcoupling of internally emitted photons is essential, because it prevents eventual non-radiative recombination due to photon reabsorption [47]. Therefore, reducing the amount of absorber material and enhancing $\overline{P_{esc}}$ of emitted photons improves the V_{OC}. This becomes directly apparent from the equation for the V_{OC} [132]:

$$V_{OC} = V_{OC}^{rad} - \frac{k_B T}{q}\left|\ln\frac{\eta_{int}\overline{P_{esc}}}{1-\eta_{int}(1-\overline{P_{esc}})}\right| \tag{4.1}$$

where V_{OC}^{rad} is the V_{OC} in the radiative limit (absence of non-radiative recombination). If $\eta_{int} \lesssim 0.1$ this equation can be simplified to

$$V_{OC} = V_{OC}^{rad} - \frac{k_B T}{q}|\ln(\eta_{int}\overline{P_{esc}})|. \tag{4.2}$$

The effects of $\overline{P_{esc}}$ and η_{int} on the V_{OC} are displayed in Figure 4.1a. This figure shows that im-

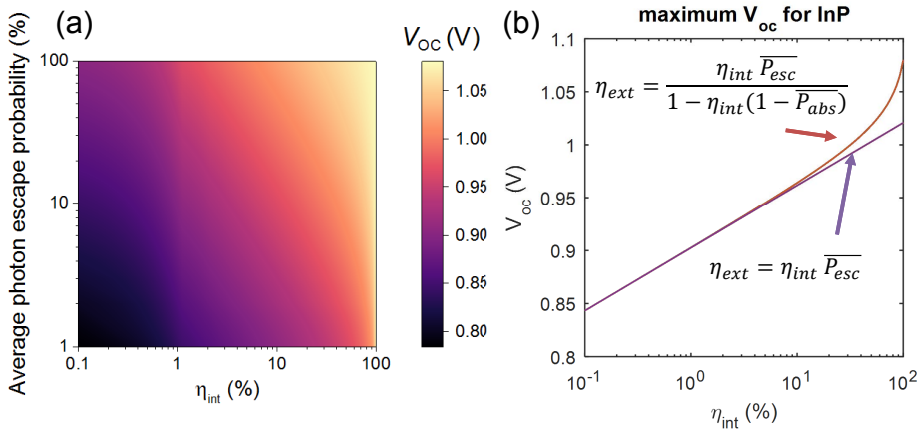

Figure 4.1: Voc as a function of the internal radiative efficiency and photon escape probability. The calculation was performed for the AM1.5 spectrum and a band gap of 1.34 eV (e.g. InP). (a) shows a plot dependent on both η_{int} and $\overline{P_{esc}}$. For (b) $\overline{P_{esc}}$ is fixed to 10% and the difference between the actual equation (Equation 4.1, red), and the simplified version (Equation 4.2, purple), which is valid when $\eta_{int} \lesssim 0.1$.

provements in η_{int} and $\overline{P_{esc}}$ are equally important for increasing the V_{OC}. A reduction of the material volume while simultaneously maintaining maximum absorption of sunlight can be achieved using the antenna effect of nanostructures, which allows them to absorb light from a larger area than their projected geometrical area [21, 81, 142]. For minimizing losses due to the

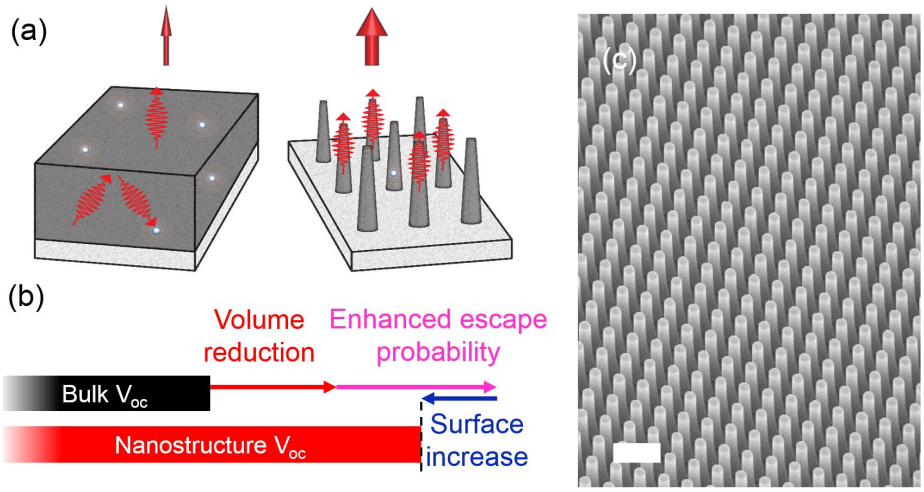

Figure 4.2: Effect of nanowire geometry on V_{OC}. a) A planar InP sample is compared with a piece of the same material in which a nanowire structure is defined by etching: the emission outcoupling enhanced and the number of bulk defect is reduced. b) Schematic of the effects of the nanostructuring on the V_{OC}. Because of reduced bulk recombination and enhanced outcoupling, the emission intensity (red upward arrow) is enhanced, indicating a higher V_{OC}. c) Scanning Electron Micrograph of the etched nanowire array, imaged at a 30° tilt. The scale bar represents 1 micron.

$\overline{P_{esc}}$ term, enhanced outcoupling of internally generated photons can be achieved in tapered nanowires by utilizing adiabatic expansion of the optical mode confined in the nanowire into free space [119]. The two described mechanisms, applied to tapered nanowires, are schematically displayed in Figure 4.2a. Figure 4.2b shows the effects on the V_{OC}, including a possible reduction due to the increased surface area. A high V_{OC} in a nanostructured solar cell has been reported recently [85], but its origin was not identified. Here we demonstrate that nanostructuring enhances the V_{OC} due to the two mechanisms described above and use these insights to reach record nanowire solar cell conversion efficiency.

4.2 DIRECT MATERIAL COMPARISON

To investigate the effect of nanostructuring on the V_{OC}, we compare planar indium phosphide (InP) material with a piece from the same sample, in which we have defined nanostructures by top-down lithographic techniques. The planar and nanostructured samples thus consist of identical material, which allows us to isolate the effect of nanostructuring on the V_{OC}. We use an intrinsic epitaxial InP layer of 1600 nm grown by metal-organic vapour-phase epitaxy (MOVPE), on top of an InP wafer. We chose InP because it has a direct band gap E_g with the

ideal energy for photovoltaic devices (E_g=1.34 eV), and a low surface recombination velocity [146]. The nanostructured sample (a periodic array of conically shaped nanowires) is fabricated by selectively dry etching the thin film through a chromium mask patterned by nanoimprint lithography, followed by digital etching to remove surface defects. The result is shown in a scanning electron micrograph in Figure 4.2c. The period of our square array is 513 nm, where the 1.6 μm long tapered wires have a base diameter of 350 nm and a top diameter of 150 nm. The conical shape is chosen because of its very high absorptance [21, 40, 43, 147], which for InP can be over 98% in the wavelength range between 400 and 900 nm [21].

4.3 VOLTAGE MEASUREMENTS

To compare the V_{OC} with and without nanostructuring, we use the fact that the photoluminescence (PL) emission intensity I_{PL} in a semiconductor is directly related to the splitting of its quasi-Fermi levels [126, 139, 148]. This relation is expressed through the following equation:

$$I_{PL}(E) = a(E) I_{bb}(E)(\exp(\mu/k_B T - 1), \tag{4.3}$$

where E is the energy of the emission, $a(E)$ is the absorptance, and $I_{bb}(E)$ is the blackbody emission intensity, $I_{bb}(E) = \frac{2\pi E^2 A}{h^3 c^2} \exp(-E/k_B T)$. Here A denotes the area of the emitting region, h Planck's constant and c the speed of light. Using this equation one can find the Fermi-level splitting:

$$\mu = E + k_B T \ln \frac{I_{PL} h^3 c^2}{2\pi E^2 a(E) A}. \tag{4.4}$$

μ defines the maximum value of the V_{OC} by $V_{OC,max} = \mu/q$, where q is the electron charge. A similar analysis has recently been performed by Tran et al. [141].

In this way we can use calibrated PL measurements as a contactless probe for the V_{OC}. PL emission spectra of InP with and without nanostructuring are shown in Figure 4.3a (absolute counts) and Figure 4.3b (normalized counts), measured at room temperature. The normalized emission spectra are identical and only show band gap related emission, the nanowire layer shows a 20-fold higher emission intensity. This increased emission cannot be explained by the increase in absorptance alone, which is only a factor of 1.4 (as will be calculated in Chapter 5).

Power dependent PL emission intensities are shown in Figure 4.3c. The number of suns corresponding to the incident photon intensity is plotted on the top horizontal axis. From the absorbed and emitted photon intensities at 1 sun, we calculate $\eta_{ext} = (7.0 \pm 0.9) * 10^{-4}$ for the nanowire array and $(5.2 \pm 0.5) * 10^{-5}$ for the planar sample. These calculations assume that all the PL is collected by the setup, which is not the case. However, in this case, the angular distribution of both planar and nanostructured sample are identical, therefore the η_{ext} values can be directly compared. The quasi-Fermi level splitting (equivalent to maximum achievable V_{OC} in a contacted device) obtained from the integrated PL intensity is displayed on the right axis (as calculated above). It is clear that nanostructuring increases the Fermi level splitting

compared to the planar film for the entire excitation intensity range from 1 to 1000 suns. At 1 sun the implied V_{OC} is 70 mV higher for the nanostructured sample compared to the planar sample, demonstrating that a nanostructured solar cell allows an intrinsic advantage in photovoltage over a planar layer, even without employing surface passivation.

4.4 EFFECTS ON V_{OC} THROUGH NANOSTUCTURING

The different contributions to the V_{OC} will be discussed now in more detail.

4.4.1 *Material volume reduction*

The first contribution is the reduction of material volume by a factor of 5.1, which therefore also reduces the non-radiative bulk recombination rate by the same factor. If the total non-radiative recombination is dominated by bulk recombination, this would result in an increase in V_{OC} equal to $\frac{k_B T}{q} \ln(5.1) = 42$ mV. We emphasize that due to the optical antenna effect of the nanowires, the reduction in material volume does not decrease the short circuit current, as we will also discuss later.

4.4.2 *Enhanced emission outcoupling*

The second contribution to the improved V_{OC} is enhanced light outcoupling. The photon escape probability of a radiative recombination event inside the nanowire array was estimated with FDTD simulations. To incorporate the effect of the array we simulated 7 by 7 unit cells, with the dipole source located in the center wire. The escape probability at a certain point x is then estimated as:

$$\overline{P_{esc}}(x) = \frac{\int_0^\infty P_{up}(E, x) S(E) \mathrm{d}E}{\int_0^\infty P_{tot}(E, x) S(E) \mathrm{d}E}. \tag{4.5}$$

Here $P_{up}(E, x)$ is the fraction of radiated power into the upper hemisphere (free space), averaged over all dipole orientations, $P_{tot}(E, x)$ is the total radiated power by the dipoles, which may vary with position due to the modified local density of optical states. Due to the lossy nature of the material we have to measure total power output with a small transmission box around the dipole.

$S(E)$ is the van Roosbroeck-Shockley relation for emission flux from a semiconductor volume, defined as [126]

$$S(E) = \frac{2\alpha(E) n^2 E^2}{h^3 c^2} \frac{1}{\exp(E/k_B T) - 1}, \tag{4.6}$$

where $\alpha(E)$ is the absorption coefficient, n is the real part of the refractive index, h is Planck's constant, c is the speed of light, E is the photon energy, and T is the temperature (300 K).

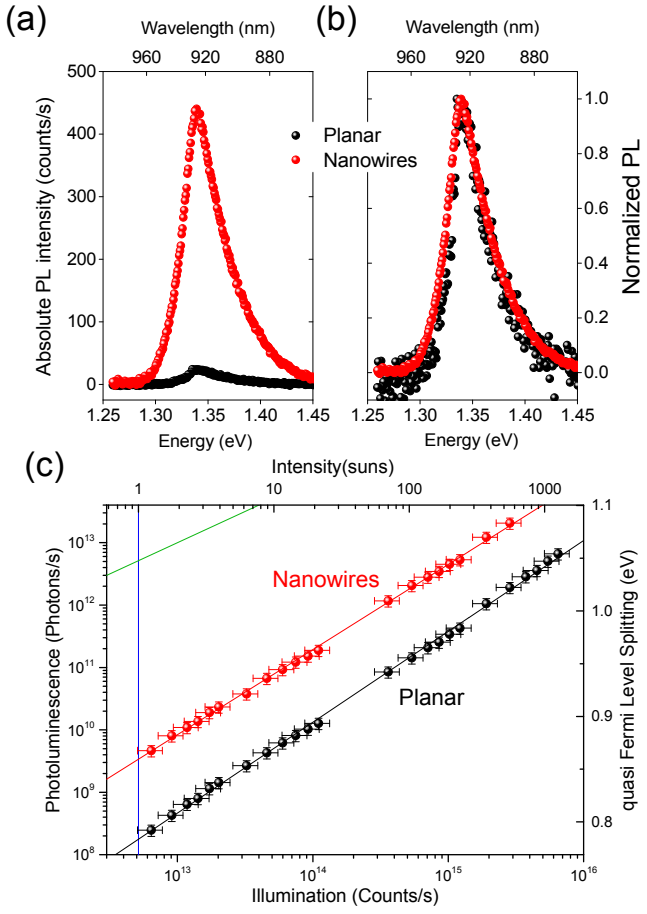

Figure 4.3: Determination of quasi-Fermi level splitting by photoluminescence. Photoluminescence spectra of a) planar layer (black) and nanowire layer (red). b) same as a), but normalized to their respective maxima, to allow comparison of the shapes. c) Power-dependent PL for planar (black) and nanostructured (red) InP films, corrected for absorption at the PL wavelength. The illumination intensity is converted into suns (top axis) and the PL intensity is expressed as Fermi level splitting (right axis). The blue line corresponds to 1 sun and the green line is the ideal curve for a sample with external radiative efficiency equal to 1.

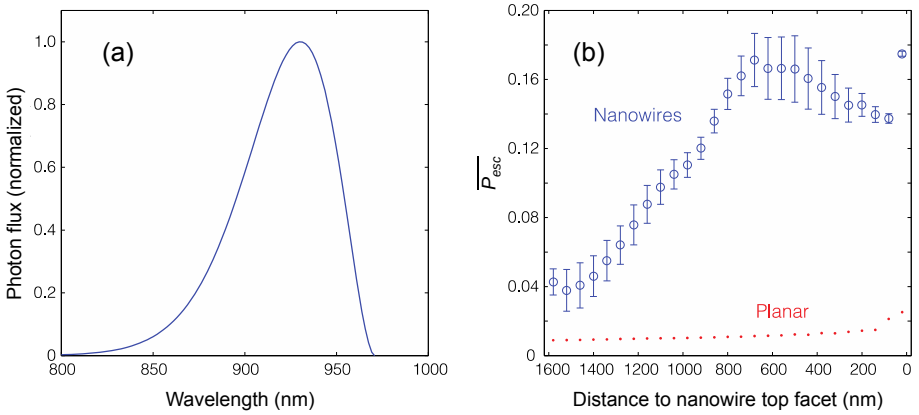

Figure 4.4: Simulated photon escape probability for a nanowire layer. (a) photon flux as used in the simulation, here plotted as a function of wavelength. (b) Average photon escape probability as a function of emitter height, for both nanowire and planar layer.

For the refractive index in this expression (α and n) we have used the data of Palik [149]. The corresponding photon emission flux $S(E)$ is shown in Figure 4.4a. Figure 4.4b shows the escape probability as a function of height in the nanowire, where we have averaged over multiple positions in the plane perpendicular to the nanowire axis, calculated on a grid with pixel size of 40 by 40 nm. The error bars display the fraction of power that escapes through the sides of the simulation volume, and as a result it is not clear whether it eventually escapes, is reabsorbed in the active layer, or in the substrate. The escape probability is as high as 16%, but varies with position of the emitter, as one would expect. Determining the actual escape probability thus depends on the generation profile and carrier diffusion. As an approximation, we use the average escape probability of dipoles located within the $1/e^2$ absorption depth of the excitation at 532 nm. With this assumption, we find that $\overline{P_{esc}}$ for the nanowires is 13% and for the planar film is 2.1%. The average escape probability from the planar layer can also be estimated from the escape cone for light of wavelength λ in a slab of refractive index $n(\lambda)$. The average escape probability can be calculated as the ratio of the solid angle of the escape cone Ω_{out} and the total spherical solid angle $\Omega_{sphere} = 4\pi$. We thus find

$$\overline{P_{esc}} = \frac{\Omega_{out}}{\Omega_{sphere}} = \frac{2\pi(1-\cos\theta)}{4\pi} = \frac{1}{2}(1-\cos\theta) = \frac{1}{2} - \frac{1}{2}\sqrt{1-1/n(\lambda)^2}, \tag{4.7}$$

where θ is the critical emission angle, defined as $\sin\theta = 1/n(\lambda)$ according to Snell's law [150]. For InP at 925 nm this gives a $\overline{P_{esc}}$ for planar material which is also equal to 2.1%, indicating that photon reabsorption does not play a significant role, unless the diffusion length is very large. The enhancement in $\overline{P_{esc}}$ can be quantified as a factor 6.3, which corresponds to an increase in V_{OC} of 47 mV.

4.4.3 *Other effects*

Since these effects together would result in a larger increase of V_{OC} (89 mV) than we have observed, we argue that increased surface recombination due to the increased surface area for the nanowires sample partially compensates the gain in V_{OC}. These results show, however, that even without surface passivation, the net V_{OC} is enhanced by nanostructuring. We emphasize that this effect is not a 'concentration' effect, since light concentration changes the photon entropy between light absorption and light emission, and thus modifies the thermodynamic limit given by V_{OC}^{rad}. Such a thermodynamic enhancement is possible in principle using nanowire arrays, but requires a specifically engineered angular emission profile [58], which is outside the scope of the present chapter.

4.5 SOLAR CELL DEVICES

To further demonstrate the potential of nanowire solar cells, we have fabricated solar cell devices, as depicted in a cross-sectional SEM image (Figure 4.5a) with a schematic of a cross-cut of the cell (Figure 4.5b). A microscope image of the device is shown in Figure 4.5c. The fabrication of nanowire solar cell starts with the growth of the active layers of the solar cell. The active layers are grown in an MOVPE reactor on a Zn-doped InP (100) substrate at a temperature of 650 °C. A 200 nm thickness p+ InP layer was firstly grown on the top surface of the substrate. This p+ InP layer serves as a back-surface field to facilitate hole transfer into the p-type InP substrate, while simultaneously blocking electron transfer into the substrate. Then a 1400 nm thick lightly p-doped (10^{17}/cm^3) InP base layer is grown as a light-absorbing layer. In order to obtain a high electrical conductivity, the doping level of this layer is made slightly higher than that for a GaAs thin film solar cell, since nanowire arrays have a larger resistance than a planar film. Subsequently, a 170 nm n+ InP emitter layer and a 30 nm n++ InP contact layer are grown, which will also serve as a front surface field for blocking hole transfer to the ITO layer. To create the nanowire solar cell, the doped layers are etched in the same way as the intrinsic nanowires in the previous sections. Afterwards, the doped nanowires are processed using the procedure described in ref. [87].

The current density-voltage ($J-V$) curve of our highest efficiency nanowire solar cell under 1 sun illumination (AM 1.5) was independently measured and certified at the PV testing facility at the National Renewable Energy Laboratories (NREL, USA). The certified parameters are a V_{OC} of 0.765 V, a fill factor (FF) of 0.794, and a J_{SC} of 10.1 mA/cm^2, based on the total cell area including gold bus bar (red square in Figure 4.5c). If we calculate the photocurrent based on the exposed area of the cell that absorbs light (green square in Figure 4.5c), we get J_{SC} =29.3 mA/cm^2, which leads to a power conversion efficiency of 17.8%. This $J-V$ curve is shown in Figure 4.5d. We have also measured the external quantum efficiency (EQE), which is the number

of collected electrons for each impinging photon at a given wavelength. The EQE is shown as a function of the wavelength in Figure 4.5e demonstrates high efficiency for all wavelengths below the optical band gap of InP. The J_{SC} is among the highest ever reported for III-V solar cells [14], while the 17.8% power conversion efficiency is the highest achieved for nanowire solar cells so far. The present efficiency can be further improved by optimizing the ITO deposition to eliminate surface damage on the nanowires. Furthermore, we have not made any efforts to passivate the surface, which we expect can lead to even higher efficiencies. Since a large part ($16/25^{\text{th}}$) of our cell is covered by the gold bus bar, the dark current is relatively large. If we would limit the cells to the active part, e.g. by a more advanced device design, like thin metal stripes instead of the thick square, we could ultimately reduce the dark current to a factor $9/25^{\text{th}}$. This would result in an improvement in V_{OC} of maximum $|\frac{k_B T}{q}\ln(9/25)| = 26$ mV. Note that this is achievable by a simply an improved device design. We have summarized the data of all 20 measured cells measured at NREL in Figure 4.6. All cells were processed identically; any changes are due to inconsistencies in fabrication, e.g. the thickness of the ITO layer.

Finally, to explore the general effect of nanostructuring on the V_{OC}, we have used Equation 4.1 (valid for any η_{int}, as long as there is no parasitic absorption), to investigate the potential for further improvement of present day solar cells by nanostructuring. We assume that bulk recombination is dominant, so the dark current of the nanostructured device is reduced to a fraction f of the bulk dark current: $J_0^{\text{nrad,nano}} = f J_0^{\text{nrad,bulk}}$, and that the short circuit current does not suffer from the reduction in material volume. The latter assumption is valid for materials such as silicon, InP and GaAs down to $f < 0.1$ [22, 40, 86]. We use

$$\eta_{int} = \frac{J_0^{rad}}{J_0^{rad} + J_0^{nrad}}. \tag{4.8}$$

This is the general equation which can be applied to bulk material. Equivalently we can write

$$J_0^{\text{nrad,bulk}} = J_0^{rad} \frac{1 - \eta_{int}^{bulk}}{\eta_{int}^{bulk}} \tag{4.9}$$

The material reduction affects only the nonradiative part of the dark current, thus we modify Equation 4.8 to

$$\eta_{int}^{nano} = \frac{J_0^{rad}}{J_0^{rad} + f J_0^{\text{nrad,bulk}}}. \tag{4.10}$$

Combining this with Equation 4.9 gives

$$\eta_{int}^{nano} = \frac{\eta_{int}^{bulk}}{\eta_{int}^{bulk} + f(1 - \eta_{int}^{bulk})}. \tag{4.11}$$

When assuming that the V_{OC} in the radiative limit V_{OC}^{rad} is not affected by the nanostructuring, and there is no parasitic absorption, we finally obtain

$$V_{OC}^{nano} \approx V_{OC}^{rad} + \frac{k_B T}{q} \ln \frac{\eta_{int}^{nano} \overline{P_{esc}}}{1 - \eta_{int}^{nano}(1 - \overline{P_{esc}})} = V_{OC}^{rad} + \frac{k_B T}{q} \ln \frac{\eta_{int}^{bulk} \overline{P_{esc}}}{f(1 - \eta_{int}^{bulk}) + \overline{P_{esc}}}. \tag{4.12}$$

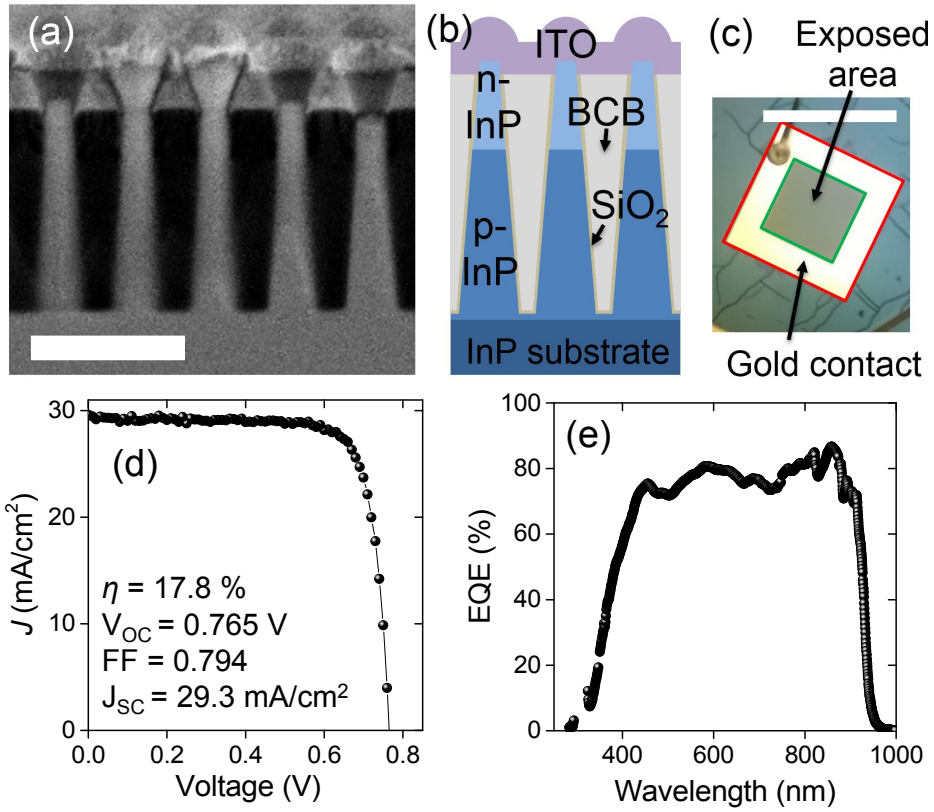

Figure 4.5: Characterization of nanostructured solar cell. a) Cross-sectional SEM image of the fully processed solar cell device. b) Schematic image of solar cell design. c) Microscope image of the solar cell device. The scale bar is 0.5 mm. The red square is the edge of the full solar cell, the green square is the edge of the area that is exposed to light. d) $J-V$ curve of the best of 20 nanowire solar cell devices, measured at 1 sun (AM1.5G) illumination. The photocurrent and efficiency are calculated based on the exposed area (green square in c). e) EQE measurement of one of the cells, measured at NREL. The J_{SC} of this cell is 26.5 mA/cm^2 (calculated based on exposed area). A bias light of 2.6 mA/cm^2 (based on full cell) was used.

In Figure 4.7a and b we have used this equation to express the maximum V_{OC} (for InP) as a function of the photon escape probability $\overline{P_{esc}}$ and the material filling fraction f, for two different values of η_{int}. We observe a clear logarithmic dependence of the maximum V_{OC} on $\overline{P_{esc}}$ and on f for the low internal luminescence efficiency. However, even layers with 90% internal luminescence efficiency can still gain tens of millivolts by improved photon escape probability and material volume reduction. Note that the choice of material only defines the value of the V_{OC} in the radiative limit, and has no influence on the loss terms related to f and $\overline{P_{esc}}$, which makes these effects generic for all solar cell materials.

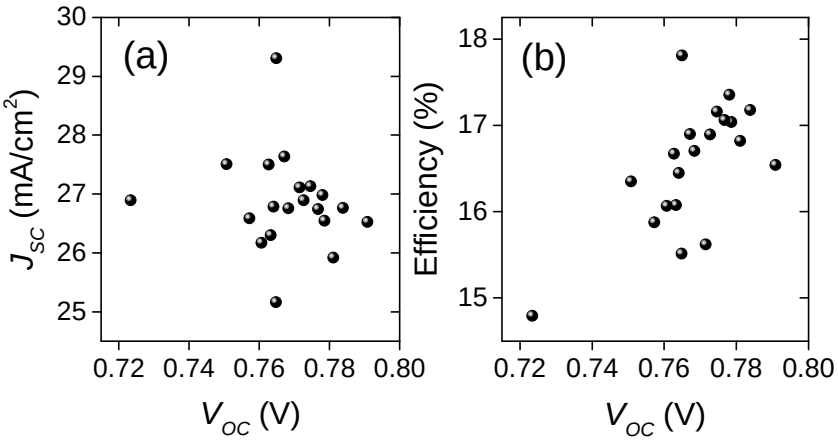

Figure 4.6: Distribution of cell parameters of the measured cells, in (a) the photocurrent density and (b) the efficiency. All parameters are calculated based on the area that is exposed to light.

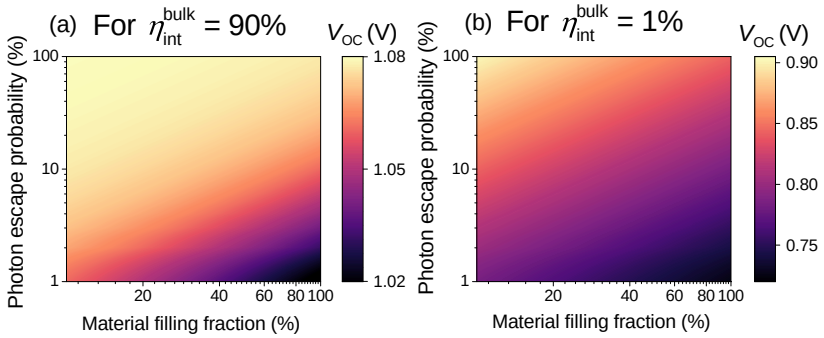

Figure 4.7: Enhancement of solar cell V_{OC} as a function of average photon escape probability and material filling fraction. (a, b) Calculated V_{OC} values for InP cells expressed in a log-log plot, as a function of the photon escape probability and the material filling fraction, for a fixed internal radiative efficiency of 90% (a) and 1% (b).

Figure 4.7 assumes that the surface recombination rate is small compared to the bulk recombination rate, while some materials instead suffer from a high surface recombination rate. However, for solar cell materials such as silicon [151, 152] and GaAs [65, 153] it has already been shown that surface recombination can be greatly reduced by proper surface passivation. For optimal solar cell performance, not only V_{OC} but also J_{SC} needs to be close to the theoretical maximum. As we have shown above a reduction of material can substantially enhance light absorption, and we note that the volume can be reduced to a factor $f \sim 0.08$ in nanowire

arrays, without losing any absorption with respect to a planar layer [21, 40, 86] as has been demonstrated for materials such as silicon, InP and GaAs. This makes the V_{OC} in Figure 4.7 indicative for the cell efficiency.

4.6 CONCLUSION

From Figure 4.7 we can derive the optimum design requirements for new record high-Voc solar cells: starting from a high internal radiative efficiency solar cell material, a very high photon escape probability should be combined with a very small amount of material. We finally conclude that nanostructuring is a very effective approach to increase both the photocurrent and the photovoltage to approach the Shockley-Queisser limit.

5

ENHANCED AND OMNIDIRECTIONAL ABSORPTION IN NANOWIRE SOLAR CELLS USING MIE SCATTERING ITO NANOPARTICLES

Photovoltaic cells based on arrays of semiconductor nanowires promise efficiencies comparable or even better than their planar counterparts with much less material. One reason is their high absorption cross section, but until recently the photocurrent has been limited to less than 70% of the theoretical maximum. Here we enhance the absorption in indium phosphide nanowire solar cells by employing broadband forward scattering of self-aligned nanoparticles on top of the transparent top contact layer. We measure omnidirectional absorption using Time-Reversed Fourier Microscopy and show that the broadband absorption enhancement of maximum 20% and average of 10% is due to Mie scattering. These insights lead to a measured short-circuit photocurrent of 29.3 mA/cm^2, which is among the highest reported for any III-V solar cell.

5.1 INTRODUCTION

Photovoltaic cells based on high-index planar material suffer from high reflection losses. Anti-reflection coatings and micro- or nanosized scattering particles have been widely used to reduce this reflection [26, 43, 147]. Nanoimprinted dielectric particles have been employed to enhance the incoupling of light in planar material. This enhanced incoupling has been explained in terms of Mie resonances, which scatter the light in the forward direction [34, 154, 155]. Recently, hemispherically shaped particles were imprinted on top of a planar silicon solar cell to improve light absorption, which was associated with the concept of a nanolens [156]. However, lenses become ill-defined at subwavelength dimensions, where ray-tracing is not valid. The interaction of light with scatterers, such as spheres or cylinders of dimensions comparable to the wavelength of light is generally explained by Mie theory [99, 133], which provides a solution to Maxwell's equations for electromagnetic waves obeying specific boundary conditions. Mie theory has proven to be very useful for dielectric and semiconductor nanoparticles [34] and nanowires [100, 142].

Nanowire solar cells have become an important field of study due to their intrinsic advantages over planar solar cells, leading to both a higher photocurrent and a higher photovoltage [22, 157]. It has been shown that the shape and size of the nanowire is very important for achieving a high absorption [21, 40]. However, until recently the highest photocurrent of a III-V nanowire solar cell (24.6 mA/cm^2) [85] was still significantly below the best planar cells of the same material (30.5 mA/cm^2) [158].

Some research groups have reported enhanced absorption due to nanostructuring of the transparent window layer of nanowire solar cells, and explained it in terms of optical concentration [159, 160]. However, optical concentration implies a modification of the angle-dependent emission and absorption patterns, which has not been investigated yet. Generally, omnidirectional absorption is an important property of solar cells since the incident sunlight is often not (only) coming from normal incidence. Strong absorption up to large angles with respect to normal incidence has been reported for black silicon [20] and also for nanowire arrays, both in simulations [79] and measurements [21, 40, 161]. However, no studies on the angle-dependent absorption of fully processed solar cells based on nanowire arrays have been reported. Therefore, a demonstration of enhanced absorption due to forward scattering of the transparent contact layer, which works well up to large angles, can provide important insights.

In this chapter, we demonstrate an omnidirectional enhanced photocurrent in a nanowire solar cell by using Mie scattering of the nanostructured transparent contact layer. This is the absorption mechanism behind the nanowire solar cell with a short-circuit current of 29.3 mA/cm^2, that is reported in Chapter 4.

5.2 TIME-REVERSED FOURIER MICROSCOPY ON NANOWIRE SOLAR CELLS

Our cells are based on tapered nanowires, that were etched from epitaxially grown n- and p-doped InP layers on top of an InP substrate. A layer of BCB was used to planarize the surface and indium-tin-oxide (ITO) was deposited as a transparent front contact. The ITO forms spherically shaped particles embedded in the planar ITO layer, that form a good Ohmic contact. More information on the fabrication can be found in ref. [162]. In Figure 5.1 we show the design of the nanowire solar cells, including a current density vs voltage plot of the best cell (Figure 5.1b).

We measure the angle-dependent photocurrent of a cell that has the geometry depicted in Figure 5.1c. Measuring the angle-dependent photocurrent of solar cells is usually done using a goniometer or rotational stage. However, the size of the excitation beam combined with the cell size limits the maximum angle to 48°.[1] In order to measure our small cell up to larger angles, we utilize Time-reversed Fourier Microscopy to excite the cell. This method, described in Section 3.2, uses a focused light source in the back focal plane of a microscope objective, in order to excite the cell with a plane wave under a microscope objective [80]. By scanning the focused beam, we illuminate the sample under the objective with a plane wave under angles varying from 0 to 72°. We scan one quarter of the back focal plane with a polarized beam from a diode laser at 532 nm, and perform a current-voltage scan for each position of the laser. The schematic of the setup and results are displayed in Figure 5.2.

1 The excitation spot is spread out over the cell when the angle increases. To keep the excitation beam width d_e entirely within the cell area (assuming a square cell of area d_c^2), the maximum oblique angle $\cos\theta_{\max} = d_e/d_c$. In our case, the cell has a width of 300 μm and an excitation beam width of 200 μm, which would limit $\theta_{\max}$ to 48°.

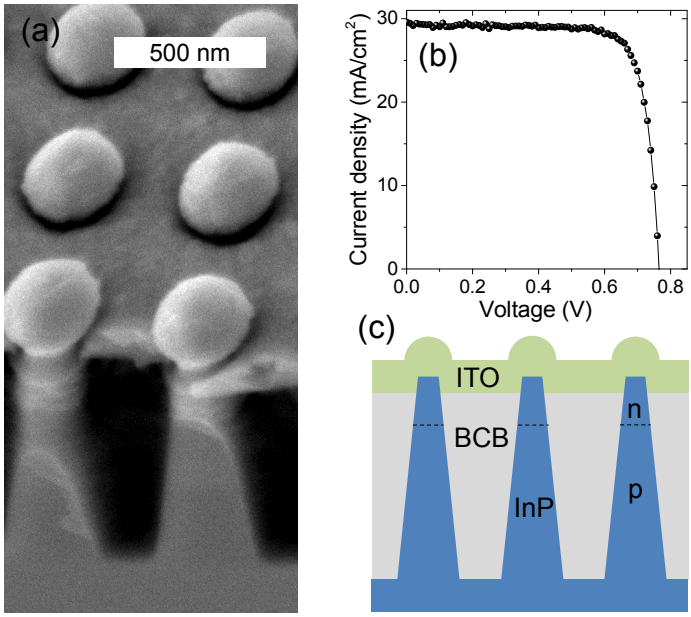

Figure 5.1: Nanowire solar cell. (a) SEM image of a cleaved nanowire solar cell device, acquired under a 30° angle. (b) current density vs voltage characteristic of the cell. The photocurrent was calculated based on the exposed active area of the cell. (c) Schematic of three unit cells of the device. The colored areas indicate InP (blue), BCB (gray), and ITO (green).

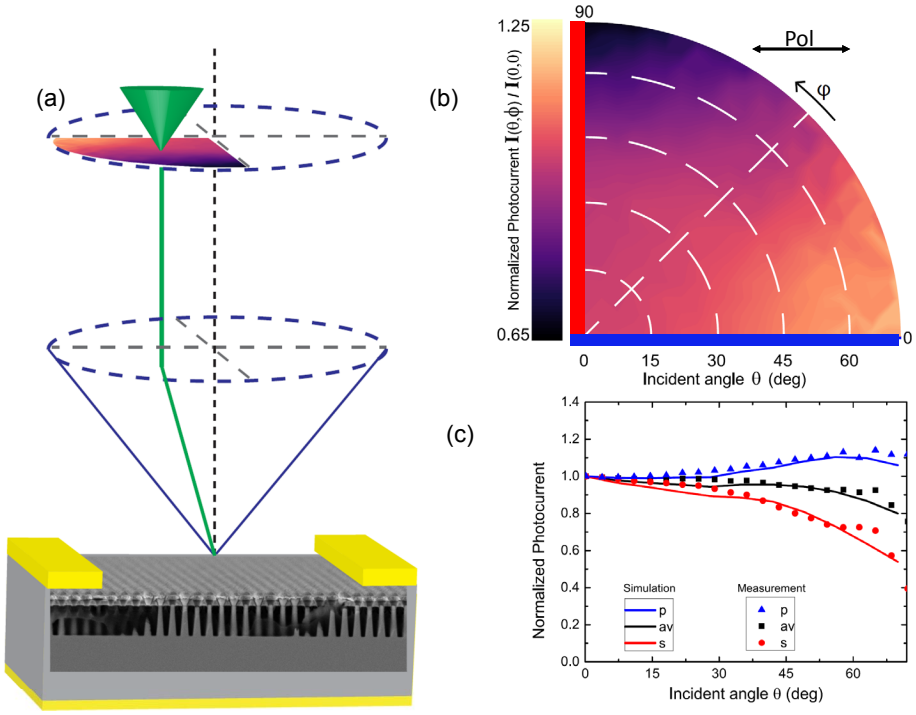

Figure 5.2: Angle-dependent photocurrent measurements. (a) schematic of the setup. (b) angle-dependent photocurrent measured using a laser scanning one quarter of the back focal plane, as indicated in (a). The photocurrent is normalized to the value at (θ,ϕ)=(0, 0). The orientation of the polarization of the excitation laser beam is shown by the black double arrow. (c) Profiles of the normalized photocurrent under polarized excitation in (b), for p-polarization (blue) and s-polarization (red). The measurements (squares) are shown with the absorption simulations acquired by FDTD (solid curves). The black curve and squares are the average of p- and s-polarization.

Figure 5.2b shows the measured angle-dependent photocurrent for the polarization of the laser oriented along the horizontal axis. This results in pure p-polarized excitation along the horizontal (blue) axis and pure s-polarized excitation along the vertical (red) axis (explained in Section 3.1). We see that the p-polarized excitation causes a growing photocurrent for larger oblique angles θ, while s-polarized excitation results in a decreasing photocurrent when θ increases. In Figure 5.2c we have depicted the profiles along the horizontal and vertical axis, together with their average.

5.3 SIMULATIONS AND MIE SCATTERING

We also perform absorption simulations using a finite-difference time-domain (FDTD) method in the commerical software package Lumerical. We model one unit cell of the device and use Bloch periodic boundary conditions. We use the refractive index of InP of n_{InP}=3.702 + 0.429i, for BCB we use n_{BCB}=1.55 and for ITO a value that was measured by ellipsometry, being n_{ITO}=2.1176 + 0.0029i. We excite a plane wave from top at a wavelength of 532 nm. We then simulate the electric fields in the unit cell, and calculate the absorption fraction over the volume V of the cell, using $a = \int \frac{1}{2}\varepsilon_0\omega|E|^2\text{im}(n)^2\text{d}V$, where ε_0 is the vacuum permittivity, ω is the frequency, E the electric field and n the respective refractive index at each position in the cell. In Figure 5.2c we have also plotted the angle-dependent absorption for both p- and s-polarized incident light and their average. We find good agreement between measurements and simulation. Measurement and simulations have been normalized to the value at $\theta = 0^\circ$ to allow direct comparison.

To investigate the role of the ITO particles, in Figure 5.3 we show the simulation results for a cell with a planar ITO layer, either with and without the ITO hemisphere. From the simulations we learn that the two angle-dependent absorption series follow the same trend. However, the cell with the ITO hemisphere on top shows an enhanced absorption for the entire angular range up to an incident angle of beyond 60°.

To look more into detail into the mechanism of the enhanced absorption by the ITO hemispheres, we simulate the field amplitude profiles in the device. Figure 5.4 shows the profiles, averaged for the two orthogonal polarizations of the light. If we compare the planar ITO layer (Figure 5.4a) to the ITO layer with hemispheres (Figure 5.4b), we clearly observe intensity enhancement in the top part of the nanowires. We conclude that the forward scattering of the light at the ITO nanostructures enhances the absorption. At a wavelength of 532 nm, the device absorption increases from 0.754 to 0.867 when introducing the hemispheres.

To show that Mie scattering is the mechanism behind the enhanced absorption of the nanostructured layer, we calculate the Mie scattering efficiencies from ITO spheres of a diameter of 350 nm, resembling the size of the ITO particles in our cell geometry (Figure 5.1a). As an approximation we take air as the embedding medium, since the light is incident from air. The scat-

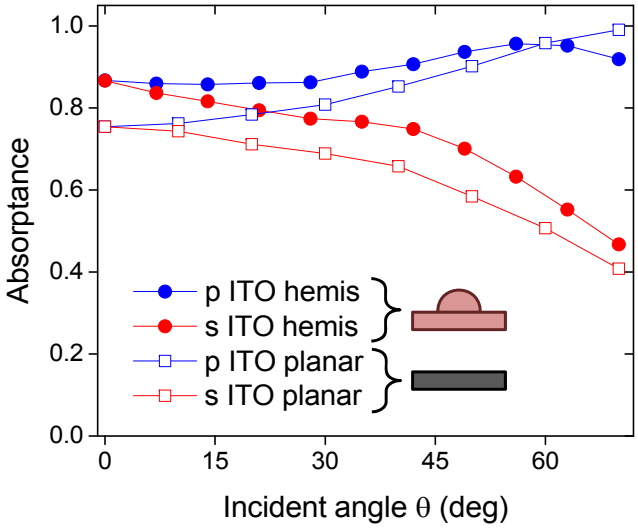

Figure 5.3: Simulated absorptance in nanowire solar cells with (dots) and without (squares) hemispherical ITO particle on top. Blue indicates p-polarization, red indicates s-polarization. The solid lines are guides to the eye.

tering and absorption efficiencies are defined as $Q_{scat} = \sigma_{scat}/\sigma_{geom}$ and $Q_{abs} = \sigma_{abs}/\sigma_{geom}$, where σ_{geom}, σ_{scat}, and σ_{abs} are the geometrical, scattering and absorption cross sections, respectively. These efficiencies are plotted in Figure 5.5a and b. The scattering efficiency is larger than 1 for the full wavelength range that is relevant for InP solar cells, and exceeds 3.5 for wavelengths from 450 to 800 nm. This broadband scattering is advantageous since it enhances the coupling of the light to the absorber layer of the cell. From Figure 5.5b we learn that the absorption in the ITO particles is negligible at wavelengths beyond 470 nm, which is important for the cell performance because the absorption should happen in the InP rather than in the ITO. To find out which resonances are responsible for the enhanced scattering, we calculate the extinction efficiencies Q_{ext} ($Q_{ext} = Q_{abs} + Q_{scat}$) of the electric and magnetic dipolar, quadrupolar and hexapolar resonances. We show these in Figure 5.6a. The different electric and magnetic resonances together cause the enhanced scattering of the ITO hemisphere into the nanowires.

Scattering in the forward direction by individual subwavelength dielectric particles has been experimentally studied recently [163–165]. Using Mie theory, we have calculated the backward and forward scattering efficiencies of ITO nanoparticles of d=350 nm in air, which we show in Figure 5.6b. A strong forward scattering was observed, which is characteristic of Mie scattering. The forward scattering may be even more enhanced in the realistic cells with respect to the Mie calculations due to the fact that the index of the nanowires-in-BCB layer is higher than that of air, which gives rise to field enhancement in this layer. The backward scattering efficiency

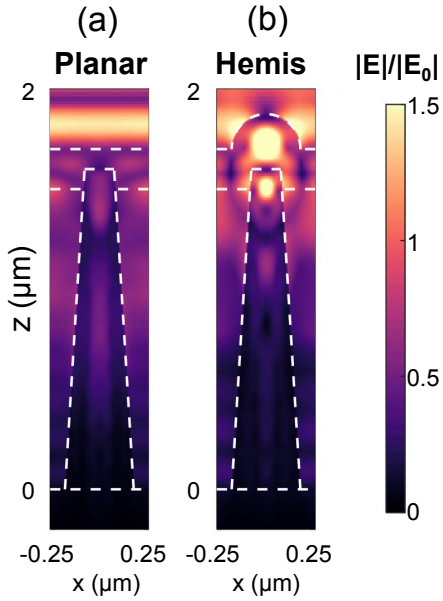

Figure 5.4: Near field amplitude profiles, simulated with FDTD, for planar ITO geometry (a), and hemispheric ITO surface (b). The simulations were performed using periodic boundary conditions for normally incident light at 532 nm, with a polarization averaged between parallel and perpendicular with respect to the displayed profile.

vanishes around 815 nm. This is exactly the wavelength at which the magnetic and electric dipolar scattering efficiencies have equal magnitude (as can be seen in Figure 5.6a). The destructive interference between the scattered fields in the particle cancels out the backscattering, which was first described by Kerker *et al.* [166]. We do not observe this in our measurements because the absolute value of the forward scattering is more important than the ratio of forward-to-backward scattering.

The absorption in fully processed devices is simulated using FDTD. Since we are interested in broadband absorption, we simulate the absorbed power in the cells excited by plane waves from 350 to 1000 nm at normal incidence (Figure 5.7a). The absorbed power is studied for cells with a planar ITO top contact (black spheres, a_{plan}) and the ITO hemispheres (red squares, a_{hemis}). Clearly, the absorption is enhanced when introducing the hemispheres. Since we know that ITO is transparent beyond 470 nm, the absorption in the InP has enhanced. Figure 5.7b displays the absorption enhancement by the hemispheres, $a_{\text{hemis}} - a_{\text{plan}}$. In the same plot we show also the Mie scattering efficiency at d=350 nm, reproduced from Figure 5.5a. We observe a remarkable qualitative correspondence between the scattering efficiency and the absorption enhancement. The enhancement measures up to 25% at 525 nm. The absorption enhancement shows more peaks than the scattering efficiency, which we attribute to Fabry-Pérot resonances

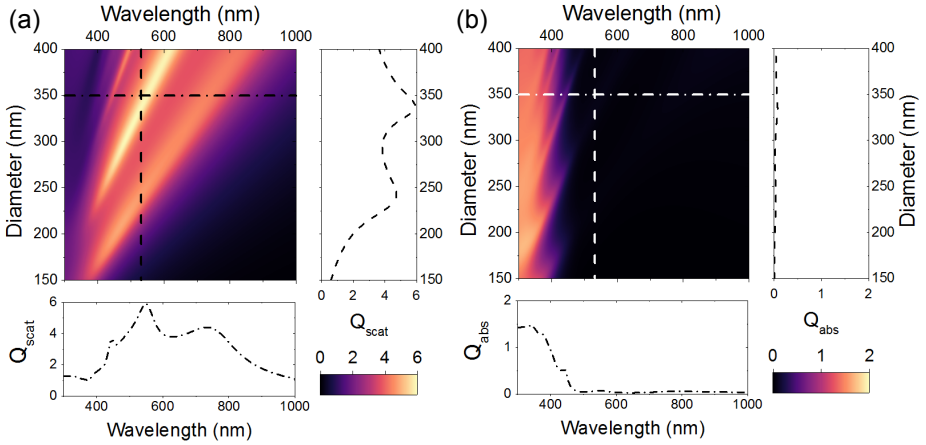

Figure 5.5: Mie scattering by spherical ITO particle in air. (a) scattering efficiency and (b) absorption efficiency, plotted a function of the diameter of the sphere d and the incident wavelength λ. Note that the color scale is different for the different graphs. The graphs at the bottom and right side of the color plot indicate profiles at d=350 nm (dash-dotted curve) and λ=532 nm (dashed curve).

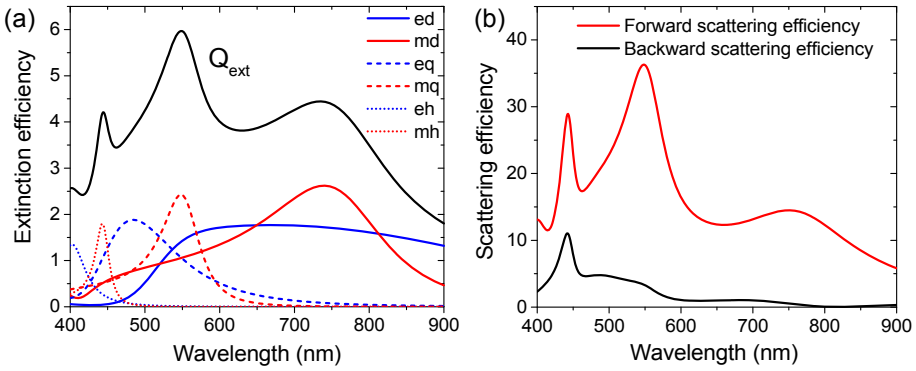

Figure 5.6: Mie scattering by ITO sphere. (a) Different contributions to extinction efficiency (black curve), calculated using Mie theory. The electric (blue) and magnetic (red) resonances are indicated by solid curves (dipolar resonances), dashed curves (quadrupolar resonances) and dotted curves (hexapolar resonances). Clearly, the extinction efficiencies is constituted by an interplay of several resonances. The legend reads the abbreviations for electric dipole (ed), magnetic dipole (md), electric quadrupole (eq), magnetic quadrupole (mq), electric hexapole (eh), and magnetic hexapole (mh). (b) Forward and backward scattering efficiencies of an ITO sphere of d=350 nm in air, calculated using Mie theory.

in either the ITO layer or the nanowires-in-BCB layer. The model is obviously only an approxi-

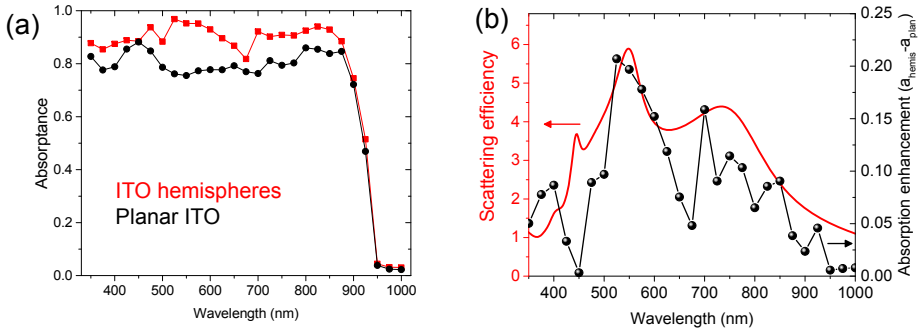

Figure 5.7: Comparison of simulations and Mie theory. (a) absorption simulation of hemispherical ITO layer (red squares) and planar ITO (black dots). The lines are guides to the eye. (b) Scattering efficiency for an ITO sphere in air at 532 nm (red curve) plotted with the numerical absorption enhancement $A_{\text{hemis}} - A_{\text{planar}}$ (black dots).

mation, but the absorption seems to be enhanced especially at the scattering resonances of the ITO spheres.

5.4 CONCLUSION

In conclusion, we have shown that properly designed hemispherical particles on top of the transparent top contact of nanowire solar cells enhance the absorption for the full relevant wavelength and incident angle range. Simulations and calculations show that forward Mie scattering is the mechanism behind this improvement. The absorption enhancement, which is wavelength-averaged 10% at normal incidence, makes the ITO hemispheres important design ingredients for solar cells based on nanowires.

6

DIRECTIONAL AND POLARIZED EMISSION FROM NANOWIRE ARRAYS

In this chapter we demonstrate a precise control of both the directionality and the polarization of the emission from nanowire arrays. By changing the nanowire diameter, we change the angular emission pattern from a large-angle doughnut shape, to a narrow-angle beam along the nanowire axis. In addition, we tune the polarization from unpolarized to either p- or s-polarized. Both the far-field emission pattern and its polarization are controlled by the number and type of guided or leaky modes supported by the nanowires, which are determined by the nanowire diameter.[1]

6.1 INTRODUCTION

Controlling the polarization and directionality of the emission of nanosized light sources is of great importance in the engineering of light-emitting diodes (LEDs) [113–115, 167], nanolasers [71, 168], single photon sources [102, 119, 169, 170], but also photovoltaics [50, 55, 129]. The bottom-up growth of semiconductor nanowires (NWs) allows a large design flexibility in parameters such as nanowire position, size, inter-wire distance and crystallographic orientation. This makes nanowires interesting candidates for the design of nanosized light emitters and detectors [171].

Previous studies had indicated the two main mechanisms that affect the nanowire emission directionality [93, 94, 172]. The directional emission of thin InP nanowires has been explained by coupling to leaky waveguide modes in the nanowire [103]. These modes modify the direction of the nanowire emission, causing an antenna-like behavior [101–103]. Identification of the relevant guided/leaky nanowire modes is important in tuning the direction of the far field emission [136]. The second mechanism that was associated with the emission directionality of NW arrays, is the coupling of the emission to modes in periodic arrays of nanowires, which behave as quasi-two-dimensional photonic crystals. The photoluminescence excited in one of the nanowires may couple to Bloch modes supported by the periodic structure and couple out to free space in certain directions. This directional outcoupling has been theoretically [173] and experimentally demonstrated [172, 174]. So far, no study – either theoretically or experimentally – of the interplay of both described mechanisms has been reported.

1 This chapter is based on: D. van Dam, D.R. Abujetas, R. Paniagua-Domínguez, J.A. Sánchez-Gil, E.P.A.M. Bakkers, J.E.M. Haverkort, and J. Gómez Rivas, "Directional and polarized emission from nanowire arrays", *Nano Lett.* 15 (7) 4557-4563 (2015).

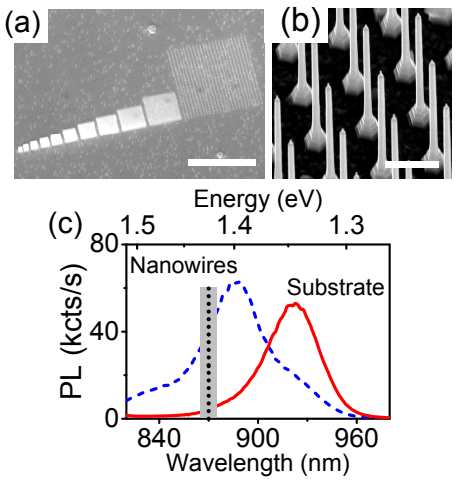

Figure 6.1: Nanowire sample and emission spectra. (a) Scanning electron micrograph (SEM) of the sample with different nanowire arrays and (b) a close-up one of the nanowire arrays. The images were taken at 30 degrees glancing angle, the scale bars are 100 and 2 μm, respectively. (c) Photoluminescence (PL) emission spectrum of nanowires (blue, dashed line) and the underlying substrate (red, solid line). The black dotted line indicates the transmittance maximum of the band pass filter used for the Fourier emission measurements, the width of the shaded area indicates the spectral FWHM of the filter.

In addition to directionality, control over the polarization of the emission is important for many applications, such as solid-state lighting, sensing and optical communication. Thin nanowires have the ability to emit strongly polarized light [73, 175], which is a useful property for displays and sensing [167], but may hinder the application in quantum optics [100]. The nanowire polarization anisotropy has been first explained in the electrostatic limit by the elongated shape of the nanowires and the high refractive index contrast with the environment [73], and it has later been described in terms of coupling to Mie resonances [100]. On top of that, the selection rules of the band structure of the emitting material also affect the polarization [175]. However, it is unknown how the polarization of the nanowire emission depends on the diameter, taking into account both waveguide modes and selection rules.

In this chapter we discuss the polarized and directional emission properties of semiconductor nanowire arrays, which were analyzed through Fourier microscopy. We demonstrate that the nanowire diameter is the essential parameter, providing control over the directionality of the emission, and show that similar far-field emission patterns can have totally different polarized emission. This behavior is explained by the coupling of the emission to different waveguide modes confined to the nanowire. In addition, the emission pattern is modulated by the periodic array.

6.2 MEASUREMENT DESCRIPTION

Our sample consists of arrays of indium phosphide (InP) nanowires with a period ranging from 0.8 to 5 μm. A combination of axial vapor-liquid-solid (VLS), radial vapor-solid (VS) growth, and the varying period, led to different nanowire diameters for the different arrays. Scanning electron micrograph of the sample can be found in Figure 6.1a-b, and a typical photoluminescence spectrum of nanowires and substrate is shown in Figure 6.1c. The mixed wurtzite-zincblende crystal structure of the nanowires gives rise to blue-shifted emission compared to the zincblende emission from the substrate. The emission patterns of the nanowires were obtained by Fourier microscopy as described in detail in Section 3.1. In a Fourier microscope the back focal plane of the objective is imaged, in order to obtain the parallel (in-plane) components of the wave vectors of the far-field emission. These wave vectors can be converted into emission angles as explained in ref. [104]. The Fourier images were collected by a CCD camera with a band pass filter with a transmission maximum at 870 nm (dotted black line in Figure 6.1c), and a bandwith of 10 nm. For all nanowire arrays, a small fraction of the emission transmitted through the band pass filter stems from the substrate, as can be appreciated from Figure 6.1c. This fraction is lower than 25% for all the arrays (typically 10%), and depends on the amount of absorption of the excitation beam in the nanowires. The small fraction of emission from the substrate causes a Lambertian-like background in the Fourier images, without qualitatively affecting them.

6.3 RESULTS AND DISCUSSION

6.3.1 *Directional and polarized emission*

First, we focus on single-nanowire effects in the emission patterns. We will discuss the interaction with the surrounding array later. The excitation beam has a diameter of about 1 μm on the sample, therefore exciting only one nanowire in all arrays. Figure 6.2a-c show polar plots of the measured unpolarized far-field emission patterns of nanowires with three different diameters d (100±10, 180±6, 295±13 nm, referred to as 'thin', 'intermediate', and 'thick'). In this emission pattern series, we observe a remarkable change from doughnut-shaped emission (Figure 6.2a) to narrow-angle beaming at small angles with respect to the nanowire's axis (Figure 6.2b). Interestingly, the emission pattern from the thickest nanowires again reveal a doughnut-shaped far-field emission (Figure 6.2c). These images illustrate that it is possible to totally change the direction of the emission by tailoring the nanowire diameter.

For further insight into the origin of this remarkable phenomenon, we have measured the polarized directional emission patterns of the nanowires, by placing a polarizer in front of the Fourier camera. The polarized emission patterns are shown in Figure 6.2d-f. In this configu-

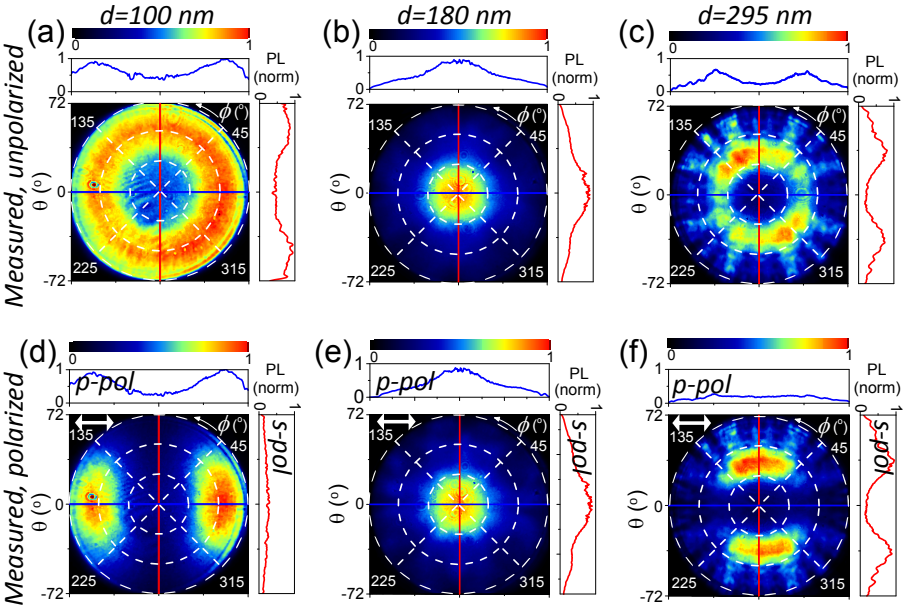

Figure 6.2: Fourier images of emission. All intensities are normalized to their maximum value. (a-c) Unpolarized Fourier emission patterns for three different nanowire diameters *d*: 100, 180, and 295 nm, respectively. The color indicates the normalized PL intensity. Cuts through the center are displayed at the top and right side of each color plot. (d-f) Same as (a-c), but the emission recorded through a linear polarizer oriented along the white double arrow in each plot. P-polarized emission is recorded along the horizontal axis (blue profile, p-pol), s-polarized emission along the vertical axis (red, s-pol).

ration, the emission recorded along the polarizer's transmission axis (horizontal direction) is purely p-polarized, whereas the emission recorded along the orthogonal axis (vertical direction) is purely s-polarized [103]. A full description of the polarization-dependent collection is provided in Section 3.1. We experimentally observe that the light is almost entirely p-polarized for small nanowire diameters. On the contrary, we observe that thick nanowires emit strongly s-polarized light, while the polarized emission pattern of the intermediate nanowire is unpolarized. To understand the origin of this variation, we investigate the role of the waveguide modes supported by the nanowire geometry.

The dispersion of the available waveguide modes in a nanowire can be calculated from Maxwell's equations, applied to an infinite cylinder (as explained in Section 2.2), and is shown in Figure 6.3a. Note that the diameters expressed in the dispersion diagram are calculated for a circular cross-section, while our nanowires have a hexagonal cross-section. It has been shown that the modes for a hexagonal nanowire-cross-section are similar to modes for a circular nanowire-cross-section with a slightly lower diameter [176]. Therefore, we choose the 'equivalent circular diameters' to be 90, 165 and 275 nm, respectively. The dispersion curves are labeled as transverse magnetic (TM), transverse electric (TE), and magneto-electric (HE) modes. The light cones of air and InP are expressed using the white and gray areas in Figure 6.3a. Waveguide modes are 'leaky' if their dispersion curve is in the air light cone. In this case, the mode radiates (leaks) into the surrounding medium (air). If the dispersion curve is in the InP light cone, the mode is guided by the nanowire. From the dispersion relation we obtain the propagation constant k_z for each mode, at the diameter of interest.

Using the k_z's, we can calculate the far-field patterns of the available waveguide modes by a 1D current model [136]. We explain this model in more detail in Section 2.2.3. The calculated polarized emission patterns (for the dominant modes) are shown in Figure 6.3b-d. These patterns can be directly compared to the measured polarized patterns, Figure 6.2d-f. The color plots and polarized profiles (cuts at top and right side of each color plot) show a very similar shape. From the good qualitative correspondence between experimental and modeled polarized patterns, we conclude that the differently polarized patterns are caused by different waveguide modes. For the thin nanowire the emission is determined by the leaky TM_{01} mode and not by the weakly guided HE_{11} mode. This counterintuitive result is caused by the larger electric field of the leaky TM_{01} mode inside the nanowire compared to that of the fundamental HE_{11} mode, whose electric field is mainly present in the surrounding medium. This can be seen by calculating the electric field profiles as shown in Figure 6.4, and comparing the two modes. We conclude that the emission from a source located in the nanowire preferentially couples to the TM_{01} mode[103]. For the intermediate nanowire diameter the emission is given by the guided HE_{11} mode. In this case, the electric field of the HE_{11} mode is better confined inside the nanowire. Finally, for the thickest nanowire, the emission couples preferentially to the guided TE_{01} mode. The main differences between the measurements of Figure 6.2 and the calculation of Figure 6.3 are at the background of the measurements, which can be attributed

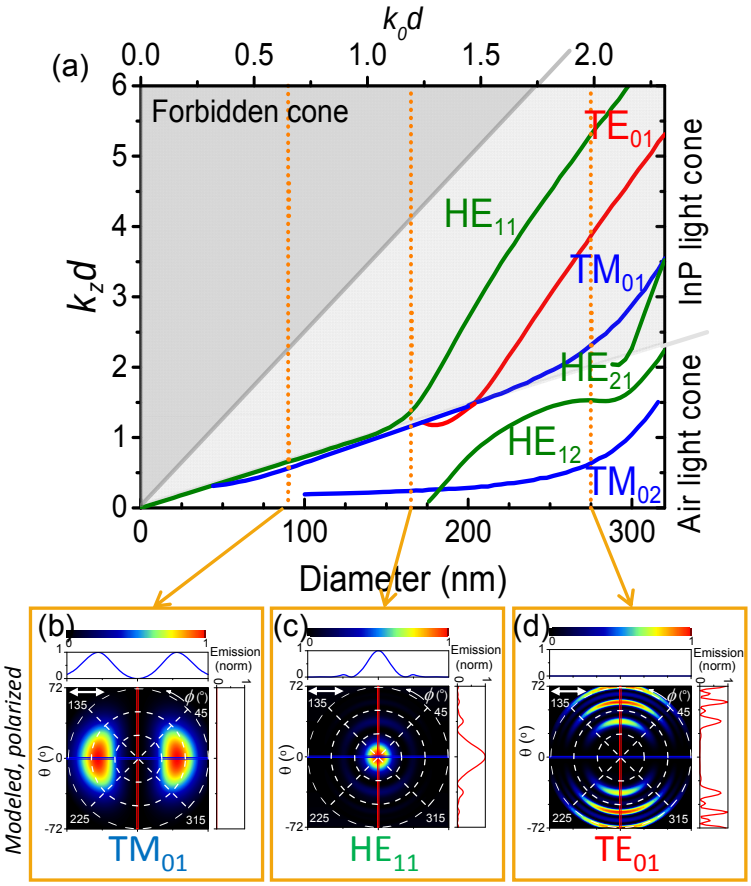

Figure 6.3: Waveguide modes account for direction and polarization of the emission. (a) Dispersion relation of leaky and guided modes for an infinitely long cylinder with diameter d, expressed as (real component of) wavenumber k_z against size parameter k_0d. At the bottom horizontal axis the diameter is shown for a cylinder with n=3.43 (InP) at 870 nm. Vertical dotted lines indicate the three diameters that we have further investigated. (b-d) Modeled emission patterns that correspond to the patterns in Figure 6.2(d-f), calculated using the 1D current model. The specific mode for which the pattern is calculated is indicated below each image.

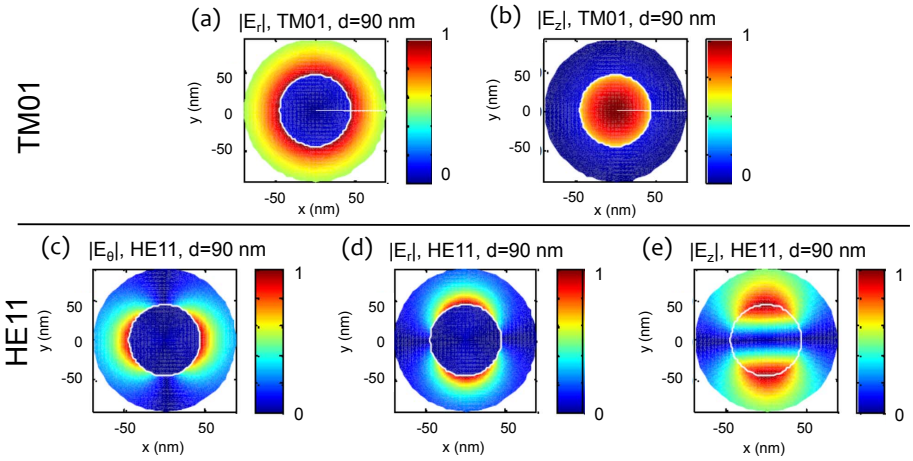

Figure 6.4: Electric field profiles of waveguide modes. Profiles are calculated for infinite cylinders with d=90 nm, for components in the θ-, r-, and z-direction. The TM_{01} mode is leaky and the HE_{11} mode is weakly guided.

to the contribution of the substrate to the emission, and the broader peaks in the measurements due to inhomogeneities in the sample. In the calculations for the thickest nanowires (Figure 6.3d) we observe emission at large emission angles ($\theta > 50°$), which is not visible in the measurement (Figure 6.2f). This absence of large-angle emission is explained by scattering of the nanowire emission due to the surrounding array. The interaction between the nanowire and the surrounding array will be discussed later.

We have also investigated whether the waveguide modes responsible for the emission can be excited from the luminescence in the nanowire. Therefore, we have performed finite-element method (FEM) simulations based on emitting dipoles inside the nanowires (shown in ref. [58]). These simulations consider a circular cylinder with dipole halfway the length of the nanowire, emitting at a wavelength of 870 nm. The dipole is located on the nanowire axis for the thin and intermediate nanowires, oriented parallel (thin) or perpendicular (intermediate) to the nanowire axis. For the thick nanowire, the dipole is replaced by a series of dipoles located on a ring around the nanowire axis, at a radius of 110 nm, and oriented perpendicular to the nanowire axis. These simulations (shown and discussed in detail in ref. [58]) indeed confirm the coupling of the emission to the aforementioned waveguide modes. We conclude that by tailoring the waveguide modes we are able to drastically change the angular distribution and polarization of the far-field emission.

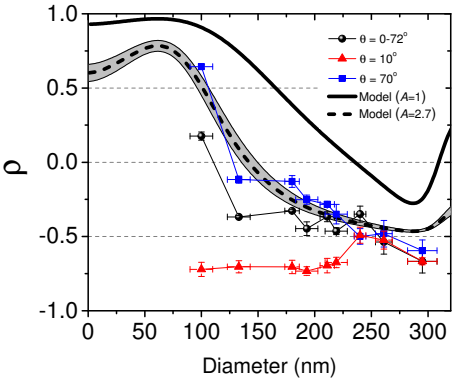

Figure 6.5: Role of dielectric contrast and viewing angle in the polarization anisotropy of the emission by nanowires. Data points show the measured polarization anisotropy ρ as a function of the nanowire diameter, for emission angles integrated over 0 to 72° (black spheres), or at 10° (blue circles) and 70° (red triangles). The data points are connected as a guide to the eye. Errorbars denote the statistical variance in diameter (determined by SEM imaging) and polarization anisotropy. The solid line is the calculated polarization anisotropy using the model of Ruda and Shik [96], for dipole anisotropy ratio A=1. The dashed line is the model with the fitted value A=2.7. The gray shaded area indicates the standard error of the fitted curve.

6.3.2 *Polarization anisotropy*

To investigate the polarization-dependent emission in more depth, we have determined the polarization anisotropy of the emission as a function of the nanowire diameter. The polarization anisotropy ρ is generally defined as $\rho = (I_{\parallel} - I_{\perp})/(I_{\parallel} + I_{\perp})$, where $I_{\parallel}$ and $I_{\perp}$ are the parallel and perpendicular polarized emission intensities with respect to the nanowire axis [73, 96]. In our angle-dependent configuration, $I_{\parallel} = I_p \sin\theta$ and $I_{\perp} = I_s$, where θ is the emission angle with respect to the nanowire axis. The polarized emission intensities I_p and I_s are obtained by integrating the polarized emission patterns along the horizontal and vertical axes ($\phi = 0° - 180°$ and $\phi = 90° - 270°$), respectively.

In Figure 6.5 we show the polarization anisotropy of the measured nanowire emission as a function of the nanowire diameter (black spheres). These data are the polarization anisotropies integrated over all angles θ captured by the microscope objective, i.e. from 0° to 72°. We observe a gradual decrease in ρ, being a transition from parallel to perpendicular polarized emission, when increasing the diameter. To investigate the dependence of the polarization anisotropy on the emission angle θ, we determine ρ for a small (10°, red triangles) and a large angle (70°, blue squares). We observe a large difference in polarization anisotropies between the different emission angles. At small θ, a small ρ is found because of the low $I_{\parallel}$ in this direction. There is no strong change in ρ depending on the diameter, except for the diameters

larger than 200 nm, where coupling to the transverse (polarized) guided modes (TM_{01}, TE_{01}) is possible. At large θ, a clear decrease of ρ is visible. It is important to mention that previous reports of the polarization anisotropy of the emission of single nanowires were based on measurements done by collecting the emission with large-NA objectives[73, 98, 100, 175, 177]. The strong angle-dependence of the polarization anisotropy of the nanowires indicates that it is important to consider the NA of the objective when analyzing this polarized emission. Clearly, the choice of NA (and therefore maximum captured emission angle θ_{max}) affects the measured value of polarization anisotropy. Fourier microscopy allows measuring the angle-dependent polarization anisotropy, thus taking into account this peculiar phenomenon.

The decreasing trend of ρ for increasing diameter at $\theta = 70^\circ$ is explained by a model for the polarization anisotropy as a function of the normalized frequency $\omega r_0/c$, which was introduced by Ruda and Shik [96]. This model considers an isotropically oriented dipole emitting at frequency $\omega = 2\pi c/\lambda$, embedded in an infinitely long nanowire (with radius r_0 and permittivity ε), and describes the emission at an angle $\theta = 90^\circ$ with respect to the nanowire axis. The dipole is located at the axis of the nanowire along the z-axis ($r = 0$, $z = 0$ in cylindrical coordinates). Two distinct cases can be distinguished: one with the dipole moment $\vec{d}_0$ oriented along the nanowire axis ($d_0 = d_{0z}$), and one with the dipole moment oriented perpendicular to the nanowire axis ($d_0 = d_{0x} = d_{0y}$). In both cases, Ruda and Shik calculated the electric field scattered by the nanowire and concluded that the dipole can be replaced by an effective dipole to achieve the same far-field intensity. For $r_0, \lambda \ll r$, this effective dipole strength is given by [96]

$$d_z = d_{0z}\sqrt{\varepsilon_c}\frac{J_1(kr_0)H_0(kr_0) - J_0(kr_0)H_1(kr_0)}{\sqrt{\varepsilon_c}J_1(kr_0)H_0(k_0r_0) - \sqrt{\varepsilon_e}J_0(kr_0)H_1(k_0r_0)} \equiv A_z d_{0z}, \tag{6.1}$$

and

$$d_x = d_{0x}\sqrt{\varepsilon_c}\frac{J_1'(kr_0)H_1(kr_0) - J_1(kr_0)H_1'(kr_0)}{\sqrt{\varepsilon_e}J_1'(kr_0)H_1(k_0r_0) - \sqrt{\varepsilon_c}J_1(kr_0)H_1'(k_0r_0)} \equiv A_x d_{0x}, \tag{6.2}$$

where $k = \sqrt{\varepsilon_c}\omega/c$ and $k_0 = \sqrt{\varepsilon_e}\omega/c$, ε_c and ε_e are the permittivities of nanowire and vacuum, respectively, and c is the speed of light in vacuum. When we consider the entire nanowire emitting instead of a single dipole, we need to integrate along z. Assuming isotropic internal emission ($d_{0z} = d_{0x}$), it has been shown that the intensity ratio for the far-field polarization is given by [91]

$$\frac{I_\parallel}{I_\perp} = \frac{d_x^2 + 2d_z^2}{3d_x^2}, \tag{6.3}$$

from which the polarization anisotropy ρ can be calculated:

$$\rho = \frac{I_\parallel - I_\perp}{I_\parallel + I_\perp} = \frac{\frac{I_\parallel}{I_\perp} - 1}{\frac{I_\parallel}{I_\perp} + 1} = \frac{d_z^2 - d_x^2}{d_z^2 + 2d_x^2}. \tag{6.4}$$

In words, this model explains the polarization anisotropy of the emission by the dielectric contrast between the nanowire (which in our case has refractive index n=3.43 and radius r_0) and

the surrounding medium (n=1), causing a suppression of the perpendicularly polarized electric field inside thin nanowires. The explanation of the polarization anisotropy of nanowires in terms of the dielectric contrast has been identified to Mie resonances and leaky modes. It has been shown that these descriptions are equivalent to each other [100, 103, 104]. The values of ρ calculated with the Ruda/Shik model, for an InP nanowire at an emission wavelength of 870 nm, are plotted in Figure 6.5 as a solid line. The suppression of the perpendicular electric field causes a strong polarization parallel to the nanowire, i.e. $\rho \approx 1$, for the thin nanowires, when $\omega r_0/c \ll 1$. This assumes that the field inside the nanowire is constant, which only works in the electrostatic limit [73]. For larger values of $\omega r_0/c$, the electrostatic approach does not hold any more, and ρ decreases until a local minimum around a diameter of 280 nm, and increases again.

At small angles ($\theta = 10^\circ$), the Ruda and Shik model fails in describing the measurements. As mentioned above, this model only describes the emission at large angles ($\theta = 90^\circ$), where there is no contribution from guided modes. At large angles ($\theta = 70^\circ$) the decreasing trend of ρ from the model is followed by the measurements, indicating that in this condition the dielectric contrast between the nanowire and the surrounding air is dominating the polarization anisotropy. However, there is a vertical offset in ρ between measurement and model. To investigate this offset, we look in more detail to the differences between experiment and model. The effect of the difference in θ between measurement and model (70° vs 90°) is negligible, since $\sin 70^\circ \approx \sin 90^\circ$. Therefore, the explanation for the difference should be found in an anisotropic internal emission of the differently oriented dipoles. The model contains the intrinsic emitting dipole strengths d_{0x}, d_{0y} and d_{0z} for dipoles oriented perpendicular and parallel to the nanowire axis. The ratio $A \equiv d_{0x}/d_{0z} = d_{0y}/d_{0z}$ is set to 1 (isotropic internal emission) in the calculation represented by the black solid line in Figure 6.5. Fitting this parameter A to the measured large-angle polarization anisotropy gives a value of $A = 2.7 \pm 0.3$. The fit is added to Figure 6.5 (dashed line). This value of A indicates a larger emission strength of the perpendicular dipole, which could be explained by the selection rules of the wurtzite crystal phase of the nanowire. These selection rules affect the dipole strengths of the emitting transitions. In zincblende crystal phase both parallel and perpendicular polarizations are allowed. However, in wurtzite crystal phase only the perpendicular polarization is allowed [178, 179]. Our nanowires are predominantly wurtzite (as can be concluded from the PL spectrum in Figure 6.1c), so emission from dipoles polarized perpendicular to the nanowire will dominate. Using the band pass filter shown in Figure 6.1c we select mainly the emission of the wurtzite InP band gap, which results in an increase of A and a decrease of the measured value of ρ.

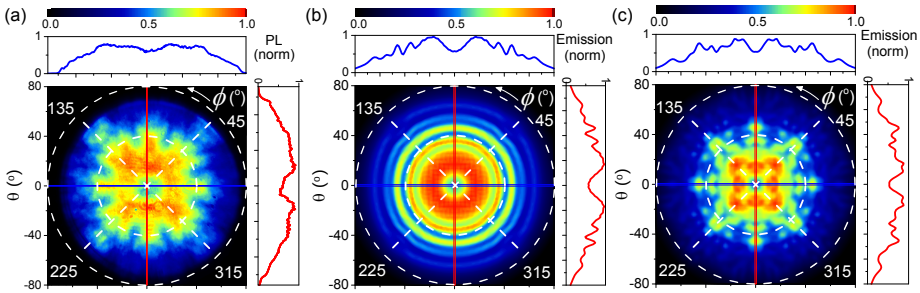

Figure 6.6: Effect of the array on the directional emission pattern. The intensities are normalized to their maximum value. (a) Fourier emission pattern of a nanowire array with period $p = 2\,\mu$m and nanowire diameter $d = 219$ nm. The intensity profiles through horizontal and vertical axes are shown at the top and right sides. (b) FDTD simulated far field pattern of three orthogonal dipoles in the center of a single nanowire. (c) FDTD simulated far field pattern for a nanowire in an array with $p = 2\,\mu$m.

6.3.3 *Influence of surrounding array*

In order to describe the interplay between the waveguide modes in the nanowire and the Bloch modes in the periodic array, we show the directional emission of a nanowire array with a pronounced square symmetry, imposed by the 2D nanowire array (Figure 6.6a). This array has a nanowire diameter $d = 219 \pm 9$ nm and an array period p=2 μm. To model the far-field emission pattern of nanowires placed in an array we have performed numerical electromagnetic simulations of the nanowires under study, using the finite-difference time-domain (FDTD) method. The simulations allow us to quantify the relative contributions of waveguide modes and Bloch modes to the far-field emission pattern. First, we obtain the emission pattern from a point dipole embedded in a single nanowire with dimensions equal to the measured nanowire (Figure 6.6b). For simplicity, the dipole is located in the center of the nanowire. Varying the position of the dipole over the nanowire changes the coupling efficiency to the different guided modes. This is discussed in detail elsewhere [136, 180]. A monitor on top of the nanowire records the fields generated by the simulation, and a near-to-far-field transformation is used to derive the far-field pattern. The directional emission measurement and corresponding simulation show a similar emission pattern: a local minimum for $\theta = 0°$ and a doughnut-shape with a maximum at about $\theta = 20°$. The measurement however shows a pronounced square symmetry, deforming the doughnut-shape, which is absent in the simulation.

To determine the contribution of the array to this emission pattern, we have also calculated the far-field emission patterns of emitting dipoles embedded in the central nanowire of a 7x7 nanowire array, which is shown in Figure 6.6c. The general pattern of the emission is preserved: a minimum for $\theta = 0°$ and a maximum at about $\theta = 20°$. This can be clearly seen at the profile

cuts in Figure 6.6. However, the array modulates the emission pattern, imposing the square symmetry that is seen in the measurement.

For getting further insight in the role of the array in the emission, we envision the nanowire array as a 2D-photonic crystal, established by the periodic refractive index modulation, which gives rise to Bloch modes [172, 174, 181]. Using the freely available program MIT Photonic Bands [182], the dispersion of Bloch modes in the plane of the array was calculated. It is sufficient to calculate the wavenumbers within the irreducible Brillouin zone, which is the triangle formed by Γ, X and M points in the reciprocal lattice (using the definitions in ref. [181]). We distinguish TE (electric field perpendicular to the nanowires) and TM (electric field parallel to the nanowires) modes, with increasing density as the frequency increases. The band diagram for the array of Figure 6.6a is shown in Figure 6.7a.

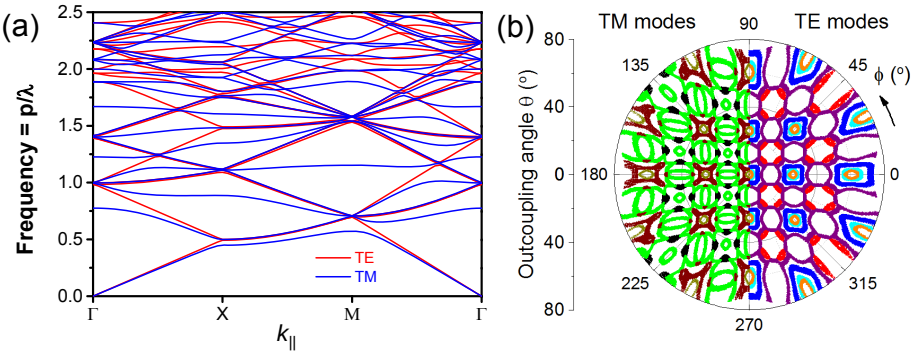

Figure 6.7: Dispersion of Bloch modes. (a) Band diagram of a 2D photonic crystal of infinitely long cylinders (d=219 nm, $n_{cylinder}$=3.43, period p=513 nm) in a medium with n=1. The parallel wavenumber $k_{||}$ is expressed on the horizontal axis, where Γ, X and M are the corners of the irreducible Brillouin zone. (b) Outcoupling angles of Bloch modes for the same array at a wavelength of 870 nm; different colors represent different eigenmodes in a 2D photonic crystal. The left side shows TM modes, the right side TE modes.

When the light coupled to Bloch modes scatters at the edge of the nanowire layer (determined by the finite nanowire length), it couples out into the into the far field. Due to conservation of parallel momentum, it couples out in a discrete collection of possible emission angles.

The outcoupling angles calculated from the Bloch mode dispersion are shown in Figure 6.7b. In these calculations, we observe a square-like symmetric angular distribution with a multitude of outcoupling angles for the allowed Bloch modes in the nanowire photonic crystal. We observe that the detailed structure of the emission pattern in Figure 6.7b resembles the measured and simulated square-symmetric emission pattern of the nanowire photonic crystal,

although our measured profiles show angular broadening due to the finite length of the nanowires and sample inhomogeneities.

Based on the measurements and simulations of Figure 6.6 and Figure 6.7, we conclude that the doughnut-shapes determining the envelope of the emission pattern of the arrays arise from the modes generated in the individual nanowires, while the square-symmetric features in the array emission patterns are due to coupling of the emission to Bloch modes in the periodic arrays. However, these modifications are not dominant, as can be appreciated by comparing the cuts of the measurements to the simulations. The emission of the array is thus mainly explained in terms of the emission of individual nanowires as discussed in the previous sections.

6.4 CONCLUSION

In conclusion, we have shown that the directionality and polarization of the emission of nanowires can be precisely tuned by introducing small changes in the nanowire diameter. This remarkable feature is caused by the efficient coupling of the emission to different waveguide modes, which dominate the emission outcoupling and polarization. Tuning the nanowire diameter enables selecting, for instance, unpolarized beaming, or linearly polarized doughnut-shaped emission. This work opens up new possibilities for light emitting devices and nanosized light sources with predesigned polarization and direction of the emission, without using any external optical element.

7

STRONG DIAMETER-DEPENDENCE OF NANOWIRE EMISSION COUPLED TO WAVEGUIDE MODES

The emission from nanowires can couple to waveguide modes supported by the nanowire geometry, thus governing the far-field angular pattern. To investigate the geometry-induced coupling of the emission to waveguide modes, we acquire Fourier microscopy images of the photoluminescence (PL) of nanowires with diameters ranging from 143 to 208 nm. From the investigated diameter range we conclude that a few nanometers difference in diameter can abruptly change the coupling of the emission to a specific mode. Moreover, we observe a diameter-dependent width of the Gaussian-shaped angular pattern in the far-field emission. This dependence is understood in terms of interference of the guided modes, which emit at the end facets of the nanowire. These results are important for the design of quantum emitters, solid state lighting and photovoltaic devices based on nanowires.[1]

7.1 INTRODUCTION

Vertically standing semiconductor nanowires are of interest for the realization of quantum optical devices [76, 102], light-emitting diodes (LEDs) [68] and solar cells [78, 85]. For all of these applications, the angle-dependent (or directional) interaction of nanowires and light is of great importance. For instance, quantum emitters require excellent coupling into fiber optics, for which a Gaussian angular emission pattern is advantageous [123], while LEDs typically need a narrow beam for efficient illumination [183]. Furthermore, solar cells require omnidirectional light absorption to trap diffuse light, although unidirectional absorption might be preferential for optimal solar cell efficiency in the radiative limit [129], i.e. the re-emission cone of light from solar cells needs to be as narrow as possible in order to match the incident solid angle of solar radiation and thus reduce entropy losses [52, 54, 55]. In all these cases, control over the directional emission and absorption is crucial for the device performance.

Both the directional emission [58, 103] and directional absorption [80, 142] of light in individual semiconductor nanowires has been investigated recently. Indium phosphide (InP) and gallium arsenide (GaAs) have proven to be among the leading materials for quantum emitters [119, 121] and solar cells [85, 89] based on nanowires. For these applications and materials, the approximate optimal diameter for absorbing the solar spectum has been estimated to be

1 This chapter is based on: D. van Dam, D.R. Abujetas, J.A. Sánchez-Gil, J.E.M. Haverkort, E.P.A.M. Bakkers, and J. Gómez Rivas, "Strong diameter-dependence of nanowire emission coupled to waveguide modes", *Appl. Phys. Lett.* 108, 121109 (2016)

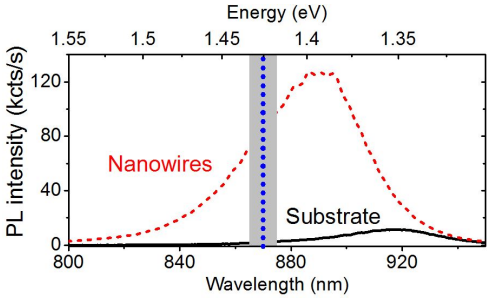

Figure 7.1: Typical microphotoluminescence spectrum from the nanowires (red, dashed) and the supporting substrate (black, solid). The blue, dotted line indicates the central wavelength of the band pass filter used in the experiments, while the width of the shaded area indicates the spectral FWHM of the filter.

177-220 nm [107, 121]. The reason for this optimal diameter is the onset of efficient coupling to the fundamental HE_{11} waveguide mode [184], which improves both absorption (for photons with energy just above the material bandgap energy) and guiding/outcoupling (for photons with energy below the material bandgap energy). The first transverse waveguide modes (TM_{01} and TE_{01}) have their cut-off diameter close to the optimal diameter, which may influence the directional outcoupling (and absorption) of light, as these modes show a distinctly different directional emission profile [58, 93]. We have explained these profiles in detail in the previous chapter. However, the range of diameters close to the onset of the transverse guided modes has not been investigated experimentally.

In this chapter we measure the directional emission from nanowires with eight different diameters in the range from 143 to 208 nm, and conclude that the coupling to waveguide modes is very sensitive to the diameter. The width of the Gaussian angular pattern is found to be diameter-dependent, with a minimum width around a diameter of 164 nm. There is an abrupt change in the emission pattern when the nanowire diameter exceeds 171 nm. These measurements illustrate the relevance of carefully tuning the nanowire diameter with nanometer accuracy to optimize device performance.

7.2 SAMPLE AND MEASUREMENT

Our sample consists of square-symmetric arrays of indium phosphide (InP) nanowires, that have been fabricated by sequential axial vapour-liquid-solid (VLS) growth and radial vapour-solid (VS) growth, as has been described in the previous chapter [58, 185]. The nanowires from different arrays exhibit different diameters d, and have the same length of about 7 micron. The nanowires are untapered, although the top and bottom ends (both 1 micron of the length) have a slight tapering. This tapering has no effect on the result, as has been addressed in ref.

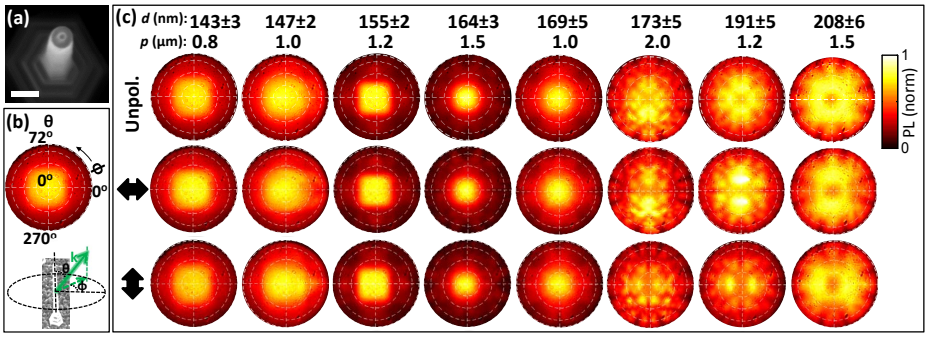

Figure 7.2: Polarized directional emission from nanowires. (a) Scanning electron micrograph of one of the investigated nanowires. The scale bar is 200 nm. (b) Example of an emission pattern and definition of the elevation angle θ (between the long axis of the nanowire and the emission k-vector) and the azimuthal angle ϕ. (c) Emission patterns of nanowires with different diameters. The first row shows the unpolarized emission, and the second (third) row shows the emission polarized horizontal (vertical) with respect to the image. The uncertainties in the diameter denote wire-to-wire differences and the error in the SEM images. p is the period of the nanowire array.

[58]. The nanowires were excited with a 640 nm diode laser under a 100x microscope objective with a numerical aperture of 0.95. A typical photoluminescence spectrum is shown in Figure 7.1 (red, dashed curve), which is blueshifted with respect to the substrate emission (black, solid curve). The nanowires exhibit band gap emission, which points at a predominantly wurtzite crystal structure, other than the substrate, which has a zincblende crystal structure. We investigate the directional emission from the nanowires by Fourier microscopy, described in detail in Chapter 3.

Figure 7.2 shows the directional emission patterns from the eight nanowire arrays that we have measured, accompanied by a scanning electron micrograph of one of them (Figure 7.2a). Figure 7.2b explains the measurement geometry and the coordinates of the emission patterns, while Figure 7.2c shows the measured emission patterns. The first row shows the unpolarized emission patterns, while the second (third) row shows the patterns recorded with the polarizer oriented horizontally (vertically) with respect to the images, as indicated by the double arrows on the left side. A gradual narrowing of the emission pattern is visible when increasing the diameter from 143 to 164 nm, as well as an abrupt change of the pattern around d=171 nm. For larger diameters we observe, instead of a Gaussian-like pattern, a significantly different pattern with a pronounced dip in the center of the images. This 'doughnut-like shape' is modified by the periodic array of nanowires although the azimuthal emission is not significantly changed [58].

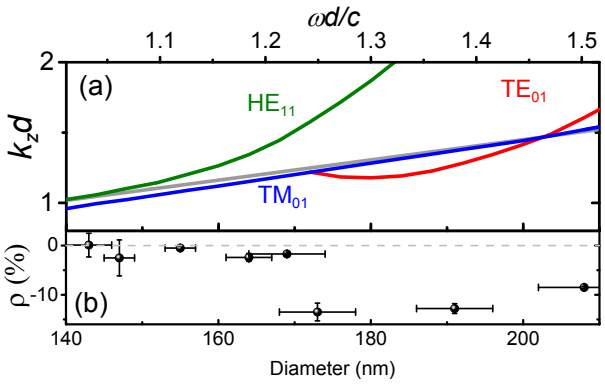

Figure 7.3: Waveguide modes in InP nanowires and polarization anisotropy. (a) Representation of the waveguide mode dispersion i.e. $k_z d$ as a function of $\omega d/c$. The gray line is the light line in air. The corresponding diameters for a fixed emission wavelength of 870 nm (InP refractive index of 3.43) are shown at the bottom horizontal axis (shared with b). (b) Polarization anisotropy $\rho = (I_{\parallel} - I_{\perp})/(I_{\parallel} + I_{\perp})$ as a function of the diameter, determined from Figure 7.2c.

7.3 WAVEGUIDE MODE DISPERSION AND POLARIZATION

Since it is known that the emission pattern is mainly determined by waveguide modes [58, 103], we display the dispersion diagram ($k_z d$ vs. $\omega d/c$) of the relevant waveguide modes in Figure 7.3a. On the bottom horizontal axis we show the diameters for a frequency fixed to the emission frequency of InP, $\omega/c = k_0 = 2\pi/870$ nm, and InP refractive index n_{InP}=3.43. We show also the light line for air (in gray), which defines the boundary between guided modes (above the light line) and leaky modes (below the light line). The leaky modes are similar to the guided modes, but have a complex propagation constant in the direction along the nanowire (with $\mathrm{Re}(k_z) < \omega/c$), which makes them radiate into the far field [135]. In the diameter range of the experiment only the HE_{11}, TM_{01}, and TE_{01} modes are available. The TM_{01} (TE_{01}) mode is leaky for diameters below d=203 nm (between d=172 nm and d=203 nm), and guided for diameters above d=203 nm. Since the TM and TE modes are polarized, the polarization of the emission provides information about the coupling to these waveguide modes. Therefore, we calculate the polarization anisotropy ratio, defined as $\rho = (\overline{I}_{\parallel} - \overline{I}_{\perp})/(\overline{I}_{\parallel} + \overline{I}_{\perp})$, [73, 96] from the angle-integrated emission of each nanowire. In this equation $\overline{I}_{\parallel}$ corresponds to the angle-integrated emission component parallel to the nanowire, whereas $\overline{I}_{\perp}$ is the emission component perpendicular to the nanowire. The polarization analysis of the setup has been described in Section 3.1. ρ is displayed in Figure 7.3b, as a function of the nanowire diameter. We see that ρ remains very close to 0, up to about d=170 nm, where it abruptly becomes negative to a value of about -10%. This negative value indicates a larger perpendicularly polarized emission fraction, pointing at a coupling of the emission to the TE_{01} mode, which becomes

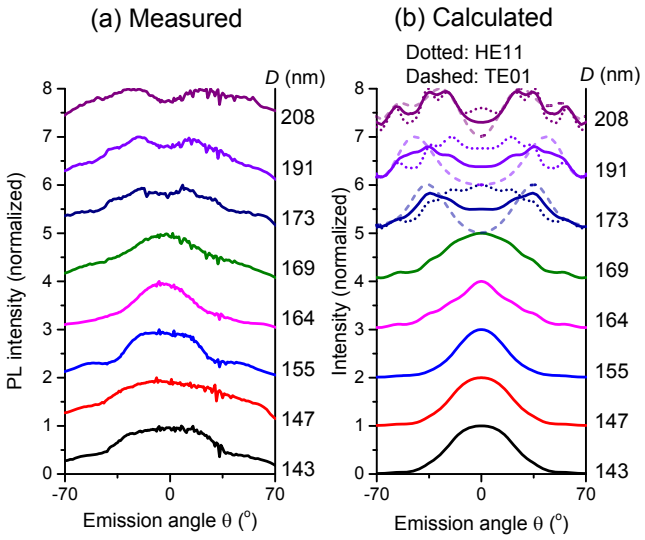

Figure 7.4: Stacked directional emission profiles along $\phi = 0°$. (a) Measured profiles of the normalized directional unpolarised emission profiles (Figure 7.1c, first row). (b) Calculated traces using a 1D analytical model. At diameters smaller than 170 nm, only the HE_{11} mode is supported. At diameters larger than 170 nm both HE_{11} and TE_{01} modes are shown. The dotted lines represent the HE_{11} mode calculations, and the dashed lines represent the TE_{01} mode calculations. The solid line is the average between the two modes.

available (although leaky) around a diameter of 170 nm. We see no signatures of the TM_{01} mode, which can be related to the fact that its dispersion is very close to the light line, or to the (mainly) wurtzite crystal structure of the nanowires. Wurtzite material forbids dipole emission oriented parallel to the nanowire [178, 179], which is needed to couple efficiently to the TM_{01} mode.

Figure 7.4a displays the profiles of the directional emission patterns along $\phi = 0°$. We compare this emission to the calculated emission profiles which correspond to the relevant waveguide modes. These calculated emission profiles were determined using an analytical model [136], which envisions the nanowire as a one dimensional current in a wire of a finite length L excited by a point dipole at a distance z_0 from the nanowire center. The model is described in more detail in Section 2.2. We calculate the emission patterns by fixing the k_z's corresponding to the HE_{11} and TE_{01} modes at each given diameter. These k_z's are determined from the dispersion curves shown in Figure 7.3a.

For d<170 nm only the HE_{11} mode profiles are calculated, and for d>170 nm both the HE_{11} (dotted) and TE_{01} (dashed) modes, as well as an average. We conclude that at d<170 nm the emission can be explained by the HE_{11} mode. At d>170 nm we see a strong emission at θ=0° as well, which also points at coupling of the emission to the HE_{11} mode. However, the features

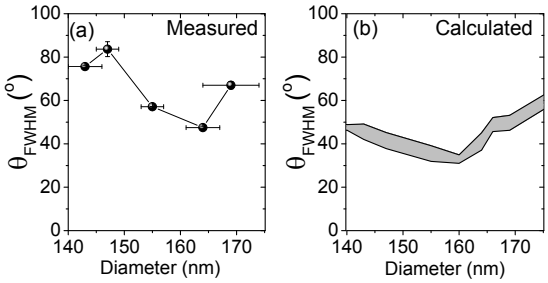

Figure 7.5: FWHM of the directional emission. (a) Measured angular full-with at half maximum (FWHM) of the directional emission profiles that are associated with the HE_{11} mode.(b) Calculated angular FWHM using an analytical model. The shaded area shows the variation for a nanowire length of 6 to 8 micrometers.

at emission angles of $20^\circ < \theta < 40^\circ$ are mainly polarized perpendicular to the nanowire (as can be seen in Figure 7.2c, second and third rows), which can only be explained by emission guided by the TE_{01} mode. Therefore, we conclude that both modes are excited for d >170 nm. The solid lines in Figure 7.4b, which are the average between the profiles of the HE_{11} and TE_{01} modes, show good agreement with the measurement.

7.4 HE_{11} MODE INTERFERENCE

As mentioned before, we observe a gradual transition among the thinner nanowires (d<170 nm), although only a single mode (HE_{11}) is excited in this range. To quantify this transition, we display in Figure 7.5a the full-width at half maximum (FWHM) of the angular profiles shown in Figure 7.4a. We observe a narrowing of the profile when increasing the diameter, finding a minimum θ_{FWHM} of 47° around d=164 nm. The profile broadens for d=169 nm. This broadening cannot be related to coupling to the TE_{01} mode, because this mode is not supported for this diameter. A very similar trend is visible in the calculated θ_{FWHM} from the profiles, which is shown in Figure 7.5b. To account for slight changes of the nanowire length, we show in this figure the results for nanowire lengths between 6 and 8 μm. The calculations were based on a 1D model, with only the parallel component of the mode wave vector (k_z), the source position distribution, and end facet reflectivities as parameters. Of these parameters, only the mode wave vector changes when modifying d. Therefore, we conclude that the behaviour of θ_{FWHM} is controlled only by k_z, thus by the effective mode wavelength λ_{eff} (since $k_z = 2\pi/\lambda_{eff}$). This parameter determines, together with the nanowire length, the interference pattern of the emission from the end facets of the nanowire into the far field, and therefore also the width of the Gaussian-like distribution. Although there is a reasonably good qualitative agreement between the measurements and the analytical model, there are significant quantitative

discrepancies. These discrepancies can be attributed to the simplicity of the 1D model and the presence of the substrate in the measurements, which introduces an additional reflection at the bottom interface. Additionally, the increased θ_{FWHM} in the thinnest measured nanowires might be caused by scattering due to the surrounding nanowires, because the period is smaller for these arrays.

7.5 CONCLUSION

In conclusion, we have shown that a change in nanowire diameter of only a few nanometers may induce an abrupt change in the emission pattern and polarization. This change is related to the onset of the TE_{01} leaky mode, to which the emission can couple. Also, we have found that the width of the emission pattern of the HE_{11} mode is strongly diameter-dependent, with a minimum width around d=164 nm. This is caused by the interference of light which couples out at the end facets of the nanowire. This work provides important guidelines for the design for quantum emitters, LEDs and photovoltaic devices based on semiconductor nanowires.

8

HIGH REFRACTIVE INDEX OF WURTZITE GAP MEASURED FROM NANOWIRE FABRY-PÉROT RESONANCES

In this chapter, we investigate the optical emission of wurtzite GaP/$Al_{0.4}Ga_{0.6}P$ core/shell nanowires (NWs) transferred on a SiO_x substrate. We demonstrate a high degree of waveguiding of the emitted photoluminescence (PL) signal. By analysing the Fabry-Pérot mode spacing in combination with calculations of the guided modes in the NWs, we determine a very high refractive index of bulk WZ GaP of 4.2 at a wavelength of 600 nm. The measured quality factors up to 600 indicate the excellent optical quality of the nanowire resonator.[1]

8.1 INTRODUCTION WURTZITE GAP NANOWIRES

Semiconductor nanowires (NWs) offer unique features such as the possibility to switch the crystal phase from zinc blende (ZB) into wurtzite (WZ) [186, 187]. The resulting change in the atomic stacking sequence has a strong effect on the electronic band structure, with an indirect to direct band gap transition in materials such as gallium phosphide [188], providing an enhanced light absorption that results in a strong efficiency increase in solar water splitting devices [189]. Recent photoluminescence (PL) studies on WZ GaP NWs provided a deeper understanding on the band gap and excitonic emission in this material system [190, 191]. However, additional knowledge on the WZ GaP parameters such as the refractive index would be beneficial for the design of opto-electrical devices based on WZ GaP.

In this chapter, we report a novel method to estimate the refractive index for materials which are available only in the nanowire geometry. From the Fabry-Pérot resonances observed in micro-photoluminescence (PL) measurements on a single WZ GaP/$Al_{0.4}Ga_{0.6}P$ core/shell nanowire we extract an effective refractive index of n_{WZ}^{EFF} = 3.8 at 600 nm. We assign the HE_{11} fundamental mode as the guided mode in the nanowires, from which we estimate the refractive index of bulk WZ GaP to be n_{WZ} = 4.2 at a wavelength of 600 nm. The presence of the wurtzite crystal structure results in one of the highest values for the refractive index in the visible part of the spectrum, among the III-V semiconductors.

1 This chapter is based on: S. Assali*, D. van Dam*, J.E.M. Haverkort, and E.P.A.M. Bakkers, "High refractive index in wurtzite GAP measured from Fabry-Pérot resonances", *Appl. Phys. Lett.* 108, 173101 (2016). * equal contribution.

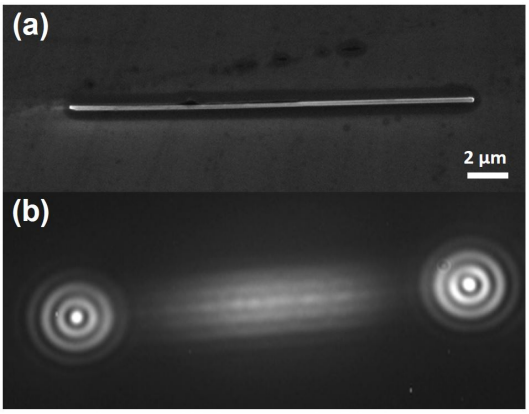

Figure 8.1: (a) SEM image of a WZ GaP/$Al_{0.4}Ga_{0.6}P$ core/shell nanowire of approximately 220 nm diameter and 18.5 μm length transferred on SiO_x. The gold droplet is visible at the right end facet of the wire. (b) PL image of the nanowire showing two bright emission spots at the end facets.

8.2 SAMPLE DESCRIPTION

The nanowires used in this work were grown according to the recipe provided in earlier publications [190, 191], resulting in WZ GaP/$Al_{0.4}Ga_{0.6}P$ core/shell NWs with lengths above 6 μm and diameters of approximately 220 nm. For micro-PL measurements, the NWs were transferred to a thermally oxidized Si wafer with gold markers, and cooled down to 4 Kelvin. The optical data were collected in backscattering geometry using a NA=0.7 Nikon 50x CR objective, and a 0.30 m spectrometer equipped with 1200 g/mm grating (500 nm blazing angle). A 405 nm CW-laser was used for the excitation in combination with a f=500 mm cylindrical lens, resulting in a rectangular spot of around 1 μm x 10 μm at the sample, while the PL images were collected with a Watec CCD camera. After optical measurements, the NWs were studied by scanning electron microscopy (SEM) to determine the wire length and diameter. The SEM image in Figure 8.1a shows a WZ GaP/$Al_{0.4}Ga_{0.6}P$ core/shell nanowire with core diameter of 200 nm and shell thickness of 10-15 nm. The length is L = 18.5 μm and the nanowire is transferred onto a SiO_x substrate. Under laser excitation the PL image in Figure 8.1b is obtained where two bright emission spots are visible at the two ends of the nanowire, which indicate that the nanowire act as a transparent waveguide for the emitted photoluminescence [192–194].

8.3 EFFECTIVE MODE INDEX

Strong modulation in the PL spectra of the nanowires due to the Fabry-Pérot (FP) resonances as a result of the multiple reflections between the wire's end facets [195] are shown in Figure 8.2a. The presence of the $Al_{0.4}Ga_{0.6}P$ shell strongly enhances the FP modes in the cavity,

reaching quality factors Q in the range 100-600, as shown by the comparison with a WZ GaP nanowire (black curve in Figure 8.2a). The mode spacing $\Delta\lambda$ reduces for increasing wire length L and increases with the emission wavelength λ, as shown in the data set covering 11 different nanowires in Figure 8.2b. The typical FP-dependence $\Delta\lambda = \frac{1}{L}\frac{\lambda^2}{n_G}$, with the group index n_G being related to the mode index n_E of the nanowire waveguide mode through $n_G = n_E - \lambda\frac{dn_E}{d\lambda}$ [196], is shown in the inset in Figure 8.2b.

In case that the dispersion relation for n_E is known, the mode spacing in the FP cavity could provide information on the mode index n_E of the WZ GaP. The Sellmeier equation [192, 197] can be used to give an approximate dispersion relation for n_E:

$$n_E^2 = A + B\frac{\lambda^2}{\lambda^2 - C} \tag{8.1}$$

where A, B and C are the Sellmeier coefficients. By fitting the mode spacing $\Delta\lambda$ as a function of the wavelength λ using the Sellmeier equation, we can estimate the mode index n_E for WZ GaP wires. In Figure 8.3 the measured values for n_E of the WZ GaP wires as a function of the wavelength are shown (blue spheres), together with the refractive index for the ZB GaP bulk (red curve). The error bars are derived from the fit on the set of 11 wires studied. Values of the mode index n_E for the WZ wires are found to be ranging from 3.6 to 4.0. However, the measured value for the mode index of the WZ wires is only a lower limit for the actual bulk refractive index. The measured mode index corresponds to the waveguide mode in the wires to which the emission has coupled. However, this mode is not fully confined inside the nanowire, but also extends partially into the surrounding air [98] while also the AlGaP shell may reduce n_E, as will be discussed later. Depending on the specific mode excited in the wire, the mode index changes, with values always lower than the refractive index of the bulk material [198].

8.4 BULK INDEX OF WURTZITE GAP

From the measured effective mode index we can estimate the value of the bulk index for WZ GaP. We use the transcendental equation for waveguide modes supported by a cylinder with radius a [134]:

$$\left(\frac{\mu_1}{u}\frac{J_m'(u)}{J_m(u)} - \frac{\mu_2}{v}\frac{H_m'(v)}{H_m(v)}\right)\left(\frac{(2\pi n_1/\lambda)^2}{\mu_1 u}\frac{J_m'(u)}{J_m(u)} - \frac{(2\pi n_2/\lambda)^2}{\mu_2 v}\frac{H_m'(v)}{H_m(v)}\right) = m^2 n_E^2\left(\frac{1}{v^2} - \frac{1}{u^2}\right)^2, \tag{8.2}$$

where λ is the vacuum wavelength, n_E is the mode index, and n_1, n_2, u, v and μ_1, μ_2 are the material refractive indices, the mode parameters and magnetic permeabilities of the nanowire and the surrounding, respectively. J_m and H_m are the Bessel and Hankel functions of the first kind. The mode parameters are defined as $u^2 = a^2((2\pi n_1/\lambda)^2 - n_E^2)$ and $v^2 = a^2((2\pi n_2/\lambda)^2 - n_E^2)$. The integer m denotes the mode order. The solutions to this equation are the hybrid electric modes HE_{ml}, the transverse electric TE_{0l}, and transverse magnetic TM_{0l}

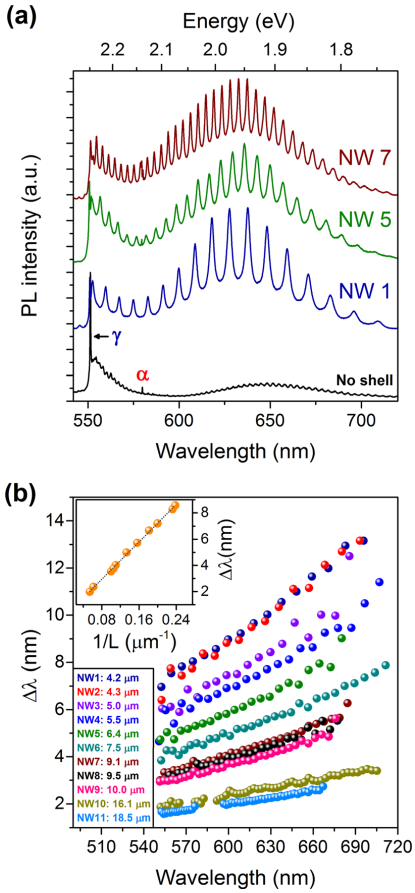

Figure 8.2: (a) PL spectra of three WZ GaP/$Al_{0.4}Ga_{0.6}P$ core/shell nanowires measured at 4K with different lengths showing a change in the FP modes spacing. The black curve refers to a WZ GaP nanowire. (b) Plot of the FP modes spacing as a function of the emission wavelength for 11 nanowires with different lengths. Inset: plot of the FP modes spacing as a function of $1/L$.

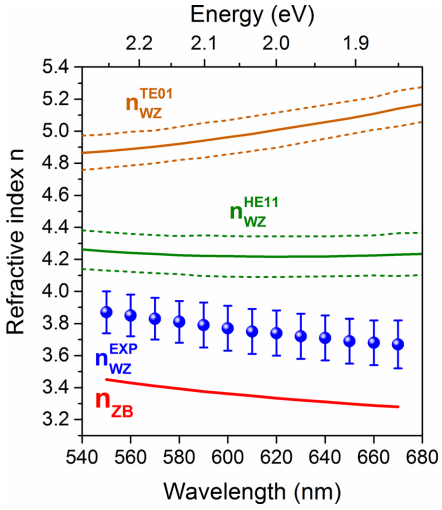

Figure 8.3: Plot of the refractive index n as a function of wavelength at T=4K. The measured refractive index of $Al_{0.4}Ga_{0.6}P$ core/shell nanowires is labelled as n_{WZ}^{EXP}, while the bulk WZ GaP refractive index estimated under the assumption of relevant HE_{11} or TE_{01} modes are labelled as n_{WZ}^{HE11} and n_{WZ}^{TE01}, respectively. The dashed curves indicate the error in the obtained index, which is defined by the error in the measured n. The red curve indicates the refractive index n_{ZB} of bulk ZB GaP at T=300K.

modes, where l is the order of the solution. For each measured $n_E(\lambda)$ we fit the given equation numerically, assuming the surrounding to be vacuum and using the bulk refractive index n_1 as a fitting parameter. For the fundamental HE_{11} mode, the electric field is tightly confined in the nanowire, having a maximum field in the nanowire's center and an electric field polarized perpendicular to the nanowire, allowing for efficient coupling with the emitting dipoles due to the wurtzite selection rules [178]. The next tightly confined mode is the TE_{01} mode with a field intensity equal to zero along the nanowire axis and thus limited spatial overlap with emitting dipoles close to the nanowire's center. In Figure 8.3 the bulk refractive indices of WZ GaP are plotted considering either the HE_{11} or the TE_{01} as the excited mode. If we would assume the TE_{01} to be the excited mode, the bulk refractive index would decrease with energy below the band gap, which would be unprecedented for bulk materials. Similar considerations hold for higher order excited modes. The overlap with the emitting dipoles (located in the core) is also larger for the HE_{11} mode than the TE_{01} mode. Therefore, we conclude that the fundamental HE_{11} mode is most probably excited in the WZ GaP nanowires under study. Under this assumption, the deduced refractive index of bulk WZ GaP at 4K ranges between 4.1-4.4 in the visible wavelength range as shown in Figure 8.3.

The large difference in refractive index induced by the change in crystalline structure is remarkable, with an increase from n_{ZB} = 3.4 to n_{WZ} = 4.2 at 600 nm. By considering the temperature dependence of the refractive index [18, 199], the 4K value of the refractive index of ZB GaP is $n_{ZB}^{4K} \approx 3.3$ at 600 nm, providing an even larger difference with the WZ value. In addition, we note that the presence of the $Al_{0.4}Ga_{0.6}P$ shell slightly reduces the measured refractive index of WZ GaP ($n_{ZB}^{Al_{0.4}Ga_{0.6}P}$= 3.24, while n_{ZB}^{GaP}= 3.37 at 600 nm) [200], therefore the derived bulk refractive index represents only a lower limit. The high refractive index of WZ GaP suggests the availability of many different waveguide modes even for small nanowire radii, which is due to the strong confinement enabled by the high refractive index. Finally, we should mention that recently, a lower refractive index for WZ GaP nanowires with respect to ZB bulk was indirectly estimated from reflection measurements in the UV range [201], leading to a similar behaviour in the visible range due to the positive sign of $\frac{dn_E}{d\lambda}$. However, a value for the WZ refractive index smaller the ZB refractive index does not match with the experimentally observed FP mode spacing in the present work. The origin of the discrepancy is not clear; additional measurements on a wider wavelength range may clarify this.

8.5 CONCLUSION

The very high value for the refractive index of 4.1-4.4 for WZ GaP in the visible wavelength range demonstrated in this work is to the best of our knowledge the highest value among other III-V semiconductor materials. Additionally, we measure high values for the quality factor of the Fabry-Perot resonances of up to 600. These properties would make WZ GaP a beneficial mate-

rial for opto-electronic applications, enhancing light confinement and absorption, which can provide higher efficiency nanowire-based (multi-junction) solar cells [85], photoelectrochemical cells [155, 189], and photodetectors [142, 202]. In addition, the transparency of WZ GaP for wavelengths above 569 nm combined with the extremely high value of the refractive index may provide applications as a 1D optical metamaterial [45, 203, 204], where a control of the optical path of the light without absorption is required.

BIBLIOGRAPHY

[1] J. Fourier. Mémoire sur les temperatures du globe terrestre et des espaces planetaires. *Mémoires de l'Académie Royale des Sciences de l'Institut de France*, VII, 570–604, 1827. (Cited on page 1.)

[2] S. Arrhenius. On the Influence of Carbonic Acid in the Air upon the Temperature of the Ground. *Phylosophical Magazine and Journal of Science*, 41, 237–276, 1896. (Cited on page 1.)

[3] Wikipedia. Alexander Graham Bell. (Cited on page 1.)

[4] J. S. Sawyer. Man-made Carbon Dioxide and the "Greenhouse" Effect. *Nature*, 239(5366), 23–26, 1972. (Cited on page 1.)

[5] W. R. L. Anderegg, J. W. Prall, J. Harold, and S. H. Schneider. Expert credibility in climate change. *Proceedings of the National Academy of Sciences*, 107(27), 12107–12109, 2010. (Cited on page 1.)

[6] J. Cook, D. Nuccitelli, S. A. Green, M. Richardson, B. Winkler, R. Painting, R. Way, P. Jacobs, and A. Skuce. Quantifying the consensus on anthropogenic global warming in the scientific literature. *Environmental Research Letters*, 8(2), 024024, 2013. (Cited on page 1.)

[7] D. J. C. MacKay. *Sustainable Energy — without the hot air*, volume 78. 2009. (Cited on page 2.)

[8] Wikipedia. Growth of photovoltaics. (Cited on pages 2 and 3.)

[9] SolarGIS maps: www.solarGIS.info. (Cited on page 3.)

[10] E. Becquerel. Mémoire sur les effets électriques produits sous l'influence des rayons solaires. *Comptes Rendus*, 9, 561–567, 1839. (Cited on page 3.)

[11] C. E. Fritts. On a New Form of Selenium Photocell. *American Journal of Science*, 26, 465, 1883. (Cited on page 3.)

[12] R. Ohl. Light-sensitive electric device. *US Patent*, 2, 402,662, 1946. (Cited on page 3.)

[13] D. M. Chapin, C. S. Fuller, and G. L. Pearson. A new silicon p-n junction photocell for converting solar radiation into electrical power. *Journal of Applied Physics*, 25(5), 676–677, 1954. (Cited on page 3.)

[14] M. A. Green, K. Emery, Y. Hishikawa, W. Warta, and E. D. Dunlop. Solar cell efficiency tables (version 46). *Progress in Photovoltaics: Research and Applications*, 23, 805–812, 2015. (Cited on pages 4, 6, and 51.)

[15] M. A. Green. Third generation photovoltaics: Ultra-high conversion efficiency at low cost. *Progress in Photovoltaics: Research and Applications*, 9(2), 123–135, mar 2001. (Cited on page 4.)

[16] ASTM reference spectrum: http://rredc.nrel.gov/solar/spectra/am1.5/. (Cited on page 5.)

[17] W. Shockley and H. J. Queisser. Detailed Balance Limit of Efficiency of p-n Junction Solar Cells. *Journal of Applied Physics*, 32(3), 510, 1961. (Cited on pages 5, 19, and 43.)

[18] Ioffe Physical-Technical Institute of the Russian Academy of Sciences. Semiconductors database: http://www.ioffe.ru/SVA/NSM/Semicond/. (Cited on pages 6 and 92.)

[19] Jefferson Lab at US department of Energy. The Periodic Table of Elements: http://education.jlab.org/itselemental/index.html. (Cited on page 6.)

[20] H. Savin, P. Repo, G. von Gastrow, P. Ortega, E. Calle, M. Garín, and R. Alcubilla. Black silicon solar cells with interdigitated back-contacts achieve 22.1% efficiency. *Nature Nanotechnology*, 10(May), 1–6, 2015. (Cited on pages 6 and 56.)

[21] S. L. Diedenhofen, O. T. A. Janssen, G. Grzela, E. P. A. M. Bakkers, and J. Gómez Rivas. Strong geometrical dependence of the absorption of light in arrays of semiconductor nanowires. *ACS Nano*, 5(3), 2316–2323, 2011. (Cited on pages 15, 44, 46, 54, 55, and 56.)

[22] N. Anttu. Shockley-Queisser Detailed Balance Efficiency Limit for Nanowire Solar Cells. *ACS Photonics*, 2(3), 446–453, 2015. (Cited on pages 6, 51, and 55.)

[23] R. A. Gaiser and M. F. Schaible. Method to produce low light reflecting films on glass surfaces. *US Patent*, 2, 490,263, 1949. (Cited on page 6.)

[24] W. H. Southwell. Gradient-index antireflection coatings. *Optics Letters*, 8(11), 584–586, 1983. (Not cited.)

[25] Y. J. Lee, D. S. Ruby, D. W. Peters, B. B. McKenzie, and J. W. P. Hsu. ZnO nanostructures as efficient antireflection layers in solar cells. *Nano Letters*, 8(5), 1501–1505, 2008. (Cited on page 6.)

[26] E. Yablonovitch. Statistical ray optics. *Journal of the Optical Society of America*, 72(7), 899, 1982. (Cited on pages 6, 43, and 55.)

[27] P. Campbell and M. A. Green. Light trapping properties of pyramidally textured surfaces. *Journal of Applied Physics*, 62(1), 243–249, 1987. (Cited on page 43.)

[28] K. X. Wang, Z. Yu, V. Liu, Y. Cui, and S. Fan. Absorption enhancement in ultrathin crystalline silicon solar cells with antireflection and light-trapping nanocone gratings. *Nano Letters*, 12(3), 1616–1619, 2012. (Cited on pages 6 and 7.)

[29] K. R. Catchpole and A. Polman. Design principles for particle plasmon enhanced solar cells. *Applied Physics Letters*, 93(19), 191113, 2008. (Cited on page 6.)

[30] S. L. Diedenhofen, G. Vecchi, R. E. Algra, A. Hartsuiker, O. L. Muskens, G. G. W. Immink, E. P. A. M. Bakkers, W. L. Vos, and J. Gómez Rivas. Broad-band and omnidirectional antireflection coatings based on semiconductor nanorods. *Advanced Materials*, 21(9), 973–978, mar 2009. (Not cited.)

[31] V. E. Ferry, J. N. Munday, and H. A. Atwater. Design considerations for plasmonic photovoltaics. *Advanced Materials*, 22(43), 4794–4808, nov 2010. (Not cited.)

[32] V. E. Ferry, M. A. Verschuuren, H. B. T. Li, E. Verhagen, R. J. Walters, R. E. I. Schropp, H. A. Atwater, and A. Polman. Light trapping in ultrathin plasmonic solar cells. *Optics Express*, 18(S2), A237–A245, 2010. (Not cited.)

[33] H. A. Atwater and A. Polman. Plasmonics for improved photovoltaic devices. *Nature Materials*, 9(3), 865, mar 2010. (Cited on page 7.)

[34] P. Spinelli, M. A. Verschuuren, and A. Polman. Broadband omnidirectional antireflection coating based on subwavelength surface Mie resonators. *Nature Communications*, 3, 692, jan 2012. (Cited on pages 6 and 55.)

[35] M. D. Kelzenberg, S. W. Boettcher, J. A. Petykiewicz, D. B. Turner-Evans, M. C. Putnam, E. L. Warren, J. M. Spurgeon, R. M. Briggs, N. S. Lewis, and H. A. Atwater. Enhanced absorption and carrier collection in Si wire arrays for photovoltaic applications. *Nature Materials*, 9(3), 239–244, mar 2010. (Cited on page 6.)

[36] L. Tsakalakos, J. Balch, J. Fronheiser, M.-Y. Shih, S. F. LeBoeuf, M. Pietrzykowski, P. J. Codella, B. A. Korevaar, O. V. Sulima, J. Rand, A. Davuluru, and U. Rapol. Strong broadband optical absorption in silicon nanowire films. *Journal of Nanophotonics*, 1(1), 013552, jul 2007. (Not cited.)

[37] E. C. Garnett and P. Yang. Light trapping in silicon nanowire solar cells. *Nano Letters*, 10(3), 1082–1087, mar 2010. (Cited on pages 13 and 43.)

[38] Y. Kuang, M. C. V. Lare, L. W. Veldhuizen, A. Polman, J. K. Rath, and R. E. I. Schropp. Efficient nanorod-based amorphous silicon solar cells with advanced light trapping. *Journal of Applied Physics*, 118(18), 2015. (Cited on page 6.)

[39] Z. Fan, R. Kapadia, P. W. Leu, X. Zhang, Y.-l. Chueh, K. Takei, K. Yu, A. Jamshidi, A. A. Rathore, D. J. Ruebusch, M. Wu, and A. Javey. Ordered Arrays of Dual-Diameter Nanopillars for Maximized Optical Absorption. *Nano Letters*, 10, 3823–3827, 2010. (Cited on page 6.)

[40] J. Zhu, Z. Yu, G. F. Burkhard, C.-M. Hsu, S. T. Connor, Y. Xu, Q. Wang, M. D. McGehee, S. Fan, and Y. Cui. Optical absorption enhancement in amorphous silicon nanowire and nanocone arrays. *Nano Letters*, 9(1), 279–282, 2009. (Cited on pages 6, 43, 46, 51, 54, 55, and 56.)

[41] B. Wang and P. W. Leu. Tunable and selective resonant absorption in vertical nanowires. *Optics Letters*, 37(18), 3756–3758, 2012. (Cited on pages 6, 12, and 14.)

[42] J. Zhu, C.-M. Hsu, Z. Yu, S. Fan, and Y. Cui. Nanodome solar cells with efficient light management and self-cleaning. *Nano Letters*, 10(6), 1979–1984, jun 2010. (Cited on page 6.)

[43] Y.-F. Huang, S. Chattopadhyay, Y.-J. Jen, C.-Y. Peng, T.-A. Liu, Y.-K. Hsu, C.-L. Pan, H.-C. Lo, C.-H. Hsu, Y.-H. Chang, C.-S. Lee, K.-H. Chen, and L.-C. Chen. Improved broadband and quasi-omnidirectional anti-reflection properties with biomimetic silicon nanostructures. *Nature Nanotechnology*, 2(12), 770–774, 2007. (Cited on pages 6, 46, and 55.)

[44] M. L. Brongersma, Y. Cui, and S. Fan. Light management for photovoltaics using high-index nanostructures. *Nature Materials*, 13(5), 451–60, apr 2014. (Cited on pages 6 and 43.)

[45] O. L. Muskens, J. Gómez Rivas, R. E. Algra, E. P. A. M. Bakkers, and A. Lagendijk. Design of Light Scattering in Nanowire Materials for Photovoltaic Applications. *Nano Letters*, 8(9), 2638–2642, 2008. (Cited on pages 7 and 93.)

[46] M. A. Green. Radiative efficiency of state-of-the-art photovoltaic cells. *Progress in Photovoltaics: Research and Applications*, 20(1), 472–476, 2012. (Cited on page 7.)

[47] O. D. Miller, E. Yablonovitch, and S. R. Kurtz. Strong Internal and External Luminescence as Solar Cells Approach the Shockley-Queisser Limit. *IEEE Journal of Photovoltaics*, 2(3), 303–311, jul 2012. (Cited on pages 7, 23, and 44.)

[48] R. T. Ross. Thermodynamic Limitations on the Conversion of Radiant Energy into Work. *The Journal of Chemical Physics*, 45(1), 1–7, 1966. (Cited on page 8.)

[49] C. H. Henry. Limiting efficiencies of ideal single and multiple energy gap terrestrial solar cells. *Journal of Applied Physics*, 51(1980), 4494–4500, 1980. (Not cited.)

[50] A. Martí, J. L. Balenzategui, and R. Reyna. Photon recycling and Shockley's diode equation. *Journal of Applied Physics*, 82(8), 4067–4075, 1997. (Cited on pages 8 and 65.)

[51] P. Würfel. Physics of Solar Cells - From Principles to New Concepts, 2005. (Cited on pages 20, 38, and 43.)

[52] U. Rau, U. W. Paetzold, and T. Kirchartz. Thermodynamics of light management in photovoltaic devices. *Physical Review B*, 90, 035211, 2014. (Cited on pages 8, 19, 21, 23, and 79.)

[53] L. C. Hirst and N. J. Ekins-Daukes. Fundamental losses in solar cells. *Progress in Photovoltaics*, 19(August 2010), 286–293, 2011. (Cited on pages 8, 19, 21, and 23.)

[54] G. L. Araújo and A. Martí. Absolute limiting efficiencies for photovoltaic energy conversion. *Solar Energy Materials and Solar Cells*, 33, 213–240, 1994. (Cited on pages 8 and 79.)

[55] E. D. Kosten, J. H. Atwater, J. Parsons, A. Polman, and H. A. Atwater. Highly efficient GaAs solar cells by limiting light emission angle. *Light: Science & Applications*, 2(1), e45, jan 2013. (Cited on pages 8, 43, 65, and 79.)

[56] E. D. Kosten, B. M. Kayes, and H. A. Atwater. Experimental demonstration of enhanced photon recycling in angle-restricted GaAs solar cells. *Energy & Environmental Science*, 7(6), 1907, 2014. (Cited on page 8.)

[57] A. Braun, E. A. Katz, D. Feuermann, B. M. Kayes, and J. M. Gordon. Photovoltaic performance enhancement by external recycling of photon emission. *Energy & Environmental Science*, 6(5), 1499, 2013. (Cited on page 8.)

[58] D. van Dam, D. R. Abujetas, R. Paniagua-Domínguez, J. A. Sánchez-Gil, E. P. A. M. Bakkers, J. E. M. Haverkort, and J. Gómez Rivas. Directional and Polarized Emission from Nanowire Arrays. *Nano Letters*, 15(7), 4557–4563, 2015. (Cited on pages 8, 16, 50, 71, 79, 80, 81, and 82.)

[59] D. van Dam, D. R. Abujetas, J. A. Sánchez-Gil, J. E. M. Haverkort, E. P. A. M. Bakkers, and J. Gómez Rivas. Strong diameter-dependence of nanowire emission coupled to waveguide modes. *Applied Physics Letters*, 108, 121109, 2016. (Cited on pages 8 and 16.)

[60] R. S. Wagner and W. C. Ellis. Vapor-Liquid-Solid Mechanism of Single Crystal Growth. *Applied Physics Letters*, 4(5), 89, 1964. (Cited on page 9.)

[61] M. T. Borgström, J. Wallentin, J. Trägårdh, P. Ramvall, M. Ek, L. Reine, L. Samuelson, and K. Deppert. In Situ Etching for Total Control Over Axial and Radial Nanowire Growth. *Nano Research*, 3, 264–270, 2010. (Cited on pages 10 and 15.)

[62] J. H. Woodruff, J. B. Ratchford, I. A. Goldthorpe, P. C. Mcintyre, and C. E. D. Chidsey. Vertically Oriented Germanium Nanowires Grown from Gold Colloids on Silicon Substrates and Subsequent Gold Removal. *Nano Letters*, 7(6), 1637–1642, 2007. (Cited on page 10.)

[63] J. Motohisa, J. Takeda, M. Inari, J. Noborisaka, and T. Fukui. Growth of GaAs/AlGaAs hexagonal pillars on GaAs (1 1 1)B surfaces by selective-area MOVPE. *Physica E: Low-Dimensional Systems and Nanostructures*, 23(3-4 SPEC. ISS.), 298–304, 2004. (Cited on page 10.)

[64] J. Motohisa, J. Noborisaka, J. Takeda, M. Inari, and T. Fukui. Catalyst-free selective-area MOVPE of semiconductor nanowires on (111)B oriented substrates. *Journal of Crystal Growth*, 272(1-4 SPEC. ISS.), 180–185, 2004. (Cited on page 10.)

[65] Q. Gao, D. Saxena, F. Wang, L. Fu, S. Mokkapati, Y. Guo, L. Li, J. Wong-Leung, P. Caroff, H. H. Tan, and C. Jagadish. Selective-Area Epitaxy of Pure Wurtzite InP Nanowires: High Quantum Efficiency and Room-Temperature Lasing. *Nano Letters*, 14, 5206–5211, 2014. (Cited on pages 10 and 53.)

[66] F. Glas. Critical dimensions for the plastic relaxation of strained axial heterostructures in free-standing nanowires. *Physical Review B*, 74(121302(R)), 1–4, 2006. (Cited on pages 11 and 12.)

[67] M. Hocevar, G. G. W. Immink, M. A. Verheijen, N. Akopian, V. Zwiller, L. P. Kouwenhoven, and E. P. A. M. Bakkers. Growth and optical properties of axial hybrid III-V / silicon nanowires. *Nature Communications*, 3, 1266, 2012. (Cited on pages 11 and 12.)

[68] K. Haraguchi, T. Katsuyama, K. Hiruma, and K. Ogawa. GaAs p-n junction formed in quantum wire crystals. *Applied Physics Letters*, 60(6), 745–747, 1992. (Cited on pages 11, 12, and 79.)

[69] K. Haraguchi, T. Katsuyama, and K. Hiruma. Polarization dependence of light emitted from GaAs p-n junctions in quantum wire crystals. *Journal of Applied Physics*, 75(8), 4220, 1994. (Cited on page 11.)

[70] J. C. Johnson, H. Yan, R. D. Schaller, L. H. Haber, R. J. Saykally, and P. Yang. Single Nanowire Lasers. *The Journal of Physical Chemistry B*, 105(46), 11387–11390, nov 2001. (Cited on pages 11 and 14.)

[71] M. H. Huang, S. Mao, H. Feick, H. Yan, Y. Wu, H. Kind, E. Weber, R. Russo, and P. Yang. Room-temperature ultraviolet nanowire nanolasers. *Science*, 292(5523), 1897–9, jun 2001. (Cited on pages 11, 14, and 65.)

[72] X. Duan, Y. Huang, Y. Cui, J. Wang, and C. M. Lieber. Indium phosphide nanowires as building blocks for nanoscale electronic and optoelectronic devices. *Nature*, 409(6816),

66–9, jan 2001. (Cited on page 11.)

[73] J. Wang, M. S. Gudiksen, X. Duan, Y. Cui, and C. M. Lieber. Highly polarized photoluminescence and photodetection from single indium phosphide nanowires. *Science*, 293(5534), 1455–7, aug 2001. (Cited on pages 11, 14, 66, 72, 73, 74, and 82.)

[74] M. T. Björk, B. J. Ohlsson, T. Sass, A. I. Persson, C. Thelander, M. H. Magnusson, K. Deppert, L. R. Wallenberg, and L. Samuelson. One-dimensional Steeplechase for Electrons Realized. *Nano Letters*, 2(2), 87–89, feb 2002. (Cited on page 11.)

[75] M. S. Gudiksen, L. J. Lauhon, J. Wang, D. C. Smith, and C. M. Lieber. Growth of nanowire superlattice structures for nanoscale photonics and electronics. *Nature*, 415(February), 617–620, 2002. (Cited on page 11.)

[76] N. Panev, A. I. Persson, N. Sköld, and L. Samuelson. Sharp exciton emission from single InAs quantum dots in GaAs nanowires. *Applied Physics Letters*, 83(11), 2238–2240, 2003. (Cited on pages 11 and 79.)

[77] M. T. Borgström, V. Zwiller, E. Müller, and A. Imamoglu. Optically bright quantum dots in single nanowires. *Nano Letters*, 5(7), 1439–1443, 2005. (Cited on page 11.)

[78] K. Peng, Y. Xu, Y. Wu, Y. Yan, S. T. Lee, and J. Zhu. Aligned single-crystalline Si nanowire arrays for photovoltaic applications. *Small*, 1(11), 1062–1067, 2005. (Cited on pages 11 and 79.)

[79] N. Anttu and H. Q. Xu. Coupling of light into nanowire arrays and subsequent absorption. *Journal of Nanoscience and Nanotechnology*, 10(11), 7183–7187, nov 2010. (Cited on pages 12, 14, and 56.)

[80] G. Grzela, R. Paniagua-Domínguez, T. Barten, D. van Dam, J. A. Sánchez-Gil, and J. Gómez Rivas. Nanowire Antenna Absorption Probed with Time-Reversed Fourier Microscopy. *Nano Letters*, 14(6), 3227–3234, may 2014. (Cited on pages 12, 14, 27, 28, 37, 56, and 79.)

[81] P. Krogstrup, H. I. Jørgensen, M. Heiss, O. Demichel, J. V. Holm, M. Aagesen, J. Nygård, and A. Fontcuberta i Morral. Single-nanowire solar cells beyond the Shockley-Queisser limit. *Nature Photonics*, 7(4), 306–310, mar 2013. (Cited on pages 12, 43, and 44.)

[82] Y. Wu, H. Yan, and P. Yang. Semiconductor nanowire array: potential substrates for photocatalysis and photovoltaics. *Topics in Catalysis*, 19(2), 197–202, 2002. (Cited on page 12.)

[83] L. Tsakalakos, J. Balch, J. Fronheiser, B. A. Korevaar, O. V. Sulima, and J. Rand. Silicon nanowire solar cells. *Applied Physics Letters*, 91(23), 233117, 2007. (Cited on pages 12 and 13.)

[84] T. Fukui, M. Yoshimura, E. Nakai, and K. Tomioka. Position-controlled III-V compound semiconductor nanowire solar cells by selective-area metal-organic vapor phase epitaxy. *Ambio*, 41 Suppl 2(Supplement 2), 119–24, jan 2012. (Cited on page 13.)

[85] J. Wallentin, N. Anttu, D. Asoli, M. Huffman, I. Åberg, M. H. Magnusson, G. Siefer, P. Fuss-Kailuweit, F. Dimroth, B. Witzigmann, H. Q. Xu, L. Samuelson, K. Deppert, and M. T. Borgström. InP Nanowire Array Solar Cell Achieving 13.8% Efficiency by Exceeding the

Ray Optics Limit. *Science*, 339(6123), 1057–1060, oct 2013. (Cited on pages 13, 45, 55, 79, and 93.)

[86] G. Mariani, A. C. Scofield, C.-H. Hung, and D. L. Huffaker. GaAs nanopillar-array solar cells employing in situ surface passivation. *Nature Communications*, 4, 1497, jan 2013. (Cited on pages 13, 51, and 54.)

[87] Y. Cui, J. Wang, S. R. Plissard, A. Cavalli, T. T. T. Vu, R. P. J. van Veldhoven, L. Gao, M. Trainor, M. A. Verheijen, J. E. M. Haverkort, and E. P. A. M. Bakkers. Efficiency enhancement of InP nanowire solar cells by surface cleaning. *Nano Letters*, 13(9), 4113–7, oct 2013. (Cited on pages 13 and 50.)

[88] O. Isabella, R. Vismara, A. Ingenito, F. T. Si, and M. Zeman. Radial heterojunction c-Si nanowire solar cells with 11.8% conversion efficiency. *Light, Energy and the Environment, OSA Technical Digest (online)*, pages 3–5, 2014. (Cited on page 13.)

[89] I. Åberg, G. Vescovi, D. Asoli, U. Naseem, J. P. Gilboy, C. Sundvall, A. Dahlgren, K. E. Svensson, N. Anttu, M. T. Björk, and L. Samuelson. A GaAs Nanowire Array Solar Cell with 15.3 % Efficiency at 1 Sun. *IEEE Journal of Photovoltaics*, 6, 185, 2016. (Cited on pages 13 and 79.)

[90] D. van Dam, N. J. J. van Hoof, Y. Cui, R. P. J. van Veldhoven, E. P. A. M. Bakkers, J. Gómez Rivas, and J. E. M. Haverkort. High-efficiency nanowire solar cells with omnidirectionally enhanced absorption due to self-aligned ITO Mie scatterers. *submitted*. (Cited on page 13.)

[91] H. E. Ruda and A. Shik. Polarization-sensitive optical phenomena in semiconducting and metallic nanowires. *Physical Review B*, 72(11), 115308, sep 2005. (Cited on pages 14 and 73.)

[92] A. V. Maslov and C. Z. Ning. Reflection of guided modes in a semiconductor nanowire laser. *Applied Physics Letters*, 83(6), 1237, 2003. (Cited on page 14.)

[93] A. V. Maslov and C. Z. Ning. Far-field emission of a semiconductor nanowire laser. *Optics Letters*, 29(6), 572–574, 2004. (Cited on pages 14, 65, and 80.)

[94] A. V. Maslov, M. I. Bakunov, and C. Z. Ning. Distribution of optical emission between guided modes and free space in a semiconductor nanowire. *Journal of Applied Physics*, 99(2), 024314, 2006. (Cited on pages 14 and 65.)

[95] A. V. Maslov and C. Z. Ning. Radius-dependent polarization anisotropy in semiconductor nanowires. *Physical Review B*, 72(16), 161310, oct 2005. (Cited on page 14.)

[96] H. E. Ruda and A. Shik. Polarization-sensitive optical phenomena in thick semiconducting nanowires. *Journal of Applied Physics*, 100(2), 024314, 2006. (Cited on pages 14, 72, 73, and 82.)

[97] A. Lan, J. Giblin, V. Protasenko, and M. Kuno. Excitation and photoluminescence polarization anisotropy of single CdSe nanowires. *Applied Physics Letters*, 92(18), 183110, 2008. (Cited on page 14.)

[98] H.-Y. Chen, Y.-C. Yang, H.-W. Lin, S.-C. Chang, and S. Gwo. Polarized photoluminescence from single GaN nanorods: effects of optical confinement. *Optics Express*, 16(17), 13465–75, aug 2008. (Cited on pages 14, 73, and 89.)

[99] C. F. Bohren and D. R. Huffman. *Absorption and scattering of light by small particles*. John Wiley & Sons, 1983. (Cited on pages 14, 27, and 55.)

[100] M. H. M. Van Weert, N. Akopian, F. Kelkensberg, U. Perinetti, M. P. Van Kouwen, J. Gómez Rivas, M. T. Borgström, R. E. Algra, M. A. Verheijen, E. P. A. M. Bakkers, L. P. Kouwenhoven, and V. Zwiller. Orientation-dependent optical-polarization properties of single quantum dots in nanowires. *Small*, 5(19), 2134–2138, oct 2009. (Cited on pages 14, 55, 66, 73, and 74.)

[101] G. Chen, J. Wu, Q. Lu, H. R. Gutierrez, Q. Xiong, M. E. Pellen, J. S. Petko, D. H. Werner, and P. C. Eklund. Optical Antenna Effect in Semiconductor Nanowires. *Nano Letters*, 8(5), 1341–1346, 2008. (Cited on pages 14 and 65.)

[102] I. Friedler, C. Sauvan, J. P. Hugonin, P. Lalanne, J. Claudon, and J.-M. Gérard. Solid-state single photon sources: the nanowire antenna. *Optics Express*, 17(4), 2095–110, mar 2009. (Cited on pages 16, 65, and 79.)

[103] G. Grzela, R. Paniagua-Domínguez, T. Barten, Y. Fontana, J. A. Sánchez-Gil, and J. Gómez Rivas. Nanowire Antenna Emission. *Nano Letters*, 12(11), 5481–5486, 2012. (Cited on pages 14, 16, 65, 69, 74, 79, and 82.)

[104] G. Grzela. *Directional light emission and absorption by semiconductor nanowires*. PhD thesis, Eindhoven University of Technology, 2013. (Cited on pages 14, 32, 37, 38, 67, and 74.)

[105] D. R. Abujetas, R. Paniagua-Domínguez, and J. A. Sánchez-Gil. Unraveling the Janus Role of Mie Resonances and Leaky/Guided Modes in Semiconductor Nanowire Absorption for Enhanced Light Harvesting. *ACS Photonics*, 2(7), 921–929, 2015. (Cited on page 14.)

[106] N. Anttu and H. Q. Xu. Scattering matrix method for optical excitation of surface plasmons in metal films with periodic arrays of subwavelength holes. *Physical Review B*, 83(16), 165431, apr 2011. (Cited on page 14.)

[107] N. Anttu and H. Q. Xu. Efficient light management in vertical nanowire arrays for photovoltaics. *Optics Express*, 21, A558, 2013. (Cited on pages 14 and 80.)

[108] J. Kupec, R. L. Stoop, and B. Witzigmann. Light absorption and emission in nanowire array solar cells. *Optics Express*, 18(26), 4651–4656, 2010. (Cited on pages 14 and 15.)

[109] B. Wang and P. W. Leu. Enhanced absorption in silicon nanocone arrays for photovoltaics. *Nanotechnology*, 23(19), 194003, may 2012. (Cited on page 15.)

[110] Y. Wang, V. Schmidt, S. Senz, and U. Gosele. Epitaxial growth of silicon nanowires using an aluminium catalyst. *Nature Nanotechnology*, 1(December), 186–189, 2006. (Cited on page 15.)

[111] I. Schnitzer, E. Yablonovitch, C. Caneau, T. J. Gmitter, and A. Scherer. 30% External Quantum Efficiency From Surface Textured, Thin-Film Light-Emitting Diodes. *Applied Physics Letters*, 63(16), 2174–2176, 1993. (Cited on pages 15 and 16.)

[112] M. L. Kuo, Y. S. Kim, M. L. Hsieh, and S. Y. Lin. Efficient and directed nano-LED emission by a complete elimination of transverse-electric guided modes. *Nano Letters*, 11(2), 476–481, 2011. (Cited on page 16.)

[113] J. J. Wierer, A. David, and M. M. Megens. III-nitride photonic-crystal light-emitting diodes with high extraction efficiency. *Nature Photonics*, 3(3), 163–169, feb 2009. (Cited on pages 16 and 65.)

[114] E. Matioli, S. Brinkley, K. M. Kelchner, Y.-L. Hu, S. Nakamura, S. DenBaars, J. S. Speck, and C. Weisbuch. High-brightness polarized light-emitting diodes. *Light: Science & Applications*, 1(8), e22, aug 2012. (Cited on page 16.)

[115] C. P. T. Svensson, T. Mårtensson, J. Trägårdh, C. Larsson, M. Rask, D. Hessman, L. Samuelson, and J. Ohlsson. Monolithic GaAs/InGaP nanowire light emitting diodes on silicon. *Nanotechnology*, 19(30), 305201, jul 2008. (Cited on pages 16 and 65.)

[116] J. H. Son, J. U. Kim, Y. H. Song, B. J. Kim, C. J. Ryu, and J. L. Lee. Design Rule of nanostructures in light-emitting diodes for complete elimination of total internal reflection. *Advanced Materials*, 24(17), 2259–2262, 2012. (Cited on page 16.)

[117] M. Crawford. LEDs for Solid-State Lighting: Performance Challenges and Recent Advances. *IEEE Journal of Selected Topics in Quantum Electronics*, 15(4), 1028–1040, jul 2009. (Cited on page 16.)

[118] W. L. Barnes, G. Björk, J.-M. Gérard, P. Jonsson, J. Wasey, P. Worthing, and V. Zwiller. Solid-state single photon sources: light collection strategies. *The European Physical Journal D - Atomic, Molecular and Optical Physics*, 18(2), 197–210, 2002. (Cited on page 16.)

[119] J. Claudon, J. Bleuse, N. S. Malik, M. Bazin, P. Jaffrennou, N. Gregersen, C. Sauvan, P. Lalanne, and J.-M. Gérard. A highly efficient single-photon source based on a quantum dot in a photonic nanowire. *Nature Photonics*, 4(3), 174–177, jan 2010. (Cited on pages 16, 45, 65, and 79.)

[120] J. Claudon, N. Gregersen, P. Lalanne, and J.-M. Gérard. Harnessing Light with Photonic Nanowires: Fundamentals and Applications to Quantum Optics. *ChemPhysChem*, 14(11), 2393–2404, jun 2013. (Not cited.)

[121] M. E. Reimer, G. Bulgarini, N. Akopian, M. Hocevar, M. Bouwes Bavinck, M. A. Verheijen, E. P. A. M. Bakkers, L. P. Kouwenhoven, and V. Zwiller. Bright single-photon sources in bottom-up tailored nanowires. *Nature Communications*, 3, 737, jan 2012. (Cited on pages 16, 79, and 80.)

[122] N. Gregersen, T. R. Nielsen, J. Claudon, J.-M. Gérard, and J. Mørk. Controlling the emission profile of a nanowire with a conical taper. *Optics Letters*, 33(15), 1693–1695, 2008. (Cited on page 16.)

[123] G. Bulgarini, M. E. Reimer, M. Bouwes Bavinck, K. D. Jöns, D. Dalacu, P. J. Poole, E. P. A. M. Bakkers, and V. Zwiller. Nanowire Waveguides Launching Single Photons in a Gaussian Mode for Ideal Fiber Coupling. *Nano Letters*, 14(7), 4102–4106, jun 2014. (Cited on pages 16

and 79.)

[124] B. J. M. Brenny, D. van Dam, C. I. Osorio, J. Gómez Rivas, and A. Polman. Azimuthally polarized cathodoluminescence from InP nanowires. *Applied Physics Letters*, 107, 201110, 2015. (Cited on page 16.)

[125] B. J. M. Brenny, D. R. Abujetas, D. van Dam, J. A. Sánchez-Gil, J. Gómez Rivas, and A. Polman. Directional Emission from Leaky and Guided Modes in GaAs Nanowires Measured by Cathodoluminescence. *ACS Photonics*, 3, 677–684, 2016. (Cited on page 16.)

[126] U. Rau. Reciprocity relation between photovoltaic quantum efficiency and electroluminescent emission of solar cells. *Physical Review B*, 76(8), 1–8, 2007. (Cited on pages 19, 46, and 47.)

[127] O. D. Miller. *Photonic design: From Fundamental Solar Cell Physics to Computational Inverse Design*. PhD thesis, University of California, Berkeley, 2012. (Not cited.)

[128] S. J. Byrnes. The Shockley Queisser Limit: http://sjbyrnes.com/sq.html. (Cited on page 21.)

[129] Y. Xu, T. Gong, and J. N. Munday. The generalized Shockley-Queisser limit for nanostructured solar cells. *Scientific Reports*, 5, 13536, 2015. (Cited on pages 19, 65, and 79.)

[130] M. A. Green. Solar Cell Fill Factors: General Graph and Empirical Expressions. *Solid State Electronics*, 24(8), 788–789, 1981. (Cited on page 21.)

[131] M. A. Steiner, J. F. Geisz, D. J. Friedman, A. Duda, W. J. Olavarria, M. Young, D. Kuciauskas, and S. R. Kurtz. Effects of Internal Luminescence and Internal Optics on Voc and Jsc of III-V Solar Cells. *IEEE Journal of Photovoltaics*, 3(4), 1437–1442, 2013. (Cited on page 25.)

[132] M. A. Steiner, J. F. Geisz, I. Garcia, D. J. Friedman, A. Duda, and S. R. Kurtz. Optical enhancement of the open-circuit voltage in high quality GaAs solar cells. *Journal of Applied Physics*, 113(12), 123109, 2013. (Cited on pages 25 and 44.)

[133] G. Mie. Beitraege zur Optic trueber Medien, speziell kolloidaler Metalloesungen. *Annalen der Physik*, 4(3), 377–445, 1908. (Cited on pages 27 and 55.)

[134] J. A. Stratton. *Electromagnetic Theory*. Cambridge University Press, Cambridge, 1941. (Cited on pages 29 and 89.)

[135] A. W. Snyder and J. D. Love. *Optical Waveguide Theory*. Chapman and Hall, 1983. (Cited on pages 29 and 82.)

[136] R. Paniagua-Domínguez, G. Grzela, J. Gómez Rivas, and J. A. Sánchez-Gil. Enhanced and directional emission of semiconductor nanowires tailored through leaky/guided modes. *Nanoscale*, 5(21), 10582–90, nov 2013. (Cited on pages 31, 32, 65, 69, 75, and 83.)

[137] G. Lozano, T. Barten, G. Grzela, and J. Gómez Rivas. Directional absorption by phased arrays of plasmonic nanoantennae probed with time-reversed Fourier microscopy. *New Journal of Physics*, 16(1), 013040, jan 2014. (Cited on page 37.)

[138] Imina. Imina Technologies SA: http://www.imina.ch/. (Cited on page 37.)

[139] P. Würfel. The chemical potential of radiation. *Journal of Physics C: Solid State Physics*, 15(18), 3967–3985, 1982. (Cited on pages 38 and 46.)

[140] J. K. Katahara and H. W. Hillhouse. Quasi-Fermi level splitting and sub-bandgap absorptivity from semiconductor photoluminescence. *Journal of Applied Physics*, 116(May 2015), 173504, 2014. (Cited on page 38.)

[141] T.-T. D. Tran, H. Sun, K. W. Ng, F. Ren, K. Li, F. Lu, E. Yablonovitch, and C. J. Chang-Hasnain. High brightness InP micropillars grown on silicon with Fermi level splitting larger than 1 eV. *Nano Letters*, 14, 3235–3240, 2014. (Cited on pages 38 and 46.)

[142] L. Cao, J. S. White, J.-S. Park, J. A. Schuller, B. M. Clemens, and M. L. Brongersma. Engineering light absorption in semiconductor nanowire devices. *Nature Materials*, 8(8), 643–647, aug 2009. (Cited on pages 43, 44, 55, 79, and 93.)

[143] A. Polman and H. A. Atwater. Photonic design principles for ultrahigh-efficiency photovoltaics. *Nature Materials*, 11(3), 174–7, mar 2012. (Cited on page 43.)

[144] S. Sandhu, Z. Yu, and S. Fan. Detailed balance analysis of nanophotonic solar cells. *Optics Express*, 21(1), 1209–17, jan 2013. (Cited on page 43.)

[145] S. Sandhu, Z. Yu, and S. Fan. Detailed Balance Analysis and Enhancement of Open-Circuit Voltage in Single-Nanowire Solar Cells. *Nano Letters*, 14(2), 2014. (Cited on page 43.)

[146] H. J. Joyce, J. Wong-Leung, C.-K. Yong, C. J. Docherty, S. Paiman, Q. Gao, H. H. Tan, C. Jagadish, J. Lloyd-Hughes, L. M. Herz, and M. B. Johnston. Ultralow surface recombination velocity in InP nanowires probed by terahertz spectroscopy. *Nano Letters*, 12(10), 5325–30, oct 2012. (Cited on page 46.)

[147] P. B. Clapham and M. C. Hutley. Reduction of Lens Reflexion by the "Moth-Eye" Principle. *Nature*, 244, 281–282, 1973. (Cited on pages 46 and 55.)

[148] R. T. Ross. Some Thermodynamics of Photochemical Systems. *The Journal of Chemical Physics*, 46(12), 4590, 1967. (Cited on page 46.)

[149] E. D. Palik. *Handbook of Optical Constants of Solids*. Academic, 1985. (Cited on page 49.)

[150] E. F. Schubert. *Light-Emitting Diodes*. E Fred Schubert, second edi edition, 2006. (Cited on page 49.)

[151] J. Oh, H.-C. Yuan, and H. M. Branz. An 18.2%-efficient black-silicon solar cell achieved through control of carrier recombination in nanostructures. *Nature Nanotechnology*, 7(September), 2–5, 2012. (Cited on page 53.)

[152] P. Repo, A. Haarahiltunen, L. Sainiemi, M. Yli-Koski, H. Talvitie, M. C. Schubert, and H. Savin. Effective passivation of black silicon surfaces by atomic layer deposition. *IEEE Journal of Photovoltaics*, 3(1), 90–94, 2013. (Cited on page 53.)

[153] H. J. Joyce, P. Parkinson, N. Jiang, C. J. Docherty, Q. Gao, H. H. Tan, C. Jagadish, L. M. Herz, and M. B. Johnston. Electron Mobilities Approaching Bulk Limits in "Surface-Free" GaAs Nanowires. *Nano Letters*, 14(10), 5989–94, 2014. (Cited on page 53.)

[154] V. E. Ferry, M. A. Verschuuren, M. C. V. Lare, R. E. I. Schropp, H. A. Atwater, and A. Polman. Optimized spatial correlations for broadband light trapping nanopatterns in high efficiency ultrathin film a-Si:H solar cells. *Nano Letters*, 11(10), 4239–4245, 2011. (Cited on page 55.)

[155] L. Gao, Y. Cui, R. H. J. Vervuurt, D. van Dam, R. P. J. van Veldhoven, J. P. Hofmann, A. A. Bol, J. E. M. Haverkort, P. H. L. Notten, E. P. A. M. Bakkers, and E. J. M. Hensen. High-Efficiency InP-Based Photocathode for Hydrogen Production by Interface Energetics Design and Photon Management. *Advanced Functional Materials*, 26(5), 679–686, 2016. (Cited on pages 55 and 93.)

[156] J.-H. Yun, E. Lee, H.-H. Park, D.-W. Kim, W. A. Anderson, J. Kim, N. M. Litchinitser, J. Zeng, J. Yi, M. M. D. Kumar, and J. Sun. Incident light adjustable solar cell by periodic nanolens architecture. *Scientific Reports*, 4, 6879, 2014. (Cited on page 55.)

[157] Y. Cui, D. van Dam, S. A. Mann, N. J. J. van Hoof, E. C. Garnett, E. P. A. M. Bakkers, and J. E. M. Haverkort. Boosting solar cell photovoltage by nanophotonic engineering. *submitted*. (Cited on page 55.)

[158] X. Yin, C. Battaglia, Y. Lin, K. Chen, M. Hettick, M. Zheng, C.-Y. Chen, D. Kiriya, and A. Javey. 19.2% Efficient InP Heterojunction Solar Cell with Electron-Selective TiO2 Contact. *ACS Photonics*, 1, 1245–1250, 2014. (Cited on page 55.)

[159] G. Mariani, Z. Zhou, A. Scofield, and D. L. Huffaker. Direct-bandgap epitaxial core-multishell nanopillar photovoltaics featuring subwavelength optical concentrators. *Nano Letters*, 13(4), 1632–1637, 2013. (Cited on page 56.)

[160] J. Yoo, B.-M. Nguyen, I. H. Campbell, S. A. Dayeh, P. Schuele, D. Evans, and S. T. Picraux. Si Radial p-i-n Junction Photovoltaic Arrays with Built-In Light Concentrators. *ACS Nano*, 9(5), 5154–5163, 2015. (Cited on page 56.)

[161] H. Lin, F. Xiu, M. Fang, S. Yip, H.-y. Cheung, F. Wang, N. Han, S. C. Chan, C.-Y. Wong, and J. C. Ho. Rational Design of Inverted Nanopencil Arrays for Cost-Effective, Broadband, and Omnidirectional Light Harvesting. *ACS Nano*, 8(4), 3752–3760, 2014. (Cited on page 56.)

[162] Y. Cui. *High-efficiency Nanowire Solar Cells*. PhD thesis, Eindhoven University of Technology, 2015. (Cited on page 56.)

[163] S. Person, M. Jain, Z. Lapin, J. J. Sáenz, G. Wicks, and L. Novotny. Demonstration of zero optical backscattering from single nanoparticles. *Nano Letters*, 13(4), 1806–1809, 2013. (Cited on page 60.)

[164] Y. H. Fu, A. I. Kuznetsov, A. E. Miroshnichenko, Y. F. Yu, and B. Luk'yanchuk. Directional visible light scattering by silicon nanoparticles. *Nature Communications*, 4, 1527, 2013. (Not cited.)

[165] B. S. Luk'yanchuk, N. V. Voshchinnikov, R. Paniagua-Domínguez, and A. I. Kuznetsov. Optimum Forward Light Scattering by Spherical and Spheroidal Dielectric Nanoparticles with High Refractive Index. *ACS Photonics*, 2(7), 150616161431005, 2015. (Cited on page 60.)

[166] M. Kerker, D.-S. Wang, and C. L. Giles. Electromagnetic scattering by magnetic spheres. *Journal of the Optical Society of America*, 73(6), 765, 1983. (Cited on page 61.)

[167] A. Lundskog, C.-W. Hsu, K. Fredrik Karlsson, S. Amloy, D. Nilsson, U. Forsberg, P. Olof Holtz, and E. Janzén. Direct generation of linearly polarized photon emission with designated orientations from site-controlled InGaN quantum dots. *Light: Science & Applications*, 3(1), e139, jan 2014. (Cited on pages 65 and 66.)

[168] R. Röder, D. Ploss, A. Kriesch, R. Buschlinger, S. Geburt, U. Peschel, and C. Ronning. Polarization features of optically pumped CdS nanowire lasers. *Journal of Physics D: Applied Physics*, 47(39), 394012, oct 2014. (Cited on page 65.)

[169] A. G. Curto, G. Volpe, T. H. Taminiau, M. P. Kreuzer, R. Quidant, and N. F. van Hulst. Unidirectional emission of a quantum dot coupled to a nanoantenna. *Science*, 329(5994), 930–3, aug 2010. (Cited on page 65.)

[170] K. G. Lee, X. W. Chen, H. Eghlidi, P. Kukura, R. Lettow, a. Renn, V. Sandoghdar, and S. Götzinger. A planar dielectric antenna for directional single-photon emission and near-unity collection efficiency. *Nature Photonics*, 5(3), 166–169, jan 2011. (Cited on page 65.)

[171] R. Yan, D. Gargas, and P. Yang. Nanowire photonics. *Nature Photonics*, 3(10), 569–576, oct 2009. (Cited on page 65.)

[172] S. L. Diedenhofen, O. T. A. Janssen, M. Hocevar, A. Pierret, E. P. A. M. Bakkers, H. P. Urbach, and J. Gómez Rivas. Controlling the directional emission of light by periodic arrays of heterostructured semiconductor nanowires. *ACS Nano*, 5(7), 5830–5837, 2011. (Cited on pages 65 and 76.)

[173] P. D. Anderson, C. Lin, and M. L. Povinelli. Effect of guided resonance modes on emission from GaN core-shell nanorod arrays. *Applied Physics A*, 117(4), 1879–1884, jul 2014. (Cited on page 65.)

[174] Y. Fontana, G. Grzela, E. P. A. M. Bakkers, and J. Gómez Rivas. Mapping the directional emission of quasi-two-dimensional photonic crystals of semiconductor nanowires using Fourier microscopy. *Physical Review B*, 86(24), 245303, dec 2012. (Cited on pages 65 and 76.)

[175] A. Mishra, L. V. Titova, T. B. Hoang, H. E. Jackson, L. M. Smith, J. M. Yarrison-Rice, Y. Kim, H. J. Joyce, Q. Gao, H. H. Tan, and C. Jagadish. Polarization and temperature dependence of photoluminescence from zincblende and wurtzite InP nanowires. *Applied Physics Letters*, 91(26), 263104, 2007. (Cited on pages 66 and 73.)

[176] A.-L. Henneghien, B. Gayral, Y. Désières, and J.-M. Gérard. Simulation of waveguiding and emitting properties of semiconductor nanowires with hexagonal or circular sections. *Journal of the Optical Society of America B*, 26(12), 2396, 2009. (Cited on page 69.)

[177] D. Spirkoska, A. L. Efros, W. R. L. Lambrecht, T. Cheiwchanchamnangij, A. Fontcuberta i Morral, and G. Abstreiter. Valence band structure of polytypic zinc-blende/wurtzite GaAs

nanowires probed by polarization-dependent photoluminescence. *Physical Review B*, 85(4), 045309, jan 2012. (Cited on page 73.)

[178] J. Birman. Some Selection Rules for Band-Band Transitions in Wurtzite Structure. *Physical Review*, 114(6), 1490–1492, 1959. (Cited on pages 74, 83, and 92.)

[179] C. Wilhelm, A. Larrue, X. Dai, D. Migas, and C. Soci. Anisotropic photonic properties of III-V nanowires in the zinc-blende and wurtzite phase. *Nanoscale*, 4(5), 1446–54, mar 2012. (Cited on pages 74 and 83.)

[180] R. Paniagua-Domínguez, G. Grzela, J. Gómez Rivas, and J. A. Sánchez-Gil. Semiconductor nanowire photoluminescence: spatial/polarization averaged coupling into leaky modes. *Proceedings of SPIE*, 8808, 88080J, sep 2013. (Cited on page 75.)

[181] J. D. Joannopoulos, S. G. Johnson, J. N. Winn, and R. D. Meade. *Photonic Crystals: Molding the Flow of Light*. Princeton University Press, Princeton, 2nd edition, 2008. (Cited on page 76.)

[182] S. G. Johnson and J. D. Joannopoulos. Block-iterative frequency-domain methods for Maxwell's equations in a planewave basis. *Optics Express*, 8(3), 173, jan 2001. (Cited on page 76.)

[183] A. Koeck, E. Gornik, M. Hauser, and W. Beinstingl. Strongly directional emission from AlGaAs/GaAs light-emitting diodes. *Applied Physics Letters*, 57(22), 2327, 1990. (Cited on page 79.)

[184] K. Seo, M. Wober, P. Steinvurzel, E. Schonbrun, Y. Dan, T. Ellenbogen, and K. B. Crozier. Multicolored vertical silicon nanowires. *Nano Letters*, 11(4), 1851–1856, 2011. (Cited on page 80.)

[185] G. Bulgarini, M. E. Reimer, T. Zehender, M. Hocevar, E. P. A. M. Bakkers, L. P. Kouwenhoven, and V. Zwiller. Spontaneous emission control of single quantum dots in bottom-up nanowire waveguides. *Applied Physics Letters*, 100(12), 121106, 2012. (Cited on page 80.)

[186] S. Assali, L. Gagliano, D. S. Oliveira, M. A. Verheijen, L.-F. Feiner, S. R. Plissard, and E. P. A. M. Bakkers. Exploring crystal phase switching in GaP nanowires. *Nano Letters*, 15(12), 8062–8069, 2015. (Cited on page 87.)

[187] S. Lehmann, D. Jacobsson, and K. A. Dick. Crystal phase control in GaAs nanowires: opposing trends in the Ga- and As-limited growth regimes. *Nanotechnology*, 26(30), 301001, 2015. (Cited on page 87.)

[188] F. Bechstedt and A. Belabbes. Structure, energetics, and electronic states of III-V compound polytypes. *Journal of Physics: Condensed Matter*, 25(27), 273201, jul 2013. (Cited on page 87.)

[189] A. J. Standing, S. Assali, L. Gao, M. A. Verheijen, D. van Dam, Y. Cui, P. H. L. Notten, J. E. M. Haverkort, and E. P. A. M. Bakkers. Efficient water reduction with gallium phosphide nanowires. *Nature Communications*, 6(May), 7824, 2015. (Cited on pages 87 and 93.)

[190] S. Assali, I. Zardo, S. R. Plissard, D. Kriegner, M. A. Verheijen, G. Bauer, A. Meijerink, A. Belabbes, F. Bechstedt, J. E. M. Haverkort, and E. P. A. M. Bakkers. Direct Band Gap Wurtzite Gallium Phosphide Nanowires. *Nano Letters*, 13(4), 1559–1563, 2013. (Cited on pages 87 and 88.)

[191] S. Assali, I. Zardo, J. Greil, A. Belabbes, M. de Moor, F. Bechstedt, E. P. A. M. Bakkers, and J. E. M. Haverkort. Optical study of the band structure of wurtzite GaP nanowires. *Under review*. (Cited on pages 87 and 88.)

[192] R.-M. Ma, X.-L. Wei, L. Dai, S.-F. Liu, T. Chen, S. Yue, Z. Li, Q. Chen, and G. G. Qin. Light Coupling and Modulation in Coupled Nanowire Ring - Fabry-Perot Cavity. *Nano Letters*, 9(7), 2697–2703, 2009. (Cited on pages 88 and 89.)

[193] B. Piccione, C.-H. Cho, L. K. van Vugt, and R. Agarwal. All-optical active switching in individual semiconductor nanowires. *Nature Nanotechnology*, 7(10), 640–5, oct 2012. (Not cited.)

[194] B. Hua, J. Motohisa, Y. Ding, S. Hara, and T. Fukui. Characterization of Fabry-Pérot microcavity modes in GaAs nanowires fabricated by selective-area metal organic vapor phase epitaxy. *Applied Physics Letters*, 91(2007), 131112–1–3, 2010. (Cited on page 88.)

[195] L. K. van Vugt, S. Ruehle, and D. Vanmaekelbergh. Phase-Correlated Nondirectional Laser Emission from the End Facets of a ZnO Nanowire. *Nano Letters*, 6(12), 2707–2711, 2006. (Cited on page 88.)

[196] M. A. Zimmler, F. Capasso, S. Müller, and C. Ronning. Optically pumped nanowire lasers: invited review. *Semiconductor Science and Technology*, 25(024001), 1–12, feb 2010. (Cited on page 89.)

[197] G. Ghosh. Sellmeier coefficients and dispersion of thermo-optic coefficients for some optical glasses. *Applied Optics*, 36(7), 1540, mar 1997. (Cited on page 89.)

[198] K. Iizuka. *Engineering Optics*. Springer, third edition, 2008. (Cited on page 89.)

[199] D. Yas'kov and A. Pikhtin. Optical properties of gallium phosphide grown by floating zone I. Refractive index and reflection coefficient. *Material Research Bulletin*, 4(10), 781–788, 1969. (Cited on page 92.)

[200] T. S. Moss. Relations between the Refractive Index and Energy Gap of Semiconductors. *Physica Status Solidi (B)*, 131(2), 415–427, oct 1985. (Cited on page 92.)

[201] M. Aghaeipour, N. Anttu, G. Nylund, A. Berg, S. Lehmann, and M.-E. Pistol. Optical response of wurtzite and zinc blende GaP nanowire arrays. *Optics Express*, 23(23), 30177, 2015. (Cited on page 92.)

[202] L. Cao, J.-S. Park, P. Fan, B. M. Clemens, and M. L. Brongersma. Resonant germanium nanoantenna photodetectors. *Nano Letters*, 10(4), 1229–1233, apr 2010. (Cited on page 93.)

[203] O. L. Muskens, M. T. Borgström, E. P. A. M. Bakkers, and J. Gómez Rivas. Giant optical birefringence in ensembles of semiconductor nanowires. *Applied Physics Letters*, 89(23),

253–255, 2006. (Cited on page 93.)

[204] R. Paniagua-Domínguez, D. R. Abujetas, and J. A. Sánchez-Gil. Ultra low-loss, isotropic optical negative-index metamaterial based on hybrid metal-semiconductor nanowires. *Scientific Reports*, 3, 1507, 2013. (Cited on page 93.)

$a(E)$	Absorptance
A	Area
BCB	Benzocyclobutene
c	Speed of light in vacuum
CCD	Charge-coupled device
d	Nanowire diameter
e	Euler's constant
E	Energy
E_g	Band gap energy
EQE	External (photovoltaic) quantum efficiency (equivalent: IPCE, incident photon to converted electron ratio)
ε_e, ε_c	Dielectric function of environment, cylinder
$\phi(E_g)$	Incident flux of photons with energy above the band gap E_g
f	Material filling fraction
FF	Fill factor of current vs voltage characterization
FWHM	Full-width at half maximum
h	Planck's constant
H_m	m^{th} order Hankel function of the first kind
η	Power conversion efficiency
η_{ext}	External radiative efficiency (equivalent: EQE_{LED}, external LED quantum efficiency, (photoluminescence) quantum yield)
η_{int}	Internal radiative efficiency (equivalent: internal quantum yield)
InP	Indium phosphide
IQE	Internal quantum efficiency: ratio of absorbed photon and generated electron rates
ITO	Indium tin oxide
J_0	Dark current density
J_{SC}	Short-circuit current density / photocurrent density (at short-circuit)
J_m	m^{th} order Bessel function of the first kind
μ	chemical potential / quasi-Fermi level splitting

k_B	Boltzmann's constant
k, $k_{\|}$, k_z	Wave number, parallel component of wave number, z-component of wave number
k_0	Free space wave number, equal to $2\pi/\lambda = \omega/c$
λ	Wavelength
MOVPE	Metal-organic Vapor Phase Epitaxy
n	Refractive index
n_E	Mode index
NA	Numerical aperture
p	Nanowire array period
$\overline{P_{abs}}$	Wavelength-, position- and direction-averaged photon absorption probability
$\overline{P_{esc}}$	Wavelength-, position- and direction-averaged photon escape probability (equivalent: extraction efficiency)
$\overline{P_{par}}$	Wavelength-, position- and direction-averaged parasitic photon absorption probability
PL	Photoluminescence
q	Electron charge
Q_{abs}	Absorption efficiency
Q_{ext}	Extinction efficiency
Q_{scat}	Scattering efficiency
Q	Quality factor
r	Nanowire radius
R	Reflection coefficient
R_{gen}	Generation rate per unit area
R_{rad}, R_{nrad}	Radiative, nonradiative recombination rate per unit area
ρ	Polarization anisotropy
SEM	Scanning Electron Microscopy
T	Temperature in Kelvin
TRFM	Time-reversed Fourier Microscopy
θ	Angle between the wave vector and the normal to the substrate, or between the wave vector and the long axis of the nanowire
V_{OC}	Open-circuit potential / photovoltage
V_{OC}^{rad}	Open-circuit potential assuming that all recombination is radiative
WZ	Wurtzite
ZB	Zinc blende
ω	Frequency

SCIENTIFIC SUMMARY

To match the increasing demand for clean energy, the market of solar cells is rapidly growing. However, there is still a large difference between the actual power conversion efficiency of state-of-the-art solar cells and their theoretical maximum efficiency. The power generation of a solar cell is limited by their photovoltage and photocurrent. Both the solar cell voltage and current can be enhanced when using nanostructured solar cells instead of planar cells. One type of nanostructures that are being used for solar cells are semiconductor nanowires, which are elongated structures with lengths of 1-10 micrometers and diameters of 100-300 nanometers. Arrays of these vertical nanowires show promising photovoltaic performance.

This thesis is devoted to investigate the interaction between light and nanowires. We demonstrate that arrays of semiconductor nanowires can be used to make solar cells with a high photocurrent and also a higher photovoltage than their planar counterparts. The photovoltage is measured by photoluminescence spectroscopy of intrinsic samples which were fabricated by a top-down etching methods, which allows to directly compare a nanowire layer with a planar layer with the exact same material quality. The higher photovoltage is caused by reduction of the material volume, which implies a decrease of the number of charge traps. A second effect is the increased emission probability from nanowire layers due to waveguiding and a lower effective refractive index. The high photocurrent is due to the antenna effect of nanowires, enabling them to absorb light from a larger area than their projected geometrical area. On top of that, the morphology of the transparent solar cell contact layer also enhances the photocurrent. Together, all these effects promise higher power conversion efficiencies in nanowire solar cells than in planar solar cells with the same material quality. We have also investigated the angle-dependence of the nanowire solar cell performance. We found that these cell perform well for light impinging at incident angles up to 60 degrees with respect to the sample normal, which is caused by the precise cell geometry.

An important parameter for the photovoltage of a solar cell is the direction of the re-emitted light generated within the cell. The difference in entropy between incident photon beam and the emitted photon beam results in a loss in the photovoltage. A narrower angular emission cone means a smaller increase in the photon entropy with respect to a wide emission cone, which reduces this important loss in the photovoltage. The direction of the emission is also of seminal importance for light-emitting diodes (LEDs), nanolasers, and single-photon sources based on nanowires. Therefore, we have investigated the directional photoluminescence emission of vertical nanowires using back-focal plane imaging, also known as Fourier microscopy. We have found that the diameter is the crucial parameter in this aspect. The diameter controls the presence and propagation of waveguide modes supported by the cylindrical geometry of

the nanowire, which determines the directional emission pattern. This diameter-dependence of the waveguide modes is very sensitive and can lead to abrupt changes in the directional emission. Also the polarization of the light is controlled by the waveguide modes. The presence of waveguide modes needs to be taken into account in the design of all photonic or opto-electronic devices based on semiconductor nanowires. Finally, we have used nanowire waveguide resonances to experimentally determine the high refractive index of a novel material, wurtzite gallium phosphide, which will be of importance for many applications.

In summary, this thesis demonstrates the advantages for nanowires to be used in solar cells. It provides guidelines in the design of these and other optoelectronic nanowire devices and stresses the physical mechanisms that dominate light emission and light absorption of semiconductor nanowires.

WETENSCHAPPELIJKE SAMENVATTING

Om aan de toenemende vraag aan schone energie tegemoet te komen, is het nodig dat de efficiëntie van zonne-energie verbetert. Immers, er is nog steeds een aanzienlijk verschil tussen de prestaties van de zonnepanelen op de markt en de theoretisch maximale prestaties. De efficiëntie van fotovoltaïsche zonnecellen wordt gelimiteerd door het product van hun spanning en hun stroom. Zowel de spanning als de stroom van een vlakke zonnecel kan worden vergroot door gebruik te maken van nanostructuren in het deel van de zonnecel dat licht absorbeert. Een type nanostructuren dat wordt gebruikt in zonnecellen zijn nanodraden: langwerpige structuren met een lengte van 1 tot 10 micrometer en diameter van 100 tot 300 nanometer. Regelmatige roosters van verticaal geplaatste nanodraden hebben een veelbelovende toekomst in de fotovoltaïca.

Dit proefschrift onderzoekt de interactie tussen licht en nanodraden. We demonstreren dat periodieke roosters van halfgeleider nanodraden kunnen worden gebruikt om zonnecellen te maken met zowel een hogere fotostroom als een hogere fotospanning ten opzichte van vlakke zonnecellen gemaakt van hetzelfde materiaal. De fotospanning is gemeten door middel van fotoluminescentie-spectroscopie op ongedoteerde nanodraadroosters, gemaakt door middel van het etsen van een gegroeide laag indiumfosfide. Op deze manier kunnen we een nanodraadlaag direct vergelijken met een vlakke laag met de exact identieke materiaalkwaliteit. De hogere fotospanning wordt veroorzaakt door een reductie in de gebruikte hoeveelheid materiaal. Dit betekent namelijk ook een vermindering in de hoeveelheid elektrische bulkdefecten. Een tweede effect is de verbeterde emissiekans van intern gegenereerde lichtemissie in de nanodraadlaag, door golfgeleiding langs de nanodraden en een lagere effectieve brekingsindex. De hogere fotostroom wordt veroorzaakt door een antenne-effect van de nanodraden, wat zorgt dat ze licht kunnen absorberen van een groter oppervlak dan hun geprojecteerde geometrische oppervlak. Daarnaast zorgt ook de precieze vorm van het transparante zonnecelcontact voor een hogere fotostroom. We hebben ook de hoekafhankelijke fotostroom van de zonnecellen onderzocht. De cellen hebben nauwelijks extra reflectieverliezen tot een hoek van inval van 60 graden ten opzichte van een loodrechte lijn op het oppervlak. Dit is van belang voor diffuus licht of in zonnecellen met concentrators.

Een belangrijke parameter voor de fotospanning van een zonnecel is de richting van het uitgezonden licht dat in de zonnecel wordt gegenereerd. Fotonen die van de zon op de zonnecel terechtkomen hebben een hele kleine hoekverdeling dus een lage entropie. Uitgezonden fotonen hebben echter typisch een brede hoekverdeling, wat resulteert in een toename in entropie en een lagere maximale spanning. Een smallere hoekverdeling van de emissie betekent minder toename in entropie van de fotonen, dus een kleiner spanningsverlies. De hoekverdeling van

de lichtemissie is ook van groot belang voor lichtuitzendende diodes (LED's), nanolasers en enkele-fotonbronnen op basis van nanodraden. Daarom hebben we de hoekafhankelijke fotoluminescentie onderzocht van verticale nanodraden, door middel van het detecteren van de lichtemissie in het achterbrandpuntsvlak, ook wel Fouriermicroscopie genoemd. We hebben ontdekt dat de diameter de cruciale parameter is voor de hoekafhankelijke emissie. De diameter bepaalt de aanwezigheid en het voortbewegen van golfgeleidermodes langs de nanodraad. Deze modes bepalen het hoekafhankelijke emissiepatroon. De diameterafhankelijkheid van de golfgeleidermodes is heel gevoelig en kan leiden tot abrupte veranderingen in de hoekafhankelijke emissie. Ook de polarizatie van het licht wordt bepaald door de golfgeleidermodes. Daarom moet de aanwezigheid van deze modes in beschouwing worden genomen bij het ontwerpen van alle fotonische of opto-elektronische apparaten op basis van halfgeleider nanodraden. Tot slot hebben we golfgeleidermodes op een nanodraad gebruikt om de brekingsindex van een nieuw materiaal, wurtzite galliumfosfide. Dit materiaal kan voor vele toepassingen worden gebruikt.

Kortom, dit proefschrift beschrijft de voordelen van het toepassen van nanodraden in zonnecellen. Het levert inzichten die nodig zijn voor het ontwerpen van deze en andere optoelektronische nanodraadapparaten en beschrijft de mechanismes die de lichtemissie en lichtabsorptie van halfgeleider nanodraden bepalen.

SAMENVATTING VOOR IEDEREEN

Veel mensen maken zich grote zorgen vanwege de opwarming van de aarde door de invloed van de mens. Deze opwarming wordt veroorzaakt door de uitstoot van broeikasgassen, wat voornamelijk komt door het verbranden van kolen, olie en gas voor onze energieopwekking. Om de opwarming te beperken is het nodig dat meer andere en schonere methodes voor energieopwekking worden gebruikt. Van deze methodes in zonne-energie een van de meest veelbelovende. De efficiëntie van de meeste zonne-energie-systemen kan echter nog verbeteren, wat de kosten per hoeveelheid energie flink zal verminderen.

Om aan de toenemende vraag aan schone energie tegemoet te komen, is het dus nodig dat de efficiëntie van zonne-energie verbetert. De actieve delen van zonnepanelen zoals die tegenwoordig veel worden gebruikt, worden zonnecellen genoemd. De efficiëntie van fotovoltaïsche cellen (dat zijn zonnecellen die licht direct in elektriciteit omzetten) wordt bepaald door de elektrische spanning en de elektrische stroom.

Dit wijst op twee belangrijke eisen die we stellen aan zonnecellen: ten eerste, de absorptie van licht. Dit is belangrijk, want meer ingevangen licht in de zonnecel betekent meer energie die kan worden omgezet in elektriciteit. Ten tweede moet het ontwerp van de zonnecel zorgen dat de elektrische stroom uit de zonnecel kan worden gehaald zonder verliezen onderweg. Dat betekent dat we een hoge spanning nodig hebben.

In dit proefschrift laten we zien dat zonnecellen die bestaan uit nanostructuren beter kunnen presteren dan zonnecellen die bestaan uit vlakke, gladde laagjes. Als nanostructuren gebruiken wij nanodraden: patronen van verticale paaltjes die ongeveer vijfhonderd keer dunner zijn dan een haar en een lengte hebben van een paar duizendste van een millimeter. Deze verticale draadjes absorberen bijna al het licht (van alle kleuren) en hebben minder elektrische verliezen (dus een hogere spanning) dan vlakke laagjes. Dit laatste komt doordat minder materiaal gebruiken ook zorgt voor minder foutjes (defecten) in dit materiaal. Daarnaast zorgt het gebruik van minder materiaal ervoor dat de zonnecel minder opwarmt, wat ook leidt tot minder verliezen.

Uit onze metingen blijkt dat deze effecten zorgen voor een elektrische spanning in de nanodraadjes die ongeveer eentiende hoger is dan in een vlak laagje gemaakt van precies hetzelfde materiaal. We fabriceren een zonnecel op basis van deze draadjes die 17.8% van het zonlicht omzet in elektriciteit. Dat is een nieuw record voor zonnecellen gemaakt van nanodraden! We hebben daarnaast ook ontdekt dat het plaatsen van kleine doorzichtige nanobolletjes boven op de zonnecel de absorptie van licht in de nanodraden nog verder verhoogt.

Om zonnecellen op basis van nanodraden nog verder te verbeteren kunnen we gebruik maken van het aanpassen van de richtingen van het licht dat door de zonnecel wordt uit-

gezonden. Dit is belangrijk vanwege het verschil in entropie (wanorde) tussen het licht dat binnenkomt vanaf de zon en het licht dat wordt uitgezonden door de zonnecel. Het binnenkomende licht is namelijk een parallelle bundel, met al het licht in dezelfde richting (dus weinig wanorde) en het uitgezonden licht (door het energieverval van de elektronen) beweegt zich in een normale zonnecel ongeorganiseerd in alle richtingen (dus met veel wanorde). Deze toename in wanorde betekent een afname in de maximale energie-opbrengst van de zonnecel. Als we deze lichtemissie kunnen controleren en zorgen dat het allemaal in dezelfde richting wordt uitgezonden, dan wordt de toename van wanorde beperkt. Je zou kunnen zeggen dat we het licht zo beter onder controle houden. Dat levert een betere energie-opbrengst op! In dit proefschrift bestuderen we uitgebreid hoe we de richting van de lichtemissie kunnen controleren. In het kort kan dat doordat de dikte van zo'n nanodraad kleiner is dan de lengte van een lichtgolf. Daardoor kan licht zich maar op een beperkt aantal manieren voortbewgen langs de draad. Dit worden 'golfgeleidermodes' genoemd. Door deze modes slim te gebruiken kunnen we de richtingsverdeling van het licht aanpassen. In een goede zonnecel kunnen we daarmee de maximaal te behalen spanning verhogen.

De richting van het uitgezonden licht is niet alleen belangrijk voor zonnecellen, maar ook voor andere apparaatjes die licht uitzenden. Je kunt daarbij denken aan LED-lampjes of lasers. Door gebruik te maken van slim ontworpen nanodraden als lichtuitzenders kun je de richtingsverdeling van het licht zo sturen dat het voldoet aan de eisen voor het apparaat. Dit kan betekenen dat al het licht in een enkele richting moet worden uitgezonden, maar ook dat het licht in alle richtingen gaat. Naast de richting kan op deze manier ook de polarisatie, dat is de oriëntatie van de trilling van het lichtveld, worden beïnvloed.

Kortom, in dit proefschrift beschrijven we waarom het gebruiken van nanodraadjes in zonnecellen tot een betere energie-opbrengst kan leiden. We leggen uit hoe de interactie tussen de draadjes en het licht werkt, waaruit kan worden afgeleid hoe de vorm en afmetingen van de draadjes moeten worden ontworpen voor de beste zonnecel. Hopelijk draagt dit bij aan een mooie toekomst voor zonnecellen op basis van nanodraden en duurzame energie in het algemeen.

LIST OF PUBLICATIONS

This thesis is based on the following publications:

1. Yingchao Cui*, Dick van Dam*, Sander A. Mann, Niels J.J. van Hoof, René P.J. van Veldhoven, Erik C. Garnett, Erik P.A.M. Bakkers, and Jos E.M. Haverkort, "Boosting solar cell photovoltage by nanophotonic engineering", submitted. (Chapter 4)

2. Dick van Dam, Niels J.J. van Hoof, Yingchao Cui, René P.J. van Veldhoven, Erik P.A.M. Bakkers, Jaime Gómez Rivas, and Jos E.M. Haverkort, "High-efficiency nanowire solar cells with omnidirectionally enhanced absorption due to self-aligned ITO Mie scatterers", submitted. (Chapter 5)

3. Dick van Dam, Diego R. Abujetas, Ramón Paniagua-Domínguez, José A. Sánchez-Gil, Erik P.A.M. Bakkers, Jos E.M. Haverkort, and Jaime Gómez Rivas, "Directional and polarized emission from nanowire arrays", Nano Lett. 15 (7), 4557-4563 (2015). (Chapter 6)

4. Dick van Dam, Diego R. Abujetas, José A. Sánchez-Gil, Jos E.M. Haverkort, Erik P.A.M. Bakkers, and Jaime Gómez Rivas, "Strong diameter-dependence of nanowire emission coupled to waveguide modes", Appl. Phys. Lett. 108, 121109 (2016). (Chapter 7)

5. Simone Assali*, Dick van Dam*, Jos E.M. Haverkort, and Erik P.A.M. Bakkers, "High refractive index in wurtzite GaP measured from Fabry-Pérot resonances", Appl. Phys. Lett. 108, 173101 (2016). (Chapter 8)

* These authors contributed equally to the article

Other publications by the author:

6. Benjamin J.M. Brenny, Diego R. Abujetas, Dick van Dam, José A. Sánchez-Gil, Jaime Gómez Rivas, and Albert Polman, "Directional Emission from Leaky and Guided Modes in GaAs Nanowires Measured by Cathodoluminescence", ACS Photonics 3 (4), 677-684 (2016).

7. Lu Gao, René H.J. Vervuurt, Yingchao Cui, Dick van Dam, René P.J. van Veldhoven, Jan Philipp Hofmann, Ageeth A. Bol, Jos E.M. Haverkort, Peter H.L. Notten, Erik P.A.M. Bakkers, and Emiel J.M. Hensen, "High-efficiency InP-based photocathode for hydrogen production by interface energetics design and photon management", Adv. Funct. Mat. 26 (5), 679-686 (cover) (2016).

8. Benjamin J.M. Brenny, Dick van Dam, Clara I. Osorio, Jaime Gómez Rivas, and Albert Polman, "Azimuthally polarized cathodoluminescence from InP nanowires", Appl. Phys. Lett. 107, 201110 (2015).

9. Anthony J. Standing, Simone Assali, Lu Gao, Marcel A. Verheijen, Dick van Dam, Yingchao Cui, Peter H.L. Notten, Jos E.M. Haverkort, and Erik P.A.M. Bakkers, "Efficient Water Reduction with Gallium Phosphide Nanowires", Nature Comm. 6, 7824 (2015).

10. Arjan Keeman, E. Stefan Kooij, Dick van Dam, Ruud E.I. Schropp, Marcel Di Vece, "Optical Response of Silver Nanoneedles on a Mirror", Plasmonics 15, s11468-015-9900-y (2015).

11. Grzegorz Grzela, Ramón Paniagua-Domínguez, Tommy Barten, Dick van Dam, José A. Sánchez-Gil, and Jaime Gómez Rivas, "Nanowire Antenna Absorption Probed with Time-Reversed Fourier Microscopy", Nano Lett. 14 (6), 3227-3234 (2014).

Patents:

1. Dick van Dam, Yingchao Cui, Jos E.M. Haverkort, and Erik P.A.M. Bakkers, "Nanostructured solar cell optimized for efficient emission of internally generated photoluminescence", US Provisional Patent 62/351458 (2016).

Laat mijn hand niet
Laat mijn hand niet gaan
Je hoeft dit niet alleen te doen

Het wordt beter
Met elkaar wordt het beter

Beter – *BLØF*[*]

ACKNOWLEDGEMENTS

Although this thesis has only one name on its cover, many people have delivered important contributions to its content. I am grateful to all of them. I will mention a selection of these people specifically below.

Allereerst dank ik Jos Haverkort, Erik Bakkers en Jaime Gómez Rivas voor hun vertrouwen en begeleiding. Jos, bedankt voor je sturing, kritische houding en relativering. Het was fijn dat ik altijd even bij je kon binnenlopen voor snelle feedback of advies. Erik, het was fijn om je als begeleider te hebben. Ik bewonder je optimisme en je vermogen om zo veel dingen tegelijk te doen en tegelijk de persoonlijke noot te behouden. Ook dank voor al je schrijf- en presentatietips. Jaime, it was a pleasure to work with you. I have learned a lot from our in-depth discussions about physics, research and other things. Still, I never know whether we should talk in English or in Dutch. In any case: muchas gracias.

My direct colleagues and collaborators have greatly contributed to this thesis. Yingchao Cui, thank you very much for fabricating the solar cell devices that made my work possible. Also, thank you for the many discussions that we had on the device physics. Alessandro Cavalli, thanks for many nanowire samples that you grew, SEM images and for being my buddy on the project. Simone Assali, thank you for the joint project and for keeping me company during the early mornings in the office. Anthony Standing, thank you very much for many tricky PDMS transfers! René van Veldhoven, thanks for the growths and joint work. Luca Gagliano, thanks for a few growths and SEM images, for being our faithful football captain and for sending funny, politically incorrect emails. Thuy Vu, my buddy from the beginning of my PhD! I enjoyed our time in the office together and the great Vietnam visit. Michele Cotrufo, thank you for the e-beam lithography. Grzegorz Grzela, you're my experimental mentor. Many experimental techniques and scripts that I have used in this thesis were developed by you. Thank you for your patience and guidance in the lab, and for the nice trip that we had in Israel and Jordan. Mohammad Ramezani, thank you for your help and for fun in the lab, the office and in Spain.

* Translation: don't let my hand / don't let go my hand / you don't need to do this by your own / it will get better / together it will get better

I am grateful to the master and bachelor students that I could supervise. Niels van Hoof, het was een plezier om je te begeleiden, tijdens een ingewikkeld jaar met de labverhuizing en werken op meerdere plaatsen. Ik ben erg blij dat je bent gaan promoveren! Veel succes (maar dat komt zeker goed)! I also thank my other students, Wouter van de Koppel, Daan Nieuwenhuizen, Meng Liu en Chi Feng, who all contributed to my PhD.

I thank the secretaries, Thérèse-Anne and Simone, for their crucial help during the entire time of my PhD. Then, I want to thank all other colleagues whom I shared an office and/or my love for semiconductor nanowires: Diana, Ikaros, Saša, Yizhen, Daniel, Alain, Milo, Ruben, Rianne, Jia, Sebastien, Sebastian, Sonia, Johannes, Ryan, Douglas, Elham, Ang, Lachlan, Lu, Ilaria, Rob, Marcel. Also thanks to all other colleagues and staff members at the Photonics and Semiconductor Nanophysics group who greatly contributed to the nice working environment: Christian, Davide, Joost, Erwin, Juanita, Samuel, Frank, Leonardo, Döndü, Sartoon, Rosalinda, Zili, Tian, Francesco, Daniele, Maurangelo, Hans, Simone, Giulia, Andrei, Andrea, Paul. Thank you all for the discussions, the fun in the lab and/or in the office, during conferences, coffee breaks, and football tournaments. Paul, thank you for managing the group in a positive and personal way. Also, thanks to the members of the Surface Photonics/Photonics for Energy group that I didn't mention yet: Tommy, Said, Giuseppe, Gopika, Martijn, Gabriel, Giorgos, Arko, Shaojun, Alexei, Pieter, Wybren, Laura. It's been a pleasure to share the lab and collaborate with you! Ik dank ook Harm, mijn kamergenoot bij Philips, voor de behulpzaamheid en gezelligheid. Dank ook aan alle andere medewerkers van de TU/e, DIFFER en Philips die direct of indirect hebben bijgedragen aan mijn werk.

I have greatly benefitted from our collaboration with our amigos from the Instituto Estructura de la Materia from the Consejo Superior Investigaciones Científicas in Madrid: Diego Abujetas, Ramón Paniagua-Domínguez, and José Sánchez-Gil. Thank you for the many simulations and discussions and for hosting us during the short but nice visit in 2015.

Very important for my work was the collaboration with FOM-institute AMOLF. Sander Mann and Erik Garnett, thank you for the discussions that we had which were crucial for our understanding of nanowire solar cells, and for the simulations. Benjamin Brenny and Albert Polman, it was a pleasure to work together on the cathodoluminescence measurements on the nanowires. It turned out to be very effective! We didn't quite get what we expected, but the results were nevertheless beautiful. Albert, thank you for hosting the Light Management in Photovoltaics meetings, which gave me the opportunity to interact with many other solar cell enthusiasts.

I thank the user committee of the STW project, in particular Michiel Mensink and Dick de Boer, for their interest in our work. I also acknowledge the reading committee of this thesis for their effort and interest: José Sánchez-Gil, Albert Polman, Henk Swagten and Ruud Schropp.

Ik dank al mijn docenten en begeleiders gedurende al mijn opleidingen, van basisschool tot universiteit. Ik heb veel geleerd, maar niets was belangrijker dan plezier hebben in leren en kennis vergaren. Veel dank hiervoor en ga zo door!

Ik dank mijn vrienden omdat ze mijn vrienden zijn en voor alle momenten die we met elkaar delen. Mijn floorballmates zijn belangrijk voor me omdat samen sporten me altijd blij en moe tegelijk maakt. Ik dank mijn hele familie vanwege hun onvoorwaardelijke vriendschap en saamhorigheid. In het bijzonder mijn ouders en broers en zussen: veel dank. Jullie betekenen meer voor me dan jullie denken.

Mijn lieve Ellen, we hebben de afgelopen jaren allebei duizenden uren in de trein doorgebracht, voornamelijk om iedere dag even samen te zijn. Het was me iedere seconde waard. Ik hou van jou, iedere nieuwe dag weer een beetje meer dan de vorige.

Veel dank,
Dick

CURRICULUM VITAE

Dick (Arie Dirk) van Dam was born in Leerbroek (Zederik municipality, Zuid-Holland) on April 12, 1988. He grew up in Aagtekerke (Zeeland) and went to highschool at CSW in Middelburg. In 2006, he started studying at Utrecht University where he obtained bachelor degrees in both Physics and Astronomy and in Mathematics. He interrupted his courses for one year (2008-2009) to serve as fulltime chairman of study association A–Eskwadraat. He was also an active member of students' association S.S.R.-N.U. In 2010 he started a master's program in Physics, which he completed in 2012. Dick went on a master exchange to University of Florida (USA), where he followed courses in Mechanical Engineering and Materials Engineering. His master thesis research was conducted in the group of Ruud Schropp at Utrecht University, on plasmonic nanoholes and nanostructures for application in thin-film silicon solar cells. During his studies, he participated in several representative councils and education boards at the Departments of Physics and Mathematics and at the Faculty of Science of Utrecht University.

In 2012, Dick participated in the television trivia quiz *'Met het mes op tafel'*, in which he became the winner of the season. Also in 2012, Dick started his PhD research in the group of Erik Bakkers and Jos Haverkort at Eindhoven University of Technology, in a close collaboration with the group of Jaime Gómez Rivas at Philips Research and AMOLF (later at DIFFER). He worked on the interaction of light with nanowires, aimed at application in solar cells. His work resulted in more than ten scientific publications and he gave presentations in 15 national and international conferences. At Fysica 2016, the annual congress of the Dutch Physical Society (NNV), Dick won the Young Speakers Contest competition. Dick was assisting teacher at several freshmen courses, and won the education award for best teaching assistent for the freshmen experimental physics course in 2014.

In his free time, Dick enjoys sports, especially floorball, cycling and running. He also likes natural landscapes.